

博士論文

Nitrogenation and Decomposition Properties of
Alkali Metal Compounds

アルカリ金属化合物の窒化及び分解特性

山 口 翔 太 郎

広島大学大学院先端物質科学研究科

2017 年 3 月

目次

1. 主論文

Nitrogenation and Decomposition Properties of Alkali Metal Compounds

(アルカリ金属化合物の窒化及び分解特性)

山口 翔太郎

2. 公表論文

(1) Thermal Decomposition of Sodium Amide

Shotaro Yamaguchi, Hiroki Miyaoka, Takayuki Ichikawa, and Yoshitsugu Kojima
International Journal of Hydrogen Energy, **42**, 5213-5219, (2017)

3. 参考論文

(1) Thermochemical Water-Splitting Reaction by Alkali Metal-Cobalt Oxide

Shotaro Yamaguchi, Naoya Nakamura, Hikaru Yamamoto, Hitoshi Inokawa,
Takayuki Ichikawa, Yoshitsugu Kojima, and Hiroki Miyaoka
Journal of the Japan Institute of Energy, **92**, 909-912, (2013)

(2) Anode Properties of Al₂O₃-added MgH₂ for All-Solid-State Lithium-Ion Battery

Suguru Ikeda, Takayuki Ichikawa, Kiyotaka Goshome, Shotaro Yamaguchi,
Hiroki Miyaoka, and Yoshitsugu Kojima
Journal of Solid State Electrochemistry, **19**, 3639-3644, (2015).

(3) Catalysis of Lithium Chloride and Alkali Metal Borohydrides on Hydrogen Generation of Ammonia and Lithium Hydride System

Hiroki Miyaoka, Keita Nakajima, Shotaro Yamaguchi, Taihei Aoki, Hikaru Yamamoto, Takahiro Okuda, Kiyotaka Goshome, Takayuki Ichikawa, and Yoshitsugu Kojima
Journal of Physical Chemistry C, **119**, 19922-19927, (2015)

(4) Catalytic Modification in Dehydrogenation Properties of KSiH₃

Ankur Jain, Takayuki Ichikawa, Shotaro Yamaguchi, Hiroki Miyaoka, and Yoshitsugu Kojima

Physical Chemistry Chemical Physics, **16**, 26163-26167, (2014)

- (5) Effects of Metal Oxide Additives on Anode Properties of Magnesium Hydride for All-Solid-State Lithium Ion Batteries

Suguru Ikeda, Takayuki Ichikawa, Shotaro Yamaguchi, Hiroki Miyaoka, and Yoshitsugu Kojima

Journal of the Japan Institute of Energy, **93**, 926-930, (2014)

主論文

Abstract

Nitrogen (N) forms various kinds of compounds with the other elements, and the nitrides are used as functional materials in wide fields such as photovoltaic cell and hydrogen storage materials. In order to further effectively use the nitrides, development of nitrides synthesis and investigating decomposition properties should be necessary as a fundamental research. In this thesis, the following two subjects related to the nitrides were focused.

Although it is better to synthesize nitrides from nitrogen (N_2) because of its abundance in the air, nitrogen is very stable molecule due to its strong triple bond, and therefore high temperature and huge energy are required to dissociate N_2 in current nitrides synthesis processes. As a social demand, much more effective processes to synthesize nitrides from N_2 in the air are strongly desired. In this work, we focused on the dissociation of nitrogen molecules by using lithium alloys, which are synthesized by some reactions between lithium metal and group 14 elements; carbon, silicon, germanium, and tin. Then, the nitrogenation and denitrogenation properties are investigated by thermal and structural analyses. Nitrogen triple bond is dissociated by all the lithium alloys below 500 °C, and the formation of lithium nitride (Li_3N) is indicated except for the lithium-germanium alloy in which ternary compound is generated. The denitrogenation (nitrogen desorption) reaction by lithium nitride and each element, which is ideal opposite reaction of nitrogenation, proceeds by heating up to 600 °C. It is revealed that ternary composites were generated after the reaction for the case of silicon and germanium although lithium alloys were formed for carbon and silicon cases. The lithium-tin alloy is a potential material for realizing reversible nitrogenation and denitrogenation reactions below 500 °C. Among nitrides synthesis and nitrogen desorption reactions, phase separation and solid-solid reaction is essential, indicating the high mobility of lithium atom. In addition, the products in these reaction possess nano-size and/or amorphous phase, meaning the high reactivity. These facts lead to the application for the ammonia synthesis. As a result, ammonia can be synthesized below 300 °C under 0.5 MPa of pressure. Therefore, the reactions using lithium alloys is recognized as a pseudo-catalyst for the ammonia synthesis.

Light metal amide-imide systems show high hydrogen capacity, and a lot of research have been reported so far. Among them, only a few studies have reported about sodium composed system, indicating that it should have complicated reaction process and difficult handling. As a fundamental research, it should be required to discuss the detailed reaction properties of sodium-including materials. In this work, thermal decomposition properties of sodium amide up to 400 °C are investigated under different reaction conditions to understand the decomposition process. The results of thermal analyses show exothermic reaction with crystallization at 120 °C and two endothermic reaction with phase transitions at 150 and 200 °C with small amounts of nitrogen desorption, concluding that decomposition of bulk NaNH_2 does not proceed up to 230 °C. To understand the further details, thermal decomposition is performed at 400 °C with and without partial pressure of generated reaction gases during the decomposition process. After the reaction under vacuum condition, metallic sodium and unknown phase are formed as the products. From the structural characterization, the new phase would be identified as the imide-like material. In the other reaction conditions, sodium amide and hydride are found as solid products without the Na generation. With the consideration of reaction process, the imide-like new phase might be generated as an intermediate phase in this reaction condition as well. In addition, hydrogen, nitrogen, and ammonia are desorbed as gaseous products, suggesting that their partial pressures affect the reaction pathway thermodynamically.

Contents

1 Introduction	1
1-1 Nitrides as functional material.....	1
1-1-1 Basic background - why nitrides are important and interesting	1
1-1-2 Nitrogen dissociation	3
1-2 Nitrides synthesis with nitrogen dissociation reaction	4
1-2-1 Conventional methods (heat, plasma, catalysts)	4
1-2-2 Transition metal alloys.....	7
1-2-3 Lithium alloys	9
1-3 Application of nitride	18
1-3-1 Semiconductor	18
1-3-2 Bearing.....	20
1-3-3 Coating.....	21
1-3-4 Nitrogen source for nitride synthesis: ammonia (NH ₃)	22
1-3-5 Energy (hydrogen) carrier and storage	24
1-4 Thermodynamics and kinetics	29
Reference	36
2 Purpose	40
Reference	42
3 Experimental procedure.....	43
3-1 Sample preparation	43
3-1-1 Materials	43
3-1-2 Mechanical ball-milling method	44
3-1-3 Synthesis of samples	45
3-2 Experimental techniques.....	46
3-2-1 Powder X-ray diffraction (XRD)	46
3-2-2 Thermogravimetry – Differential thermal analysis (TG-DTA)	49
3-2-3 Differential scanning calorimetry (DSC).....	51
3-2-4 Thermal desorption mass spectroscopy (TDMS)	54
3-2-5 Fourier transform infrared (FT-IR) spectroscopy	56

3-2-6 Raman spectroscopy	59
3-2-7 Transmission Electron Microscope (TEM).....	61
3-2-8 Scanning Electron Microscope (SEM)	64
3-2-9 Energy Dispersive X-ray Spectroscopy (EDS).....	66
3-2-10 Gas chromatography (GC).....	67
Reference	69
4 Results and discussions	70
4-1 Nitrogenation of Li-M alloys.....	70
4-1-1 LiC alloy	70
4-1-2 Li-Si alloy	71
4-1-3 Li-Ge alloy	72
4-1-4 Li-Sn alloy	73
4-2 Denitrogenation	85
4-2-1 Mixture of C and Li_3N	85
4-2-2 Mixture of Si and Li_3N	85
4-2-3 Mixture of Ge and Li_3N	86
4-2-4 Mixture of Sn and Li_3N	86
4-3 Ammonia synthesis	93
4-4 Thermal decomposition of NaNH_2	100
References	114
5 Conclusion	115

1 Introduction

1-1 Nitrides as functional material

1-1-1 Basic background - why nitrides are important and interesting

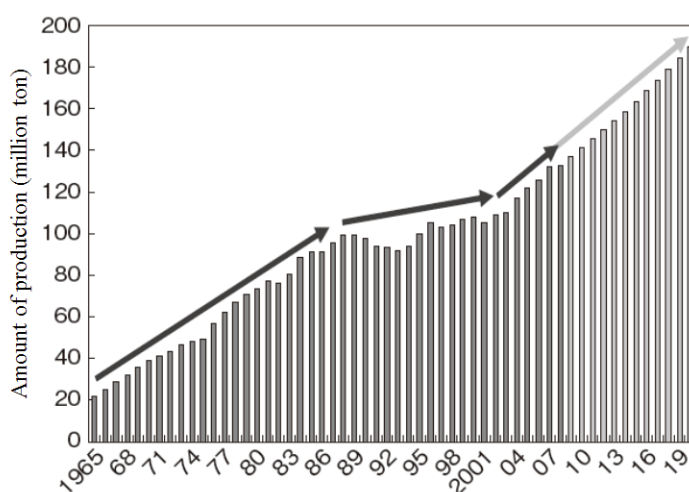
Nitrogen (N) is abundant element on the earth, where N_2 gas is the largest component of the air (about 78%). When nitrogen forms nitride with inorganic elements, some characteristic properties could be appeared. Some nitrides are well known as functional materials and practically used in various kinds of field. Many kinds of metal nitrides have been already reported so far. On the other hand, nitrogen can make covalent bonds with non-metallic element such as hydrogen (H), carbon (C), oxygen (O), and sulfur (S).

Ammonia (NH_3) is a typical functional nitride as materials of fertilizer and utilized for a long time. After industrial revolution in the end of 19th century, the world population was drastically increased with large demand for food. It was well known at that time that nitrogen fertilizer is important for farm products and several techniques for nitrogen fixation were established. Therefore, ammonia is one of the important nitrides for agriculture. As shown in Figure 1-1-1, the amount of NH_3 production is increased about 6 times for 40 years after 1965, and it can be estimated that the ammonia production will keep on evolving. This expected large amount of ammonia production is caused by not only for the demands from agriculture but also as an energy carrier. Recently, utilization of renewable energy is necessary as the alternative energy of fossil fuels because of resources limitation (depletion) and environmental problems due to the carbon dioxide emitted by using fossil fuels. For the fast development of these techniques, transportation technique of the energy should be also developed. Hydrogen is thought to be one of the promising energy carrier due to its high gravimetric energy density and realization for the transportation with large amount. However, volumetric energy density of hydrogen is extremely poor. One of the techniques to compactly store the hydrogen, hydrogen storage systems or materials have suggested. Thus, liquid ammonia has been recognized as a promising hydrogen carrier because of its notably high gravimetric and

volumetric hydrogen density compared to the other hydrogen storage materials. In addition to NH_3 , the other nitrides such as lithium nitride (Li_3N) and amide (MNH_2) are considered as solid state hydrogen storage materials with high gravimetric hydrogen capacity in recent years.

Some nitrides can be applied to semiconductors, paint materials, and photocatalysts by using suitable energy gaps. Especially, in the field of semiconductor, nitrides are widely utilized. Particularly, Dr. Shuji Nakamura, Dr. Isamu Akasaki, and Dr. Hiroshi Amano got the Nobel Prize in 2014 for the study of blue light-emitting diode by using gallium nitride (GaN)¹⁻¹⁻⁴). This discovery realizes the white light which is consisted by red, green, and blue light. Furthermore, the recording media field has drastically developed by using blue light represented by Blu-ray Disc, which can record more than 5 times larger information compared to typical DVD disc. Moreover, some nitrides are utilized as engineering application because of its characteristic physical properties. For instance, nitrides with high heat resistance are suitable material for high temperature structural applications such as gas turbine engines. Furthermore, nitrides are used as coating material. The details of functional nitrides are described at the following sections.

As mentioned above, the research on efficient nitride synthesis and utilization techniques are quite important for development of energy, industrial, and manufacturing fields.



* ~2008 : U.S. Geological Survey

2009~ : Assume the increase of ammonia demand at 3 % annual rate (MITSUI & CO., LTD.)

Figure 1-1-1 Ammonia production amount per year¹⁻⁵⁾

1-1-2 Nitrogen dissociation

Nitrogen can make ionic bond, covalent bond, and solid solution depending on the component metals. N_2 molecules have the stable triple bond ($N\equiv N$) with 945 kJ mol^{-1} ^{1-6, 7)}, although similar diatomic molecules such as oxygen (O_2) and hydrogen (H_2) show lower bond energy of 498 kJ mol^{-1} and 436 kJ mol^{-1} , respectively. Thus, how to dissociate the strong triple bond of nitrogen molecules should be an important issue if nitrogen-containing materials are directly synthesized from N_2 gas. So far, more than 800°C and/or nitrogen plasma are necessary to synthesize nitrides because of the high kinetic barrier to dissociate N_2 . Some materials revealed their catalytic activities for nitrogen dissociation such as iron, ruthenium, and electride. Especially, iron-based catalyst is used for the Haber-Bosch process, which is a typical mass production system for ammonia. Besides, ammonia is often used as a nitrogen source because of its low N-H binding energy (389 kJ mol^{-1}) compared with N triple bond. However, it is not desirable to use costly materials as catalyst and to be supplied with high energy to synthesize ammonia. Hence, studying for the catalysts still has much attention to dissociate the nitrogen triple bond. It is desired to establish a feasible and efficient way to synthesize nitride from the direct use of nitrogen gas. Therefore, new concepts and breakthroughs are essential to overcome these problems.

1-2 Nitrides synthesis with nitrogen dissociation reaction

Nitrogen (N) is one of the most related element for our lives and is abundant on the earth, where the air is constituted by 78 % of N_2 gas. Many materials are composed of nitrogen regardless of organic or inorganic fields. N_2 molecules have the stabled triple bond ($N\equiv N$) with 945 kJ mol^{-1} ^{1-6, 7)}, although diatomic molecule represented by oxygen and hydrogen show the bond energy of 498 kJ mol^{-1} and 436 kJ mol^{-1} , respectively. Thus, how to dissociate the strong triple bond of nitrogen molecule should be important issue when nitrogen including materials are synthesized by directly use of N_2 gas.

1-2-1 Conventional methods (heat, plasma, catalysts)

Nitrides are well known as functional materials and practically used in various kinds of fields. Metal nitrides, especially group 13 nitrides such as aluminum nitride (AlN), gallium nitride (GaN), and indium nitride (InN), have attracted much attention as semiconductors for the application of electrical devices represented by light-emitting diode using those feasible bandgap.

The simplest method to synthesize these nitrides is a reaction between metal and nitrogen gas (N_2). Figure 1-2-1¹⁻⁸⁾ shows experimentally obtained enthalpy for each material, where the dashed lines indicate the limits of available experimental conditions. The standard enthalpy for all nitrides shows negative value, meaning that elemental substances theoretically react with N_2 gas under the ambient temperature and pressure (0.1 MPa) by exothermic reactions. High pressure and temperature are often necessary to satisfy nitrogenation conditions. These facts suggest that N_2 molecules are very stable and high energy supply should be required to dissociate the stable triple bond.

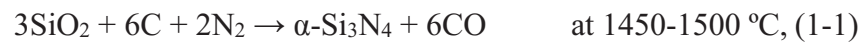
Needless to say, GaN is the important component for blue light-emitting-diode (LED). AlN is featured by its high insulation property and thermal conductivity, applying to electronic substrate.

For the synthesis of GaN and AlN, metalorganic chemical vapor desorption (MOCVD) method is widely used¹⁻⁹⁾. In this process, high temperature in excess of 800°C is required to obtain high quality nitrides as single crystal. The best electrical and optical performance of GaN can be shown when the operating temperature is fixed at

1050 °C. As shown in Figure 1-2-1, AlN is more stable than GaN. When MOCVD method is used to AlN synthesis, high temperature range from 1050 to 1200 °C is needed, and more than 1200 °C should be required to obtain a high quality single crystal. Then, molecular beam epitaxy (MBE) technology as reactive nitrogen sources is favorable technique to reduce the reaction temperature, which can be applied for both the nitride syntheses. The key issue in the synthesis by MBE is nitrogen source. Several kinds of nitrogen sources such as microwave N₂ plasma are acceptable and these are coupled with MBE, resulting in the reduced reaction temperature around 350 °C in the case of AlN.

InN is quite significant group 13 nitride semiconductor for many potential applications. The use of InN and its alloys with GaN and/or AlN makes it possible to expand the emission range of LED from ultraviolet to near infrared. The InN synthesis with high quality, which means low contamination and high crystalline form, is difficult due to the low dissociation temperature as shown in Figure 1-2-1. In order to decrease the reaction temperature, metalorganic vapor phase epitaxy (MOVPE) method, in which ammonia is generally used as a nitrogen source, is utilized as the most popular technique of InN synthesis. From the quality of the synthesized InN, it is found that the most suitable operating temperature range is from 500 to 650 °C. However, a single crystal can be generated at a temperature as low as 400 °C^{1-10, 11)}.

Silicon nitride (Si₃N₄) shows the high stability in temperature ranges from room temperature to 1400 °C, wear resistance, low friction, high stiffness, and low density. These characteristic properties have led to the utilization for ball bearings, oil drilling, and vacuum pumps. There are a few ways for commercially accepted Si₃N₄ powder production as follows¹⁻¹²⁾.



One of the ways to synthesize Si₃N₄ is the carbothermal reduction of SiO₂ powder under nitrogen gas (eq. (1-1)). This method was established as the initial technique and have been widely used at present because of its effective cost performance and available high purity Si₃N₄ powder. However, the high operating temperature around 1500 °C should be caused by the high stability of SiO₂ as well as nitrogen. The direct nitrogenation of silicon

powder by eq. (1-2) was developed in the 1960s and was the first large-scale method for powder production. The high purity of Si_3N_4 is required to utilize its characteristic properties with the best performance, however, tiny amounts of impurities such as iron (Fe) cannot stop being included because Fe exists in Si originally, and small amounts of Fe is mingled with Si to accelerate the nitrogenation reaction and cannot be removed completely after the reaction. Both reactions need high temperature at least 1300 °C to realize the nitrogen dissociation.

Titanium nitride (TiN) is known as coating materials because it shows low friction coefficient, extremely high abrasion resistance, and high hardness. A reaction of titanium metal powder with nitrogen gas should proceed at 1760 °C thermodynamically (nitrogen pressure is assumed at 0.1 MPa)¹⁻¹³, which is very high temperature. By using physical vapor deposition (PVD), in which titanium metal is vaporized in a nitrogen plasma, the reaction temperature can be decreased although high energy supply is necessary. TiN is able to be obtained as following reaction,



this carbothermal reduction of titanium oxide proceeds at 1150 °C¹⁻¹⁴. The reaction temperature can be decreased to 800 °C by using NH_3 as nitrogen source instead of nitrogen gas¹⁻¹⁵).

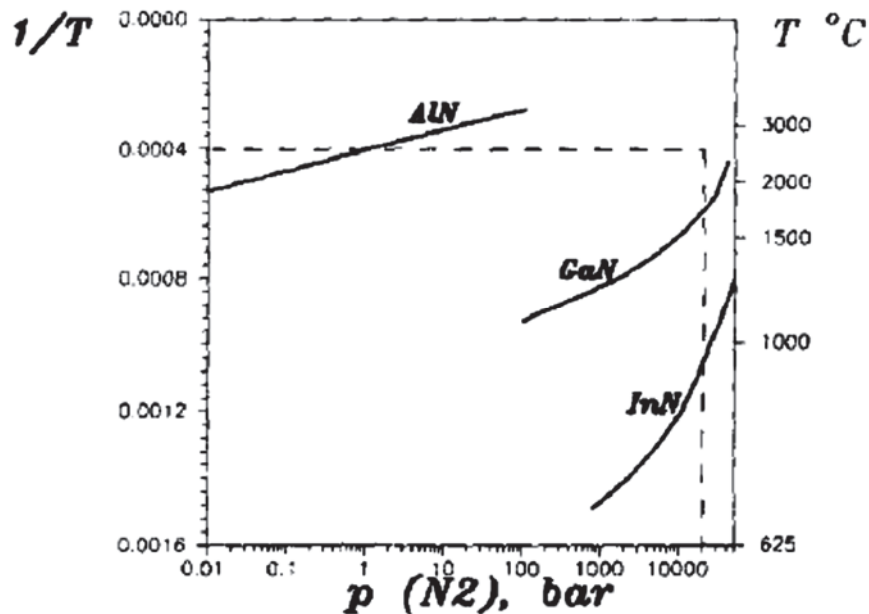


Figure 1-2-1 Thermodynamics of group 13 compounds¹⁻⁸⁾

1-2-2 Transition metal alloys

For the ammonia synthesis whose reaction essentially includes nitrogen dissociation, exploring alternative catalysts from rare-earth metal should be essential from the aspect of cost. To find suitable catalysts, studies without use of noble metal alloy have been carried out. It was reported in the early 1900s that Fe-cobalt (Co) alloys show catalytic effects for the ammonia synthesis¹⁻¹⁶, and furthermore, molybdenum (Mo) shows similar catalytic effects when it makes alloys with Fe, Co, or nickel (Ni) and also Co-rhenium (Re)¹⁻¹⁷. Jacobsen C. J. H. *et al.*¹⁻¹⁶ proposed ammonia synthesis activity of several catalysts by calculational study with a complete agreement of experimental evidence in the case of ruthenium (Ru) and osmium (Os), which show the high catalytic performance (shown in Figure 1-2-2). On the other hand, Co-Mo alloys show the

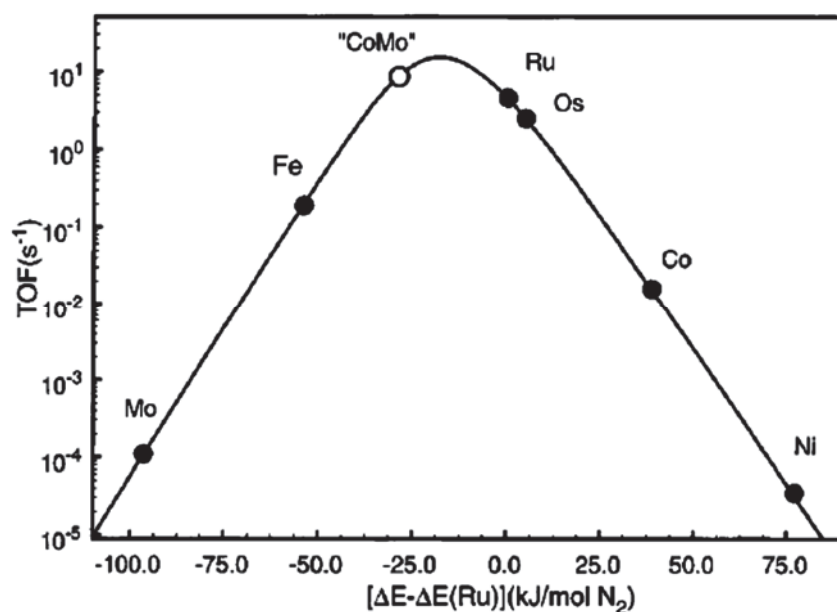


Figure 1-2-2 Calculated turnover frequencies for ammonia synthesis as a function of the adsorption energy of nitrogen¹⁻¹⁶

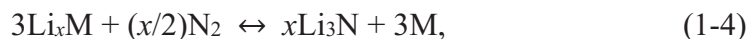
equivalent efficiency compared with these metals. It is suggested as one of rational approach for designing two-metal-combined catalysts that should be constructed by the combination of materials with high and low nitrogen interaction energy. In fact, Mo makes stable bond with N in contrast to Co with weak interaction. Mo based ternary nitrides, Fe₃Mo₃N, Co₃Mo₃N, and Ni₂Mo₃N exhibit catalytic activities as well in the N₂

pressure range between 0.1 and 10 MPa and temperature range from 320 to 500 °C. This reaction condition is relatively milder than that of Haber-Bosh process, which needs high pressure of 20-35 MPa and high temperature of 500 °C. The catalytic effects are enhanced by adding cesium (Cs) into the catalysts^{1-18, 19)}. Especially, Co₃Mo₃N revealed significant catalytic activities even under 0.1 MPa at 400 °C¹⁻¹⁷⁾.

1-2-3 Lithium alloys

Lithium metal easily reacts with nitrogen, forming Li_3N at relatively low temperature. The most simple and effective way is nitrogenation of Li metal, which requires at the temperature around $30 - 400\text{ }^\circ\text{C}$ ¹⁻²⁰⁻²²). However, Li_3N is thermodynamically stable material of which ΔH is -165 kJ mol^{-1} and it is difficult to realize reverse reaction without an energy input such as the introducing high temperature. On the basis of database, around $800\text{ }^\circ\text{C}$ is required to decompose Li_3N into Li metal and N_2 (nitrogen pressure is assumed at 0.1 MPa).

To control the dissociation of N_2 and utilize the N atoms under moderate conditions, we have focused on the following reaction using Li alloys.



If Li in the alloys takes metal state, a shift resulting from nuclear magnetic resonance (NMR) shows a significantly larger value compared with that of ionic compounds, which is so-called Knight shift ^{1-23, 24}). Actually, the Knight shift of Li atom in Li intercalated graphite observed by NMR is around 40 ppm (Li metal: more than 200 ppm). Because metallic state of Li atom is expected to be high activity with nitrogen gas, the dissociation properties should be expected even in the case of Li alloys. Furthermore, the ΔH value of the reverse reaction of (1-4) should be lower than that of Li_3N decomposition into Li and N_2 because the relatively stable alloy phases is formed as the reaction products.

The above concept is proposed on the basis of previous research on hydrogen absorption and desorption properties of Li alloys,



where, M is thought to be 14 group elements; such as carbon (C), silicon (Si), germanium (Ge), and tin (Sn). In fact, by using the Li alloys, the hydrogen absorption and desorption temperatures are clearly reduced compared with LiH decomposition. It is expected that the above phenomena are originated in the high reactivity with H_2 and the high mobility of Li in the alloys. Therefore, it is possible that the N_2 absorption (nitrogenation) and desorption (denitrogenation) reactions are operated at lower temperature than those of Li_3N by using the Li alloys.

In the following parts, the basic properties of the Li alloys are described.

Lithium Graphite alloy

The graphite possesses layer structure which is composed of hexatomic rings as shown in Figure 1-2-3. And each layer is generally called and known as graphene. The crystal structure is classified to hexagonal with $a=2.46 \text{ \AA}$ and $c=6.71 \text{ \AA}$ ¹⁻²⁵). Each carbon

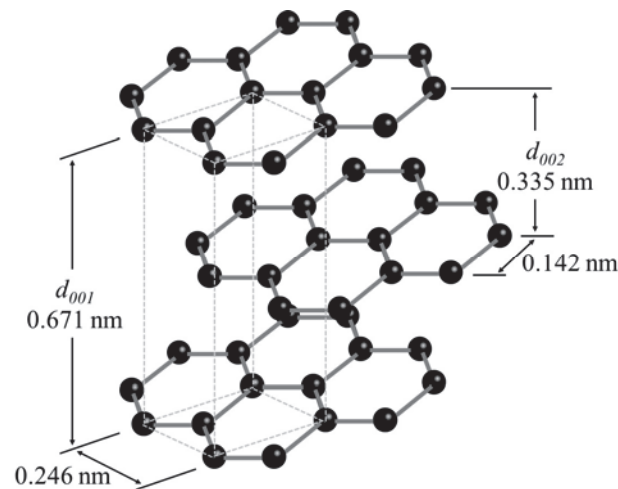


Figure 1-2-3 Crystal structure of graphite ¹⁻²⁵⁾

atom is strongly combined with the sp^2 hybridization bond to form the angle of 120° in the graphene sheet. The layers are combined with van der Waals force. The distance of contiguous atoms and layer-direction are 0.142 and 0.335 nm , respectively. The structural properties of graphite is characterized by XRD and Raman spectroscopy. Particularly for XRD measurement, the distance of lattice plane can be estimated by diffraction angle by Bragg's law. Graphite structure shows characteristic strong diffraction peak originated in the (002) lattice plane and analyzing its peak is effective way for estimating the layer distance. It is well known that graphite can form intercalated compounds with some alkali metals such as lithium (Li) and potassium (K). With the increasing of layer distance due to the insertion of atoms, the peak position corresponding to (002) diffraction is shifted to low angle according to Bragg's law. As synthesis of Li intercalated graphite, there are three techniques, which are thermochemical, electrochemical, and mechanochemical processes. The electrochemical process is the same process as the electrode reaction of Li ion battery. The Li intercalated graphite is conventionally synthesized by thermochemical processes using the reaction between Li vapor and graphite. However, the vapor pressure

of lithium is low, leading to the difficulty for synthesizing the lithium carbon alloy around room temperature. Namely, excess energy supply is required for the synthesis from kinetic reason although the reaction is exothermic. The electrochemical method is quite typical way and LiC_6 is well known as negative electrode of lithium ion battery. As the other technique for synthesizing the lithium carbon alloy, mechanical milling is one of the ways¹⁻²⁶⁾.

Interlayer distance of the Li intercalated graphite LiC_6 , LiC_{12} , and LiC_{24} is 0.370, 0.352, and 0.347 nm, respectively¹⁻²⁷⁾. Namely, when larger amount of lithium is intercalated into graphite layers, the interlayer distance is more expanded.

Graphite exhibits strong anisotropy for physical and chemical properties because of its layered structure. Especially for in-plane dimension, the π -electrons can move on the graphite layer and behave like conductive electron, resulting in the high electric conductivity. Thus, the electrical resistivity of the in-plane direction on graphite is low and comparable to metals.

LiC_6 is a typical material for negative electrode of lithium ion battery with lithium cobalt oxide (LiCoO_2) as positive electrode. Various electrical devices are employed for the lithium ion battery because its high energy density, high cycle life, and no memory effect. Lithium insertion and extraction occur electrochemically during the charge and discharge process of battery, and then six carbon (6C) can accept one lithium (Li) showing the capacity of 372 mA h g^{-1} .

Miyaoka *et al.*¹⁻²⁶⁾ reported that the above reactions with moving Li can be adapted to hydrogen absorption and desorption reactions. In this paper, three kinds of different graphite-based materials were prepared as starting materials by the ball milling: (1) as received graphite (G); (2) pre-milled graphite for 8 h under 1 MPa H_2 (HG); (3) pre-milled graphite for 8 h under 1 MPa Ar (AG). Each graphite was ball-milled with Li metal under Ar for 3 h. Hydrogen absorption properties were investigated under 0.5 MPa H_2 flow up to 500 °C. To examine the hydrogen desorption of Li-C compounds, hydrogenated samples were prepared and heated up to 500 °C under Ar flow. Table 1-2-1 shows the hydrogenation and dehydrogenation properties for each sample. Among them, it was revealed that H_2 can be reversibly stored in the Li intercalated graphite with the Li

deintercalation and intercalation reaction below 200 °C by the following equation,



Table 1-2-1 Hydrogenation and dehydrogenation reaction of Li-C alloys

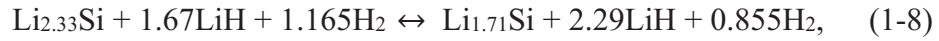
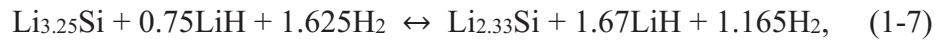
	Hydrogenation reaction under 0.5 MPa H ₂ flow	Dehydrogenation reaction (Total weight loss at 500 °C)
Li-G	100-180 °C with the generation of LiH and Graphite	150 °C with the generation of LiC ₁₂ and Li ₂ C ₂ (1 mass%)
Li-HG	120 °C with the generation of LiH and Graphite 190 °C with the generation of Li ₂ C ₂	180 °C with the generation of Li ₂ C ₂ (2 mass%)
Li-AG	215 °C with the generation of LiH	150 °C with the generation of Li ₂ C ₂ (3.5 mass%)

Lithium Silicon alloy

Li-Si alloys have been studied as an anode material for lithium ion battery since 1970s¹⁻²⁸⁾. Each silicon atom can accommodate 4.4 Li atom to form Li₂₂Si₅ alloy at a maximum with specific capacity of 4200 mA h g⁻¹ through several intermediate phases, which are reported as Li₁₂Si₇, Li₇Si₃, and Li₁₃Si₄ (phase diagram is shown in Figure 1-2-4¹⁻²⁹⁾). The theoretical capacity of Li-Si alloy shows the highest among the other alloying elements such as Sn, Pb, Al, Au, Pt, Zn, Cd, Ag, and Mg. Furthermore, silicon is the second most abundant element on the earth resulting in large attention for anode material of lithium ion battery. However, Li-Si alloys formation involves large volume expansion of 400 % per silicon in the case of fully inserted phase Li₂₂Si₅. Table 1-2-2 shows the crystal structure, unit cell volume, and volume per Si atom for Li-Si alloys. This volume change makes cracking and reducing electric contact, resulting in worse battery performance.

The hydrogenation and dehydrogenation properties of Li-Si alloys were investigated to destabilize LiH¹⁻³⁰⁾. It was revealed that the equilibrium pressure for LiH/Si system was increased i.e. 0.1 MPa at 490 °C. They also proposed that the stability of Li-Si alloys increases with a decrease in Li content, resulting in a lower

dehydrogenation enthalpy and a higher plateau pressure. The reversibility of the Li-Si alloy was investigated by Doi *et al.* in 2011¹⁻³¹⁾. The Li-Si alloy was prepared by milling with the initial ratio of 4Li : Si, and actual composition of obtained alloy was Li₁₅Si₄. Then, this alloy was hydrogenated and dehydrogenated with the formation of Li₁₃Si₄. The product was employed for PC (Pressure-Composition) isothermal measurements operated at 400, 450, and 500 °C. From the results of PC isothermal measurements and van't Hoff plot by the obtained results, following absorption/desorption reactions were proposed at three plateau regions:



$$\Delta H = -117 \pm 16 \text{ kJ mol H}_2^{-1}, \Delta S = -141 \pm 20 \text{ J mol H}_2^{-1} \text{ K}^{-1}$$



$$\Delta H = -99 \pm 6 \text{ kJ mol H}_2^{-1}, \Delta S = -132 \pm 8 \text{ J mol H}_2^{-1} \text{ K}^{-1}$$

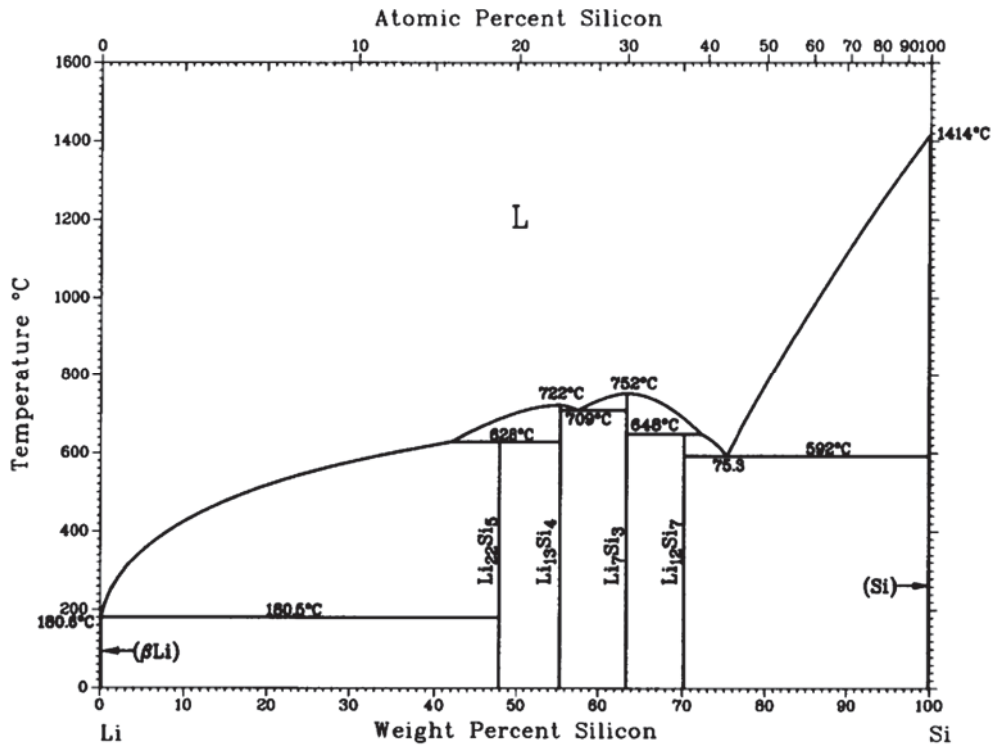


Figure 1-2-4 Phase diagram of Li-Si alloys¹⁻²⁹⁾

Table 1-2-2 Crystal structure parameters of Li-Si alloys

Compound	Crystal structure	Unit cell volume (Å ³)	Volume per silicon atom (Å ³)
Si	Cubic	160.2	20.0
Li ₁₂ Si ₇	Orthorhombic	243.6	58.0
Li ₇ Si ₃	Rhombohedral	308.9	51.5
Li ₁₃ Si ₄	Orthorhombic	538.4	67.3
Li ₂₂ Si ₅	Cubic	659.2	82.4

Lithium Germanium alloy

Germanium belongs to group 14 element and is the next element of Si. Li is inserted into Ge to form Li-Ge alloy, which has been investigated for not only the effective

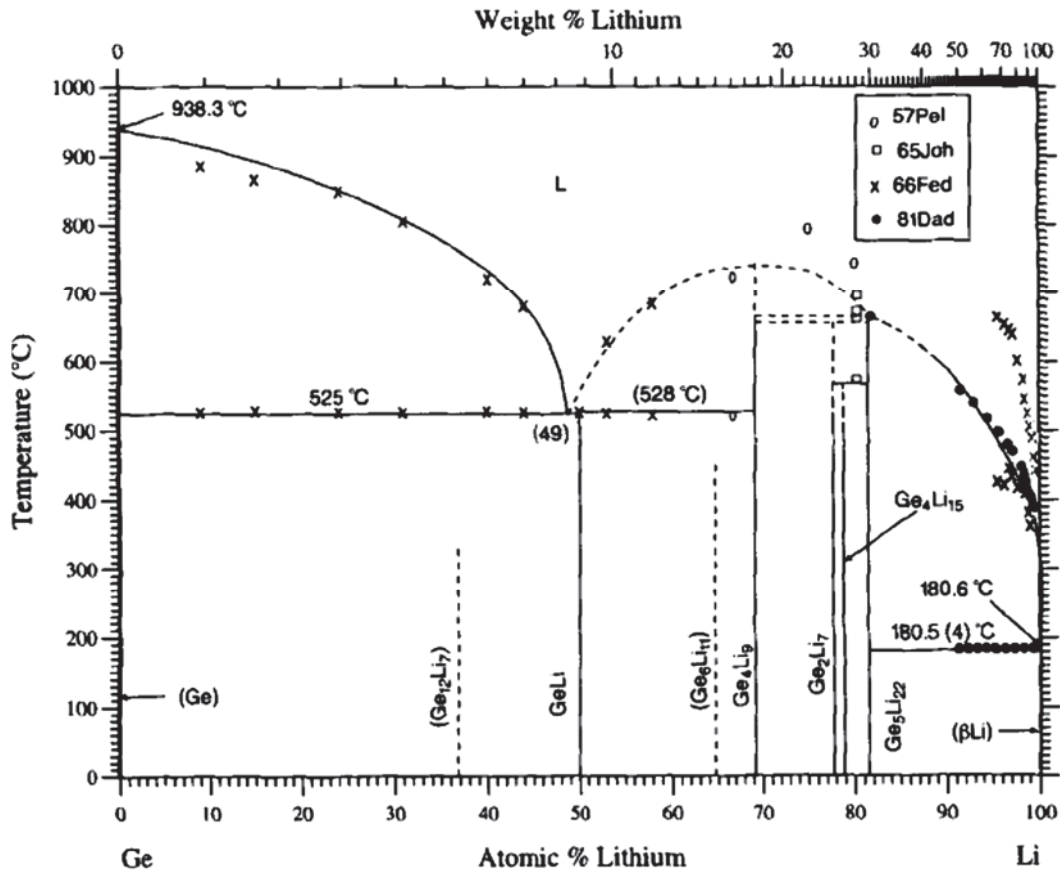
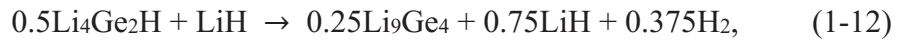


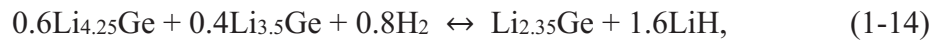
Figure 1-2-5 Phase diagram of Li-Ge alloys ¹⁻³²⁾

destabilization agent of LiH and MgH₂ but also anode electrode for Li ion battery. Several alloy phases were reported so far. A phase diagram is shown in Figure 1-2-5, and crystal structure of representative phases are shown in Table 1-2-3¹⁻³²⁾.

Two different mixture, which are 4.4LiH + Ge and 4.4Li + Ge, were prepared to examine the hydrogen absorption and desorption reaction, and then the hydrogen desorption process of LiH + Ge system was proposed¹⁻³³⁾ as follows,



It is claimed that the system reversibly storages 3 wt% of hydrogen, but there were no experimental evidence for rehydrogenation. In order to investigate hydrogenation reaction of Li-Ge system in further details, the alloy of 4.4Li + Ge was prepared as a starting material by following procedure¹⁻³⁴⁾. The ball milling process was employed, and then the mixture was annealed at 500 °C to obtain desired Li₂₂Ge₅ alloy, which is fully Li inserted phase. A recent study suggested that the stoichiometry of Li₂₂Ge₅ (Li_{4.4}Ge) structure is not true but Li₁₇Ge₄ (Li_{4.25}Ge)¹⁻³⁵⁾. The properties of synthesized alloy were investigated by the PC isotherm measurements. It was revealed that the Li-Ge system can absorb and desorb hydrogen with two step reactions. An unknown phase was observed after the first step of hydrogen absorption. However, it shows similar crystal structure to Li_{14.1}Si₆ (Li_{2.35}Si), indicating that new phase was possibly formed and assigned to Li_{14.1}Ge₆ in tetragonal structure (space group of R $\bar{3}$ m). The total reaction can be described as follow,



$$\Delta H = -143 \pm 5 \text{ kJ mol H}_2^{-1}, \Delta S = -155 \pm 7 \text{ J mol H}_2^{-1} \text{ K}^{-1}$$



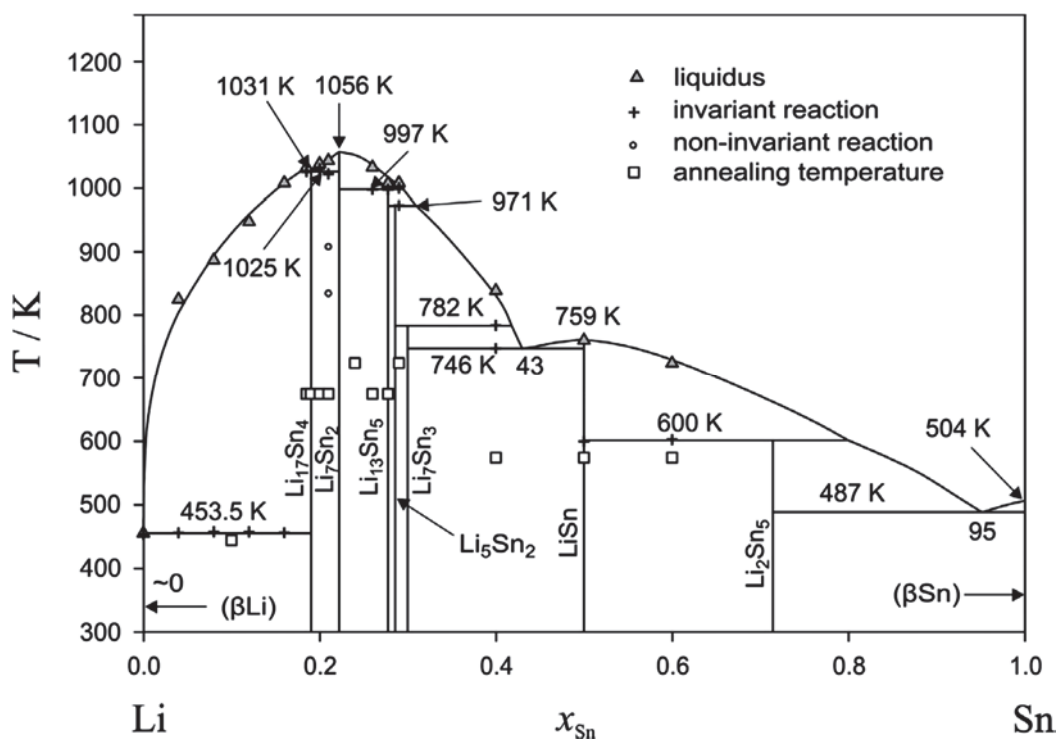
$$\Delta H = -79 \pm 6 \text{ kJ mol H}_2^{-1}, \Delta S = -117 \pm 6 \text{ J mol H}_2^{-1} \text{ K}^{-1}$$

Table 1-2-3 Crystal structure parameters of Li-Ge alloys

Compound	Crystal structure	Lattice constant (Å)
Ge	Cubic	a=0.5657
LiGe	Tetragonal	a=9.846, c=5.810
Li ₇ Ge ₂	Orthorhombic	a=8.179, b=15.135, c=4.508
Li ₁₅ Ge ₄	Cubic	a=1.0698
Li ₂₂ Ge ₅	Cubic	a=1.8859

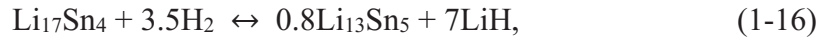
Lithium tin alloy

Li-Sn alloys are also one of candidates for anode material of lithium ion battery (LIB) because they can theoretically improve the volumetric capacity almost 2.5 times compared with graphite which is equal to 2000 mA h cm⁻³. Li-Sn alloys can possess larger amount of Li than graphite, which is anode material for LIB, and show high density of more than twice as large as the graphite, resulting such high volumetric capacity. Several phases have been already reported for Li-Sn alloys, and the phase diagram and each



crystal structure shown in Figure 1-2-6 and Table 1-2-4¹⁻³⁶⁾, respectively.

The ball milling was performed to make the mixture of Li and Sn for 3 h to synthesize $\text{Li}_{17}\text{Sn}_4$ ($\text{Li}_{4.25}\text{Sn}$), in which the phase obtained is considered as the most Li inserted Li-Sn alloy. $\text{Li}_{17}\text{Sn}_4$ reacts to H_2 with two major exothermic reaction completed up to 260 °C. The hydrogenation reaction does not reach the desired LiH and Sn, and LiSn and LiH were observed as final product in the experimental conditions. The PC isothermal experiment was also employed, suggesting that the reaction proceeds as follows¹⁻³⁷⁾,



$$\Delta H = -90 \pm 10 \text{ kJ mol H}_2^{-1}, \Delta S = -100 \pm 20 \text{ J mol H}_2^{-1} \text{ K}^{-1}$$



$$\Delta H = -37 \pm 2 \text{ kJ mol H}_2^{-1}, \Delta S = -75 \pm 3 \text{ J mol H}_2^{-1} \text{ K}^{-1}$$

The dehydrogenation reaction was investigated by using the mixture of 4.25LiH and Sn. Hydrogen were released by multistep reaction starting at 150 °C and $\text{Li}_{17}\text{Sn}_4$ was observed as the final product followed by the intermediate phase of Li_7Sn_2 , $\text{Li}_{13}\text{Sn}_5$, Li_5Sn_2 , Li_2Sn , and LiSn at 450 °C.

Table 1-2-4 Crystal structure parameters of Li-Sn alloys

Compound	Crystal structure	Lattice constant (Å)
Sn	Tetragonal	a=5.7998, c=3.1642
Li_2Sn_5	Tetragonal	a=10.274, c=3.125
LiSn	Monoclinic	a=5.17, b=3.18, c=7.74
Li_7Sn_3	Monoclinic	a=8.56, b=4.72, c=9.45
Li_5Sn_2	Trigonal	a=4.74, c=19.83
$\text{Li}_{13}\text{Sn}_5$	Trigonal	a=4.70, c=17.12
Li_7Sn_2	Orthorhombic	a=9.80, b=13.80, c=4.75
$\text{Li}_{17}\text{Sn}_4$ ($\text{Li}_{22}\text{Sn}_5$)	Cubic	a=19.6907

1-3 Application of nitride

1-3-1 Semiconductor

The group 13 nitrides such as AlN, GaN, and InN are attractive from the viewpoint of electronic device development. These nitrides possess suitable properties for practical and engineering application as semiconductor because they form solid solution phase with continuous composition and have wide band-gap range from 1.9 eV for InN, to 3.4 eV for GaN, to 6.2 eV for AlN (Figure 1-3-1¹⁻¹¹). The energy range of visible light, which is from ultraviolet to infrared, can be completely available by these nitrides. The group 13 nitrides and their alloys have been fabricated into various high-temperature and high-power microelectronics and optoelectronic devices such as integrated circuits, blue light-emitting diodes, and UV photodetectors.

Although GaN is more extensively studied than other group 13 nitrides, it is still required extensive investigation because of technologically important materials. In addition, visible light can be available by using GaN as main material and other group 13 nitrides. GaN is first synthesized in 1928¹⁻³⁸), in which it is indicated that GaN is an extremely stable compound and exhibits significant hardness. The chemical stability at high temperatures up to 800 °C¹⁻³⁹) with the hardness that GaN has regarded as attractive material for protective coating. Moreover, it is also an excellent candidate for device operation because of wide band-gap and stability under severe environments such as high temperature. The materials characteristics indeed depend on the crystalline growth conditions. In fact, the nitrides synthesized by different methods show clearly different properties.

AlN exhibits many useful properties, that is, the feasibility for utilization as practical application, due to, for example, high hardness, high thermal conductivity, resistance to high temperature, and insulation quality. For the main application except for the component of semiconductor, it is used as heat releasing material placed in electronic parts.

The first study for synthesizing InN was reported in 1938¹⁻¹⁰), in which $\text{InF}_6(\text{NH}_4)_3$ was starting material. After that, several attempts were made to synthesize

InN and it was revealed that direct interaction between metallic In and N₂ does not take place even at high temperatures. In all of the methods proposed before in 1970, the reaction between In including compound and ammonia, or thermal decomposition of complex compound composed by In and N was used to obtain InN, and the synthesized InN was in the form of powder or small crystal. After the period, the success of the growth for InN as single crystal, many kinds of techniques have been reported to apply it to semiconductor. The wavelength of LED can be controlled by alloying some materials with different bandgap. The bandgap of InN is narrower than those of other group 13 nitrides as mentioned above. This characteristic properties make it possible to adjust the bandgap for obtaining target emitting energy.

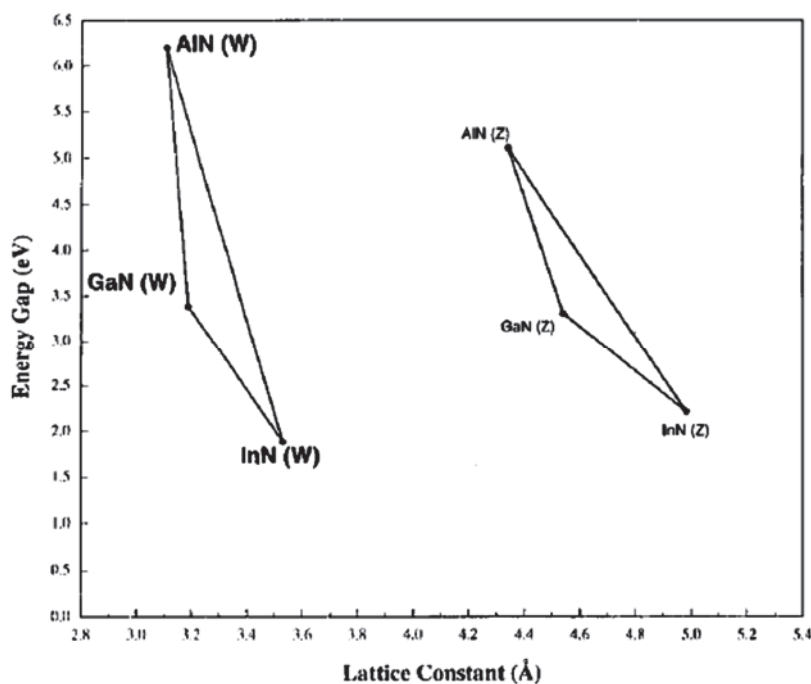


Figure 1-3-1 Bandgap versus lattice parameters for group 13 nitrides¹⁻¹¹⁾

1-3-2 Bearing

Silicon nitride (Si_3N_4) is first reported in 1859¹⁻⁴⁰⁾ and has been studied actively for more than 50 years in the field of material science. The development of Si_3N_4 ceramics was markedly accelerated in early 1960s as the potential material due to its high structural stability at high temperature. At the same time, an important breakthrough in development of Si_3N_4 came with the realization that a fully dense and much stronger form could be obtained by hot-pressing of Si_3N_4 powder. In the 1970s, the studies for Si_3N_4 have much accelerated with the objects of demonstrating the practicability of ceramic-containing gas-turbine engines. During the last 30 years, many of considerable development works on Si_3N_4 have been conducted and many different aspects of Si_3N_4 have been revealed.

There are two important properties for practical use of Si_3N_4 : one is the good resistance to thermal shock and refractoriness, and another is low friction. Much of the work was desired as dense-sintered component into a new range of advanced gas-turbine and reciprocating engines with significantly higher temperatures. Most of these components are manufactured in the United States and Japan, although considerable development works also have been conducted in Germany and the other European Union countries. The characteristic property of low friction and additional properties such as wear resistance, high stiffness, and low density of Si_3N_4 should suit to the development of high temperature and unlubricated roller and ball bearings. Friction and rolling contact fatigue rates are low, and this properties are given to Si_3N_4 bearing longer life than conventional higher-density steel and hard-metal bearings. As a result, Si_3N_4 is used at abrasive environments such as oil drilling and vacuum pumps.

1-3-3 Coating

Titanium nitride (TiN) coatings are used to improve metallic surface properties for industrial application. TiN layer with a few microns thickness is chemically stable and improves the surface scratch-proof. Its characteristic properties of high hardness, low coefficient of friction and resistance are favorable for drills and cutting tools. Moreover, its pleasing golden appearance is used for ornamental purposes such as watches and accessories. The quantity of admitted nitrogen gas determines the color of the coating. Masking of the silver-colored dental alloys by a gold-colored layer turns out to be a hot item in dentistry. Here, the gilding process produce a no wear resistant, no porous surface, indicating that TiN coating may be a good alternative. Then, application of TiN is introduced in this section, especially focused on biological, mechanical, and corrosive aspect of the coating as follows.

TiN coatings on a silver-palladium (Ag-Pd) and cobalt-chrome-molybdenum (Co-Cr-Mo) alloy showed similar biological behavior as the base materials. Compared to stainless steel, TiN was more compatible in cell culture and animal experiments. The repair of broken bone of dogs around implants coated with TiN was faster than the Co-Cr base material. In general, biocompatibility of TiN has been evaluated positively, in agreement with clinical observations.

The investigations of mechanical properties of TiN coating are commonly carried out on the wear and strength of the coating, and the combination of TiN and underlying alloys. It was clarified that wear characteristics of TiN are good but seem to depend on the coating thickness.

The good corrosion resistance is made by the formation of a protective surface layer of TiN.

1-3-4 Nitrogen source for nitride synthesis: ammonia (NH₃)

As mentioned 1-2 section, high temperature and/or large energy supply should be necessary to directly dissociate nitrogen triple bond of N₂ molecules. Therefore, exploring effective catalyst to realize mild condition for nitride synthesis is required and a lot of techniques have been discussed so far. From a different point of view, ammonia is suggested that one of ways for the use of nitrogen source. NH₃ shows weak N-H bond energy (389 kJ mol⁻¹)¹⁻⁴¹⁾ compared with N₂ molecule itself (945 kJ mol⁻¹), indicating that the N-H bond can be easily cleavage and an atomic state of nitrogen should be easily produced. Namely, ammonia is the potential material as nitrogen source to synthesize nitrides. On the other hand, NH₃ should be also synthesized from N₂ and H₂ gases because it is not enough amount in nature for industrial use.

It has passed over 100 years since a publication of first report about ammonia synthesis¹⁻⁴²⁾, and after that, numerous studies for ammonia synthesis catalyst have been reported such as iron-based catalyst, ruthenium-based catalyst, and electride. Haber-Bosh process was first industrialized in 1931 and drastically developed with large demand of fertilizer. Many kinds of catalysts were surveyed, and finally, BASF Co. found the industrially effective catalyst, which is Fe₃O₄ based material added with Al₂O₃ and K₂O. For the mass production, the NH₃ synthesis is operated under high pressure of 20-35 MPa and high temperature of 500 °C. It is acceptably understood that Al₂O₃ is composed as a catalyst to prevent sintering during reaction. K₂O have been believed as its electron donating nature, which changes main adsorbed species from N to NH and accelerate the dissociation of nitrogen molecule. In fact, ammonia synthesis rate is improved with adding K₂O to Fe-Al₂O₃, accompanying the decrease of work function around an iron surface^{1-43, 44)}. Aika *et al.*¹⁻⁴⁵⁾ reported that ammonia synthesis rate can be accelerated by an addition of ruthenium, and furthermore, it can be remarkably improved when ruthenium is supported by potassium. After the publication of this report, ruthenium (Ru)-including materials have attracted much attention as potential catalyst as researching topics for promoting material and support material. On the Basis of catalytic behavior for Ru, American company have started mass production of ammonia by using the optimized Ru catalyst, which technique is called Kellogg method, from in 1992, and these plant

are running around 7 countries at present ¹⁻⁴⁶). Electron-donating nature is considered to play an important role for promoting ammonia synthesis, and alkali metals such as Cs, K, and Na show distinct effect. Novel electron donor supporting a ruthenium, which is called Ru-loaded electride $[\text{Ca}_{24}\text{Al}_{28}\text{O}_{64}]^{4+}(\text{e}^-)^4$ (Ru/C₁₂A₇:e⁻) instead of alkali metal was first reported by Kitano *et al.* in 2012 ¹⁻⁶). Work function of electride is smaller than that of ruthenium metal, resulting in superior catalytic effect, and besides, that ability is better than other ruthenium-based materials at 400 °C with a pressure of 0.1 MPa (Figure 1-3-2). Exploration of promising electron donor alternative to alkali metal is still ongoing, and ammonia synthesis reaction can be realized even at 200 °C by using ruthenium-loaded dicalcium nitride $[\text{Ca}_2\text{N}^+]\cdot\text{e}^-$ as catalyst ¹⁻⁴⁷). The superior catalytic effect of Ru is admitted with no doubt, however, it is not easily accepted from the aspect of cost.

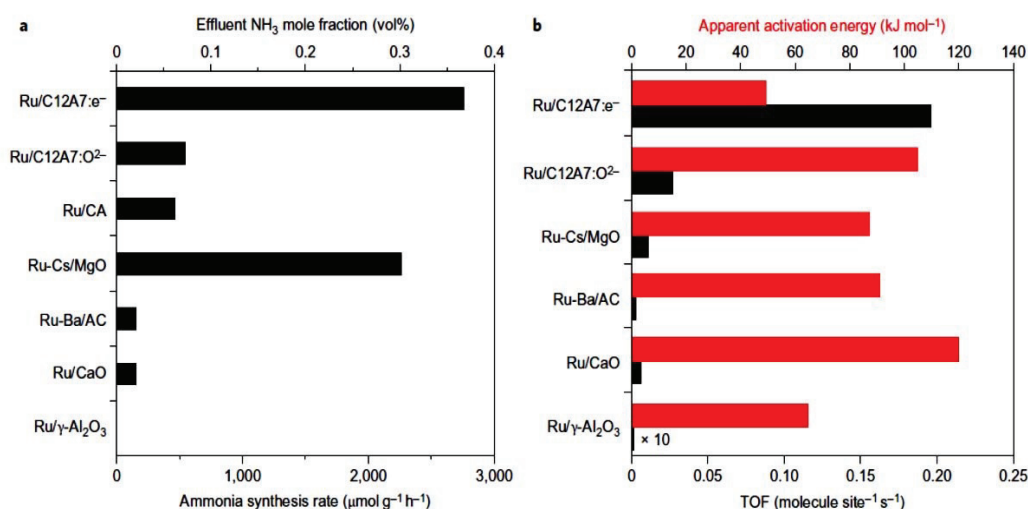


Figure 1-3-2 Catalytic performance of Ru/C12A7:e⁻ at atmospheric pressure. (a) Ammonia synthesis rate and ammonia effluent mole fraction at 400 °C over various 1 wt% Ru-loaded catalysts, (b) Turnover frequencies (TOFs: upper bars) and apparent activation energies (bottom bars) for ammonia synthesis at 400 °C over various 1 wt% Ru-loaded catalysts. Reaction condition: catalyst, 0.2 g; synthesis gas, H₂/N₂=3 with a flow rate of 60 ml min⁻¹; pressure, 0.1 MPa; temperature, 400 °C. An error analysis was performed for these data and the error range found was ±5 %. ¹⁻⁶

1-3-5 Energy (hydrogen) carrier and storage

Ammonia (NH₃)

The global consumption of primary energy has been drastically increased since the “Industrial Revolution” began in the 18th century. There are many kinds of primary energy; fossil energy, nuclear energy, and natural energies such as wind power, solar light, geothermal power, and so on. In Japan, our lives strongly depend on fossil energy as well as 90 % of primary energy consumption in 2011. Anyway, global society is facing serious environmental problems such as air pollution, global warming, and exhaustion of fossil fuels. Therefore, establishment and development of a carbon free and sustainable society are desired. To promote the utilization of renewable energy, sustainable energy system is proposed with the electrical energy as secondary energy. However, it is difficult to store and transport a great deal of electrical energy in the long term. Recently, hydrogen has attracted much attention as an energy carrier because of its advantages such as high gravimetric density, carbon free, suitability for mass storage and transportation. However, gaseous hydrogen is much voluminous, resulting in low volumetric energy density. Table 1-3-1 shows the characteristics of liquid hydrogen, organic hydride, and liquid ammonia. One of the solution, ammonia is recognized as promising hydrogen storage and carrier due to its high hydrogen density (17.8 mass%), which is more than two times higher than those of organic hydrides. Besides, the volumetric hydrogen density of liquid ammonia is 1.5 times higher than that of liquid hydrogen, and ammonia can be easily liquefied by

Table 1-3-1 Characteristics of liquid hydrogen, organic hydrogen, and liquid ammonia

Physical property	Ammonia	Decalin	Methylcyclohexane	Liquid hydrogen
	NH ₃	C ₁₀ H ₁₂	C ₇ H ₁₄	H ₂
Molecular weight (g/mol)	17.03	132.20	98.19	2.02
Density (g/cm ³)	0.603*	0.97	0.769	0.0706
Gravimetric hydrogen density (mass %)	17.8	7.29	6.16	100
Volumetric hydrogen density (kg/100 L)	10.7	7.07	4.73	7.06

* at 1.0 MPa, 298 K

Table 1-3-2 Ammonia absorption amount (n) and equilibrium pressure at plateau (P_{eq}) of all samples at 293 K ¹⁻⁵¹⁾

reaction	n (mol NH ₃ / mol material)	P_{eq} (MPa)	x_p difference ^a
LiF + n NH ₃ \rightleftharpoons LiF(NH ₃) _{n}		> 0.800	3.00
LiCl + 4NH ₃ \rightleftharpoons LiCl(NH ₃) ₄	4	0.178	2.18
LiBr + 2NH ₃ \rightleftharpoons LiBr(NH ₃) ₂	2	< 0.001	1.98
CaF ₂ + n NH ₃ \rightleftharpoons CaF ₂ (NH ₃) _{n}		> 0.800	2.98
CaCl ₂ + 8NH ₃ \rightleftharpoons CaCl ₂ (NH ₃) ₈	8	0.030	2.16
NaI + 5NH ₃ \rightleftharpoons NaI(NH ₃) ₅	5	0.055	1.73
NiCl ₂ + 6NH ₃ \rightleftharpoons NiCl ₂ (NH ₃) ₆	6	< 0.001	1.25
NiBr ₂ + 6NH ₃ \rightleftharpoons NiBr ₂ (NH ₃) ₆	6	< 0.001	1.05
NaCl + n NH ₃ \rightleftharpoons NaCl(NH ₃) _{n}		> 0.800	2.23
KBr + n NH ₃ \rightleftharpoons KBr(NH ₃) _{n}		> 0.800	2.14
MgF ₂ + n NH ₃ \rightleftharpoons MgF ₂ (NH ₃) _{n}		> 0.800	2.67
LiBH ₄ + 3NH ₃ \rightleftharpoons LiBH ₄ (NH ₃) ₃	3	< 0.001	
NaBH ₄ + 2NH ₃ \rightleftharpoons NaBH ₄ (NH ₃) ₂	2	0.090	
KBH ₄ + n NH ₃ \rightleftharpoons KBH ₄ (NH ₃) _{n}		> 0.800	
Ca(BH ₄) ₂ + 5NH ₃ \rightleftharpoons Ca(BH ₄) ₂ (NH ₃) ₅	5	< 0.001	
MgBH ₄ + 5NH ₃ \rightleftharpoons MgBH ₄ (NH ₃) ₅	5	< 0.001	

compressing up to 0.87 MPa at 20 °C ¹⁻⁴⁸⁾. Besides, the attractive advantage of ammonia as hydrogen storage material is that infrastructure is already established because ammonia is commercialized as fertilizer of chemicals all over the world. In Cross-ministerial Strategic Innovation Promotion Program (SIP), the national project starts in 2014 ¹⁻⁴⁹⁾ to focus on the development of energy carrier system by means of ammonia. In this project, a roadmap proposed to establish hydrogen society, ammonia is regard as the most important hydrogen carrier, and many research groups are investigating elemental technologies to effectively utilize ammonia from fundamental research to practical use.

To realize the effective transportation of ammonia, main issue is how to compactly and safely store ammonia. For example, ammonia can be stored more compactly than liquid state of ammonia if suitable ammonia absorbing material is chosen, and moreover, partial pressure of ammonia gas is also decreased. Aoki *et al.* systematically investigated ammonia absorption properties of metal halides and

borohydrides by pressure-composition-isothermal measurements^{1-50, 51)} as shown in Table 1-3-2.

As mentioned above, ammonia is regarded as a promising hydrogen carrier so ammonia should be decomposed depending on the demands as energy. Electrochemical process is one of the promising method to decompose ammonia with the generation of hydrogen at moderate temperature. It was reported that ammonia can be decomposed in alkaline solution by electrolysis at room temperature, however the gravimetric hydrogen density is as low as 6.1 mass% according to its solubility to water, 34.2 mass% at 20 °C. Thus, direct electrolysis of liquid ammonia is the simplest way and is investigated by Hanada *et al.*, where alkaline metal amide (MNH_2 : $M=Li, Na, K$) was used as a supporting electrolyte^{1-52, 53)}. As a results, it was clarified that ammonia electrolysis proceeded with higher reaction rate in the order of solubility of MNH_2 in liquid ammonia because current density clearly depends on the solubility, resulting in higher concentration of NH_2^- in liquid ammonia. However, the experimental electrolysis voltage to obtain realistic reaction rate requires more than 1 V, which is still high for practical use. In addition, the anode electrode was corroded after the electrolysis process. The direct electrolysis using supporting electrolyte MNH_2 should be effective technique to obtain hydrogen from ammonia if the above issues are solved.

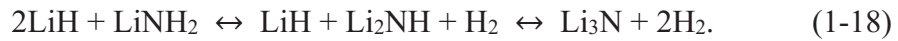
Nitrogen atoms in ammonia is useful as nitrogen source for the synthesizing process of nitrides. For instance, as the practical application to synthesis process of gallium nitride (GaN), ammonia is widely used as nitrogen source. As represented nitride synthesis, the thermochemical reactions with the use of ammonia is called “ammonothermal reaction”, the detailed synthesis process is described at later parts.

Hydrogen storage system based on nitrides

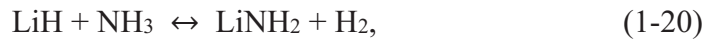
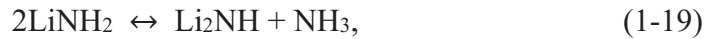
Amide and imide

Solid state hydrogen storage materials composed of light elements such as alkali (-earth) metals, carbon, and nitrogen have attracted much attention as well. These materials show high gravimetric hydrogen density, which is roughly 5-20 wt% and higher than 1-3 wt% of conventional hydrogen storage alloys^{1-54, 55)}. As N-including hydrogen

storage materials, alkali metal and alkali earth metal amides (MNH_2 : $M=Li, Na, K, Mg, Ca$) and those imide (M_2NH) were typical ones. MNH_2 consists of ionic bond between cation M^+ and anion NH_2^- . For NH_2^- anion, a chemical bond between N and H atoms is stabilized by covalent bonds. As the same points of view, M^+ and NH^- in imide M_2NH makes ionic bond of with the covalent bond of N and H atom. These nitride based hydrogen storage systems, which is called as amide-imide ($M-N-H$) systems, have been widely studied after the first report by P. Chen *et al.* in 2002¹⁻⁵⁶. The $M-N-H$ systems are basically composed of two solid phases, which are amide and hydride. So far, various types of amide-imide system are reported such as Li-Mg-N-H, Ca-N-H^{1-56, 57}. In the case of Li-N-H system, large amount of hydrogen, 10.4 wt%, can be stored by reversible reactions. The reaction is described as follow,



For the first reaction, which is expressed by $LiH + LiNH_2 \leftrightarrow Li_2NH + H_2$, the catalytic effects on hydrogen desorption properties were investigated by the addition of Fe, Co, Ni metal, $TiCl_3$, and VCl_3 ¹⁻⁵⁸. The best hydrogen desorption properties were shown when 1 mol% of $TiCl_3$ was added to the mixture of LiH and $LiNH_2$. The 5.5 to 6.0 wt% of hydrogen was practically available below 250 °C, where the theoretical capacity is 6.5 wt%. It showed high reversibility higher than 5 wt% even after 3rd cycles. The reaction mechanism was proposed about hydrogen desorption reaction, which can be explained following ammonia mediated reactions¹⁻⁵⁹⁻⁶²,



Among the $M-N-H$ systems, the $8LiH-3Mg(NH_2)_2$ system can be considered as the most potential hydrogen storage material because more than 5.5 mass% of hydrogen can be reversibly absorbed and desorbed at 150 °C, where the hydrogen capacity and operating temperature achieves the NEDO targets^{1-63, 64}. Therefore, the above $M-N-H$ systems are recognized promising hydrogen storage materials and further developed in future.

The one of elemental reaction (eq. 1-20) is also considered as the nitride based hydrogen storage system. The hydrogen capacity of the NH_3 and LiH system is 8.1 wt%. So far, the hydrogen generation and regeneration reactions of the gaseous NH_3 and alkali

metal hydrides (M_1H : $M_1=Li, Na, \text{ and } K$) system are systematically investigated^{1-65, 66}. The K system revealed that highest reactivity for the hydrogenation and regeneration with the reversible hydrogen storage almost 100 % of the reaction yield. The reactivity of the Li system is very poor in spite of its high hydrogen density. To improve the reaction kinetics, addition of catalysts are desirable. Generally, transition metal or its compounds are generally utilized as catalyst to improve the kinetic properties for dissociation of gaseous molecules in gas-solid reactions, where it is expected that electrons possessed around valence level can affect the reaction. However, the effective catalysts for this system are proposed from the other point of view. Miyaoka *et al.* reported the catalytic effects without the components of transition metals in 2015¹⁻⁶³). The reaction yield for hydrogen generation reaction (eq. 1-20) was drastically improved by adding ammonia absorbing materials as catalyst. Especially in the case of $NaBH_4$, the ammonia absorbing reaction can be proceeded as shown eq. 1-21¹⁻⁵¹), the reaction yield surpassed 90 % for 12 h, although the reaction yield was less than 50 % for 12 h without catalyst.



where, the reaction mechanism could be considered as follow. Ammonia is condensed in ammonia absorbing materials with keeping high mobility because ammine complex show high entropy value S^0 . This phenomena result in the improvement of kinetic properties such as frequency factor.

As described above, the nitrides such as amide, imide, and ammonia are potential materials in the hydrogen storage field. However, as shown in eq. (1-18), (1-19), and (1-20), these materials show complicated processes including solid-solid reaction and phase separation. Particularly, the reaction processes of the Na and K systems are more complicated because phase transition such as melting also includes as intermediate reactions. In addition, imide and nitride phases are not reported for the Na and K systems differently from the Li system. Therefore, the research to understand the details of reaction mechanism are necessary for development of light elements based hydrogen storage materials.

1-4 Thermodynamics and kinetics

Thermodynamics

It is well known that nitrogen from various compounds with the other elements. For example, in the case of alkali(-earth) metals, ionic bond can be formed with N, in which nitrogen atom exists as N^{3-} . Typically, these chemical bonds consist of stoichiometric ratio. On the other hands, the bonds between N and group 3-7 elements are basically covalent. When transition metals react to nitrogen, nitride phase is formed with keeping its metallic behavior over non-stoichiometric composition, which is called “metal-nitrogen alloys”. This section focuses on the thermodynamics of metal-nitrogen ($M-N$) system.

Nitrogen can be dissolved and go into the crystal lattice of base metal without changing the crystal structure. When the concentration of nitrogen increases in the base metal, nitride phase is formed with structural change. Here, a certain metal can absorb nitrogen gas if the metal is kept in the nitrogen atmosphere and the reaction reaches equilibrium condition. Then, the concentration of nitrogen in the metal should be expressed as a function of temperature and nitrogen pressure.

Generally, the thermodynamics for a reaction between metal and nitrogen, which is named nitrogenation, is explained as follows.

The equilibrium condition between gaseous nitrogen and nitrogen atom dissolved in a metal can be expressed as the following reaction,



Under the equilibrium condition, chemical potential of the molecular nitrogen gas μ_g is equal to that of nitrogen atoms in nitride μ_a ,

$$\frac{1}{2} \mu_g(T, p) = \mu_a(T, p, x), \quad (1-23)$$

where, the gaseous nitrogen is assumed as an ideal gas in low pressure range. Therefore, the chemical potential of nitrogen gas is led by using partition function Z for translational, vibrational, and rotational motions (Z_t , Z_v , and Z_r) of ideal diatomic molecule, which is based on statistical thermodynamics, as the following equation,

$$\begin{aligned}\mu_g(T, p) &= k_B T \ln(Z_t \cdot Z_v \cdot Z_r) - E_d, \\ &= kT \ln\left(\frac{p}{p_0(T)}\right) - E_d,\end{aligned}\quad (1-24)$$

$$P_0(T) = \frac{16(\pi k)^{\frac{7}{2}} M_0^{\frac{5}{2}} r_0^2}{h^5} T^{\frac{7}{2}}, \quad (1-25)$$

in which k_B is the Boltzmann constant, E_d is the dissociation energy of nitrogen molecules, M_0 is the mass of nitrogen gas, r_0 is the distance between nitrogen atoms, and h is Planck's constant.

The chemical potential of nitrogen atoms in metal is defined by Gibbs free energy, which is expressed assuming the amount of nitrogen atoms n as follow,

$$\mu_a = \frac{\partial G}{\partial n}, \quad (1-26)$$

$$\Delta G = \Delta H - T\Delta S, \quad (1-27)$$

where the enthalpy change ΔH and entropy change ΔS can be approximated as follow,

$$\Delta H = -nE_a, \quad (1-28)$$

$$\Delta S = \Delta S_{\text{vib}} + \Delta S_c, \quad (1-29)$$

$$\Delta S_{\text{vib}} = nS_a, \quad (1-30)$$

$$\Delta S_c = k_B \ln\left(\frac{r!}{x!(r-x)!}\right), \quad (1-31)$$

where E_a and S_a are enthalpy and entropy for an atom, respectively, ΔS_{vib} is entropy change of vibration mode due to the nitrogen, ΔS_c is entropy to distribute the nitrogen atom into metal, r ($=N/N_0$) is the number of N atoms per metal atom N_0 , which can be fully occupied by nitrogen atoms after complete nitride formation, and x ($=n/N_0$) is the number of nitrogen atoms per metal atom. Then, eq. (1-26) should be rearranged as follow,

$$\begin{aligned}\mu_a &= \frac{\partial G}{\partial n}, \\ &= -E_a - TS_a + K_B T \ln\left(\frac{x}{r-x}\right),\end{aligned}\quad (1-32)$$

then, as expressed above, chemical potential of nitrogen gas and that of nitrogen atom in the metal is shown by eq. (1-23),

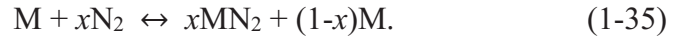
$$\left\{ \frac{1}{2} K_B T \ln \left(\frac{P}{P_0(T)} \right) - E_d \right\} = -E_a - TS_a + K_B T \ln \left(\frac{x}{r-x} \right), \quad (1-33)$$

assuming the low nitrogen concentration in the metal ($x \ll 1$),

$$\begin{aligned} \sqrt{\frac{P}{P_0(T)}} &= x \cdot K_s(T), \\ K_s(T) &= \exp \left(- \frac{S_a T - 1/2 E_d + E_a}{K_B T} \right). \end{aligned} \quad (1-34)$$

This is known as Sievelt's law.

Assuming that nitrogenation reaction between nitrogen gas and metal is proceeded with the formation of nitride, the equilibrium for the formation of metal nitride MN_2 is expressed as follow,



And then, the Gibbs's free energy can be described by the enthalpy change ΔH and entropy change ΔS ,

$$\Delta G = \Delta H - T\Delta S = 0, \quad (1-36)$$

$$\Delta H = T\Delta S. \quad (1-37)$$

where the entropy of gaseous nitrogen S_{N_2} can be separated into the standard entropy $S_{N_2}^0$, which is the standard entropy of nitrogen molecule at 0.1 MPa, and the entropy change of nitrogen gas can be shown by following equation,

$$S_{N_2} = S_{N_2}^0 - R \ln \left(\frac{P_{eq}}{p_0(T)} \right), \quad (1-38)$$

where R is gas constant and p_{eq} is the equilibrium pressure. Therefore, ΔS is rearranged as follow by using the entropy of nitride S_{MN_2} and metal S_M ,

$$\Delta S^0 = S_{MN_2} - S_M - S_{N_2}^0, \quad (1-39)$$

finally, following equation can be obtained,

$$\ln \left(\frac{P_{eq}}{p_0(T)} \right) = \frac{\Delta H}{RT} - \frac{\Delta S^0}{R}. \quad (1-40)$$

This equation is called van't Hoff equation. Thus, the enthalpy change and the entropy

change of nitrogenation reaction can be obtained from the slope and intercept of $\ln(p_{eq}/p_0(T))$ versus $1/T$.

When the above metal M was alloyed with a metal atom X, M_nX alloy could react with nitrogen, leading to the metal nitride MN_2 and other alloy phase $M_{n-1}X$ generation. The reaction is expressed as follow,



This reaction is called conversion reaction

Gibbs's free energy shown in eq. (1-36) can be applied to general chemical reaction. Supposing that a decomposition reaction can be proceeded with the formation of solid phase and gaseous phase, the reaction should be expressed as follow,



and then, Gibbs's free energy should be described as follows,

$$\Delta G_{A \rightarrow B+C} = (H_B + H_C - H_A) - T(S_B + S_C - S_A), \quad (1-43)$$

Here, the entropy is separated into the standard enthalpy S^0 and the function of gas pressure as follow,

$$S = S^0 - R \ln \left(\frac{P}{P_0(T)} \right), \quad (1-44)$$

where P is partial pressure of each materials, $P_0(T)$ is the standard pressure. The solid material should not have the partial pressure, resulting in cancellation of the pressure term. Then, eq. (1-43) can be rearranged as follow,

$$\begin{aligned} \Delta G_{A \rightarrow B+C} &= (H_B + H_C - H_A) - T(S_B + S_C - S_A), \\ &= \Delta H_{A \rightarrow B+C} - T\Delta S_{A \rightarrow B+C} + RT \ln \left(\frac{P_C}{P_0(T)} \right). \end{aligned} \quad (1-45)$$

If this reaction is endothermic reaction ($\Delta H > 0$), the decomposition thermodynamically proceeds by satisfying the specific temperature. As another way, by continuously removing the generated gases from the reaction field ($P_C \rightarrow 0$), the required reaction temperature is decreased. This condition is generally called as “non-equilibrium state”. In experiments using carrier gas and dynamic vacuum, the reactions proceeds under non-equilibrium states.

Kinetics

Reaction kinetics for nitrogen absorption with metal largely depends on the interaction with the metal surface. Some kinetic energy barriers exist and the interaction energy U can be expressed a function of Z , which is the distance between nitrogen molecule and metal surface¹⁻⁶⁷). U potential is generally explained following four steps,

1. Adsorption step

In this step, U is given the sum of van der Waals' force (attractive force) and the electron repulsion, which is caused by the interaction between fully filled orbital of nitrogen and valence orbital of metal. The nitrogen is temporally trapped on the minimum potential point E_p (Figure 1-4-1 (a)).

2. Chemisorption step

The adsorbed nitrogen molecule is dissociated into nitrogen atoms on the surface of metal. Valence energy of metal nitride should be decreased and stabilized by the interaction between d orbital electron of metal and $2p$ orbital electrons of nitrogen. Then, nitrogen can be strongly trapped on E_{ch} (Figure 1-4-1 (b)). Figure 1-4-1 (c) is superimposed image obtained from Figure 1-4-1 (a) and Figure 1-4-1 (b). The point P is the intersection of each figures. If the point P placed below the zero potential, absorbed nitrogen can be chemisorbed without large energy change (Figure 1-4-1 (d)). On the other hands, when the point P is above zero potential, the activation energy E_{ad}^* is required to form the chemisorption state as shown in Figure 1-4-1 (e).

3. Diffusion step

The dissolved nitrogen atom goes into the bulk through interstitial site in the metal (Figure 1-4-2). The diffusion phenomena in the metal are expressed by moving of nitrogen atoms toward next interstitial site. Assuming that an atom overcomes the potential by receiving heat energy from lattice vibration of the metal, diffusion rete (D) should be expressed as follow,

$$D = d^2 \nu_D \exp\left(-\frac{E_a}{k_B T}\right), \quad (1-46)$$

where ν_D is frequency of lattice vibration, d is distance of each interstitial sites, E_a is activation energy, and k_B is Boltzmann constant.

4. Nitride forming step

When the local nitrogen concentration exceeds a certain limit, atomic rearrangement should be occurred to make stabilized state, resulting in the crystal change.

Considering the kinetics of nitrogen related reaction, N_2 dissociation on the surface and diffusion step should be rate-limiting because nitrogen molecule is formed by the strong triple bond and atomic size of nitrogen is large. Especially, in the case of reactions between light elements such as alkali metals and N_2 , it is expected the alkali metals and their compounds are often formed by ionic bond with closed-shell electronic state, resulting in inactive surface for N_2 dissociation. Furthermore, the diffusion of N atoms in bulk is more difficult compared with the compounds based on transition metals because the rearrangement process for nitride formation requires diffusion of all the elements for long distance.

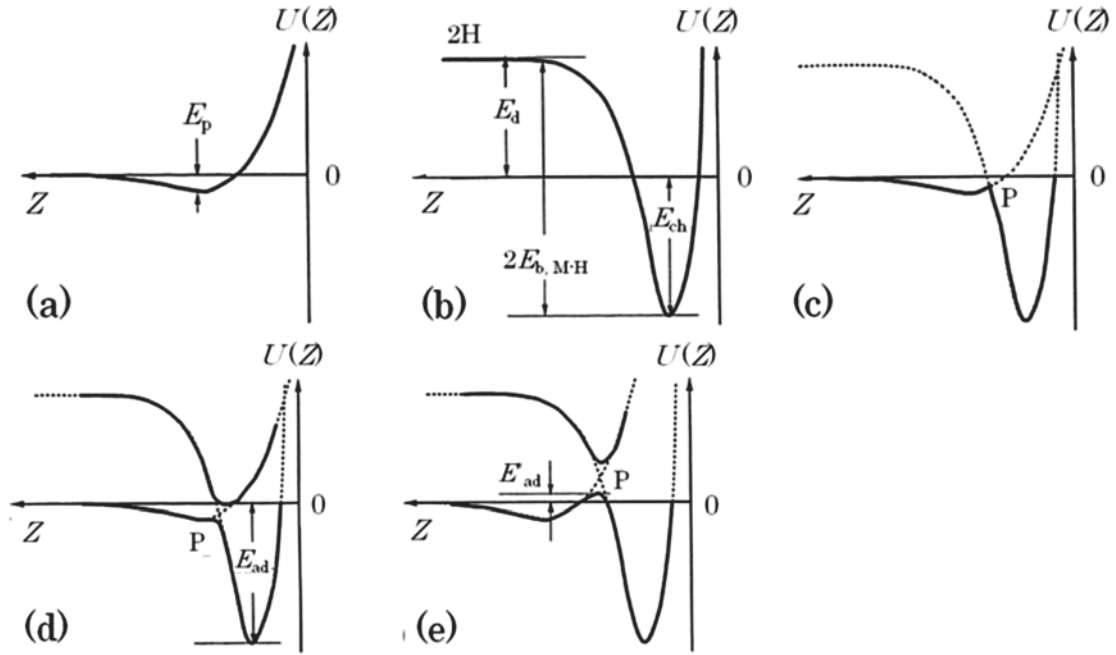


Figure 1-4-1 Interaction energy between hydrogen and metals versus the distance between hydrogen and metal surface, where these phenomena should be applied to nitrogen case ¹⁻

67)

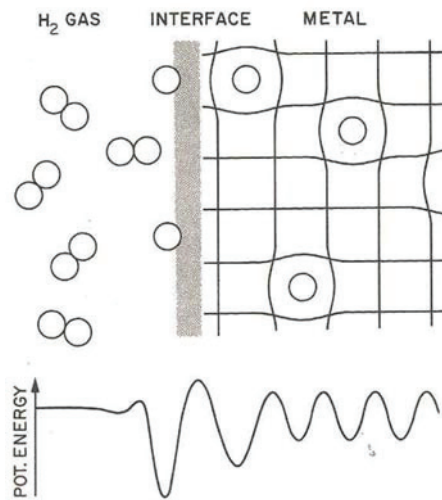


Figure 1-4-2 Simplified model of the dissociation of molecular hydrogen at an interface and solution of hydrogen atoms in the bulk with the potential energy curves ¹⁻⁶⁸). Same behavior is assumed to nitrogen

Reference

- 1-1. Karpiński, J. and S. Porowski, Journal of Crystal Growth **66**, 11-20, (1984)
- 1-2. Mohammad, S.N. and H. Morkoç, Progress in Quantum Electronics **20**, 361-525, (1996)
- 1-3. Karpiński, J., J. Jun and S. Porowski, Journal of Crystal Growth **66**, 1-10, (1984)
- 1-4. Unland, J., B. Onderka, A. Davydov and R. Schmid-Fetzer, Journal of Crystal Growth **256**, 33-51, (2003)
- 1-5. Japan Oil, Gas and Metals National Corporation: JOGMEC, <http://www.jogmec.go.jp/>,
- 1-6. Kitano, M., Y. Inoue, Y. Yamazaki, F. Hayashi, S. Kanbara, S. Matsuishi, T. Yokoyama, S.-W. Kim, M. Hara and H. Hosono, Nat Chem **4**, 934-940, (2012)
- 1-7. Kitano, M., S. Kanbara, Y. Inoue, N. Kuganathan, P.V. Sushko, T. Yokoyama, M. Hara and H. Hosono, Nat Commun **6**, (2014)
- 1-8. Grzegory, I., J. Jun, S. Krukowski, M. Boćkowski and S. Porowski, Physica B: Condensed Matter **185**, 99-102, (1993)
- 1-9. Powell, R.C., N.-E. Lee, Y.-W. Kim and J.E. Greene, Journal of Applied Physics **73**, 189-204, (1992)
- 1-10. Bhuiyan, A.G., A. Hashimoto and A. Yamamoto, Journal of Applied Physics **94**, 2779-2808, (2003)
- 1-11. Neumayer, D.A. and J.G. Ekerdt, Chemistry of Materials **8**, 9-25, (1996)
- 1-12. F.K. van Dijen, A. Kerber, Uwe Vogt, W. Pfeifer and M. Schulze, Scientific.net by Trans Tech Publications Ltd **89-91**, 19-28, (1993)
- 1-13. Wagman, D.D., W.H. Evans, V.B. Parker, R.H. Schumm and I. Halow, J. Phys. Chem. Ref. Data, **11**, (1982)
- 1-14. White, G.V., K.J.D. Mackenzie and J.H. Johnston, Journal of Materials Science **27**, 4287-4293, (1992)
- 1-15. Li, J., L. Gao, J. Sun, Q. Zhang, J. Guo and D. Yan, Journal of the American Ceramic Society **84**, 3045-3047, (2001)
- 1-16. Jacobsen, C.J.H., S. Dahl, B.S. Clausen, S. Bahn, A. Logadottir and J.K. Nørskov, Journal of the American Chemical Society **123**, 8404-8405, (2001)

- 1-17. Kojima, R. and K.-i. Aika, Chemistry Letters **29**, 912-913, (2000)
- 1-18. Jacobsen, C.J.H., Chemical Communications, 1057-1058, (2000)
- 1-19. Boisen, A., S. Dahl and C.J.H. Jacobsen, Journal of Catalysis **208**, 180-186, (2002)
- 1-20. Kamoi, K., T. Arakawa, T. Hayatsu and H. Hasuo, *Production method of lithium nitride*, in *Japanese Patent*. 2001: Japan.
- 1-21. Arakawa, T. and I. Takizawa, *Production method of lithium nitride*, in *Japanese Patent*. 2002: Japan.
- 1-22. Tokoyoda, K., S. Suzuki and T. Hatsumori, *Method for producing metal nitride*, in *Japanese Patent*. 2012: Japan.
- 1-23. Janot, R., J. Conard and D. Guérard, Carbon **39**, 1931-1934, (2001)
- 1-24. Imanishi, N., K. Kumai, H. Kokugan, Y. Takeda and O. Yamamoto, Solid State Ionics **107**, 135-144, (1998)
- 1-25. Chung, D.D.L., Journal of Materials Science **37**, 1475-1489, (2002)
- 1-26. Miyaoka, H., W. Ishida, T. Ichikawa and Y. Kojima, Journal of Alloys and Compounds **509**, 719-723, (2011)
- 1-27. Billaud, D., E. McRae and A. Hérold, Materials Research Bulletin **14**, 857-864, (1979)
- 1-28. Kasavajjula, U., C. Wang and A.J. Appleby, Journal of Power Sources **163**, 1003-1039, (2007)
- 1-29. Okamoto, H., Bulletin of Alloy Phase Diagrams **11**, 306-312, (1990)
- 1-30. Vajo, J.J., F. Mertens, C.C. Ahn, R.C. Bowman and B. Fultz, The Journal of Physical Chemistry B **108**, 13977-13983, (2004)
- 1-31. Doi, K., S. Hino, H. Miyaoka, T. Ichikawa and Y. Kojima, Journal of Power Sources **196**, 504-507, (2011)
- 1-32. Sangster, J. and A.D. Pelton, Journal of Phase Equilibria **18**, 289-294, (1997)
- 1-33. Abbas, M.A., D.M. Grant, M. Brunelli, T.C. Hansen and G.S. Walker, Physical Chemistry Chemical Physics **15**, 12139-12146, (2013)
- 1-34. Jain, A., E. Kawasako, H. Miyaoka, T. Ma, S. Isobe, T. Ichikawa and Y. Kojima, The Journal of Physical Chemistry C **117**, 5650-5657, (2013)

- 1-35. Goward, G.R., N.J. Taylor, D.C.S. Souza and L.F. Nazar, *Journal of Alloys and Compounds* **329**, 82-91, (2001)
- 1-36. Li, D., S. Fürtauer, H. Flandorfer and D.M. Cupid, *Thermodynamic assessment and experimental investigation of the Li-Sn system*. 2014. p. 181-195.
- 1-37. Jain, A., H. Miyaoka, T. Ichikawa and Y. Kojima, *Correlation between electrochemical behavior and hydrogen storage properties of Li-Sn system*, in *SI : MH2012*. 2013. p. S211-S215.
- 1-38. Johnson, W.C., J.B. Parson and M.C. Crew, *The Journal of Physical Chemistry* **36**, 2651-2654, (1931)
- 1-39. Pisch, A. and R. Schmid-Fetzer, *Journal of Crystal Growth* **187**, 329-332, (1998)
- 1-40. Riley, F.L., *Journal of the American Ceramic Society* **83**, 245-265, (2000)
- 1-41. March, J., John Wiley and Sons, New York 24, (2001)
- 1-42. Liu, H., *Ammonia synthesis catalyst 100 years: Practice, enlightenment and challenge*. 2014. p. 1619-1640.
- 1-43. Krylova, E.V., L.D. Kuznetsov and I.N. Konyukhova, *Kinet. Katal.* **5**, 948, (1964)
- 1-44. Ivanov, M.M., L.A. Rudnitskii, P.D. Rabina and L.D. Kuznetsov, *Kinet. Katal.* **9**, 1239, (1968)
- 1-45. Aika, K.-i., H. Hori and A. Ozaki, *Journal of Catalysis* **27**, 424-431, (1972)
- 1-46. Tokyo Institute of Technology: HP, http://www.titech.ac.jp/about/stories/ammonia_synthesis.html,
- 1-47. Kitano, M., Y. Inoue, H. Ishikawa, K. Yamagata, T. Nakao, T. Tada, S. Matsuishi, T. Yokoyama, M. Hara and H. Hosono, *Chemical Science*, (2016)
- 1-48. NIST chemistry webbook : National Institute of Standards and Technology,
- 1-49. Cross-ministerial Strategic Innovation Promotion Program: SIP, <http://www8.cao.go.jp/cstp/gaiyo/sip/>,
- 1-50. Aoki, T., H. Miyaoka, H. Inokawa, T. Ichikawa and Y. Kojima, *The Journal of Physical Chemistry C* **119**, 26296-26302, (2015)
- 1-51. Aoki, T., T. Ichikawa, H. Miyaoka and Y. Kojima, *The Journal of Physical Chemistry C* **118**, 18412-18416, (2014)
- 1-52. Hanada, N., S. Hino, T. Ichikawa, H. Suzuki, K. Takai and Y. Kojima, *Chemical*

- Communications **46**, 7775-7777, (2010)
- 1-53. Dong, B.X., T. Ichikawa, N. Hanada, S. Hino and Y. Kojima, Journal of Alloys and Compounds **509**, *Supplement 2*, S891-S894, (2011)
 - 1-54. Akiba, E. and H. Iba, Intermetallics **6**, 461-470, (1998)
 - 1-55. Wang, H.B., Q. Wang, C. Dong, L. Yuan, F. Xu and L.X. Sun, Journal of Physics: Conference Series **98**, 012018, (2008)
 - 1-56. Chen, P., Z. Xiong, J. Luo, J. Lin and K.L. Tan, Nature **420**, 302-304, (2002)
 - 1-57. Luo, W., Journal of Alloys and Compounds **381**, 284-287, (2004)
 - 1-58. Ichikawa, T., N. Hanada, S. Isobe, H. Leng and H. Fujii, Journal of alloys and compounds **404**, 435-438, (2005)
 - 1-59. Ichikawa, T., N. Hanada, S. Isobe, H. Leng and H. Fujii, The Journal of Physical Chemistry B **108**, 7887-7892, (2004)
 - 1-60. Isobe, S., T. Ichikawa, S. Hino and H. Fujii, The Journal of Physical Chemistry B **109**, 14855-14858, (2005)
 - 1-61. Hino, S., T. Ichikawa, N. Ogita, M. Udagawa and H. Fujii, Chemical Communications, 3038-3040, (2005)
 - 1-62. Leng, H.Y., T. Ichikawa, S. Hino, N. Hanada, S. Isobe and H. Fujii, Journal of Power Sources **156**, 166-170, (2006)
 - 1-63. Miyaoka, H., Y. Wang, S. Hino, S. Isobe, K. Tokoyoda, T. Ichikawa and Y. Kojima, Materials **8**, 3896, (2015)
 - 1-64. New Energy and Industrial Technology Development Organization: NEDO, http://www.nedo.go.jp/library/battery_hydrogen.html,
 - 1-65. Kojima, Y., K. Tange, S. Hino, S. Isobe, M. Tsubota, K. Nakamura, M. Nakatake, H. Miyaoka, H. Yamamoto and T. Ichikawa, Journal of Materials Research **24**, 2185-2190, (2009)
 - 1-66. Yamamoto, H., H. Miyaoka, S. Hino, H. Nakanishi, T. Ichikawa and Y. Kojima, International Journal of Hydrogen Energy **34**, 9760-9764, (2009)
 - 1-67. Fukai, Y., K. Tanaka and H. Uchida, Uchida Roukakuho Publishing CO., LTD., (2 nd ed. 2002)
 - 1-68. Schlapbach, L., 63, (1988)

2 Purpose

As described in Introduction, the various kinds of nitrides have attracted much attention and have been actively studied as functional materials. However, fundamental researches on syntheses and utilization are still necessary for further development in this field. In this thesis, I have focused on the following two research subjects related to the nitrides.

I. Nitrogen dissociation via reaction with lithium alloys

For the direct and effective syntheses of nitrides from N_2 gas, an extreme condition such as more than 800 °C and/or nitrogen plasma are necessary to dissociate N_2 molecule into N atoms as described in Introduction. This should be caused by very strong triple bond ($N\equiv N$) of N_2 gas with 945 kJ mol⁻¹ of the bonding energy. Consequently, catalysts to effectively dissociate N_2 molecule and utilization of atomic N including materials such as ammonia (NH_3) as nitrogen source are studied to establish the effective nitride synthesis processes so far. Here, lithium (Li) metal can easily react with N_2 to form lithium nitride (Li_3N) at a low temperature range of 50–400 °C, suggesting that the metallic Li possesses high reactivity to dissociate N_2 . However, Li_3N is thermodynamically stable and difficult to be used as the nitrogen sources. In order to control the dissociation of N_2 and to utilize the N atoms under moderate conditions, reactions using Li alloys are proposed. It is expected that Li in the alloys takes metal state, suggesting that the N_2 dissociation is available.

In this thesis, I have focused on the reaction using Li alloys as the reversible N_2 dissociation and recombination processes, where there is no reports for research on the Li alloys with such concept so far. The N_2 absorption and desorption, which are corresponding to dissociation and recombination, respectively, properties of the Li alloys are systematically investigated as fundamental research. Furthermore, the ammonia synthesis by N atoms dissociated by the Li alloys are performed, and the feasibility as the pseudo catalytic process are discussed.

II. Thermal decomposition of sodium amide (NaNH_2)

Hydrogen storage system using alkali(-earth) metal amide is one of applications by using the nitrides, and various kinds of systems are reported so far. However, there are few reports about the system consisted of sodium nitride (NaNH_2) at present. This may be caused by the difficult handling and complicated reaction process. Recently, it was reported that NaNH_2 showed catalytic properties for NH_3 decomposition ²⁻¹⁾, where the activities of NaNH_2 should be better than typical catalysts such as ruthenium (Ru) ²⁻²⁻⁴⁾. On the other report, NaNH_2 showed positive effects on the initial hydrogenation of magnesium (Mg) ²⁻⁵⁾. Therefore, NaNH_2 is very interesting and potential material for application in many kinds of fields. However, its decomposition process has not been understood yet.

In this thesis, to develop NaNH_2 as the functional and practical material, the detailed decomposition properties of NaNH_2 were investigated. The thermal decomposition of NaNH_2 is carried out under different thermodynamic conditions, and then the products are characterized by various types of analyses. From the obtained experimental results, the decomposition process of NaNH_2 is discussed.

Reference

- 2-1. David, W.I.F., J.W. Makepeace, S.K. Callear, H.M.A. Hunter, J.D. Taylor, T.J. Wood and M.O. Jones, *Journal of the American Chemical Society* **136**, (2014)
- 2-2. Aika, K.-i., H. Hori and A. Ozaki, *Journal of Catalysis* **27**, 424-431, (1972)
- 2-3. Kitano, M., S. Kanbara, Y. Inoue, N. Kuganathan, P.V. Sushko, T. Yokoyama, M. Hara and H. Hosono, *Nat Commun* **6**, (2014)
- 2-4. Kitano, M., Y. Inoue, H. Ishikawa, K. Yamagata, T. Nakao, T. Tada, S. Matsuishi, T. Yokoyama, M. Hara and H. Hosono, *Chemical Science*, (2016)
- 2-5. Chu, H., S. Qiu, L. Sun and J. Huot, *Dalton Transactions* **44**, 16694-16697, (2015)

3 Experimental procedure

3-1 Sample preparation

3-1-1 Materials

In this thesis, all of the starting materials are shown in Table 3-1-1. All the samples were treated in a glovebox (Miwa MFG, MP-P60W) filled with a purified Ar (> 99.9999 %) to prevent as oxidation and pollution due to water.

Table 3-1-1 Materials information

Material	Purity	Company
Lithium (Li)	99≥ %	Sigma Aldrich
Carbon (C)	99.999 %	Strem Chemicals
Silicon (Si)	99.999 %	Kojundo Chemical Lab.
Germanium (Ge)	99.999 %	Sigma Aldrich
Tin (Sn)	99.99 %	Kojundo Chemical Lab.
Lithium nitride (Li ₃ N)	99.5≥ %	Sigma Aldrich
Sodium hydride (NaH)	95 %	Sigma Aldrich
Sodium hydroxide (NaOH)	95 %	Sigma Aldrich

3-1-2 Mechanical ball-milling method

With applying to mechanical ball-milling process for the samples, local high pressure condition can be generated and make it possible to give physical energy for the samples by collision between balls and the inner wall of milling container. Thus, mechanical milling technique is used for various situations such as synthesis of alloys (mechanical alloying), mecanochemical reaction, synthesis of composite with close contact between components, dispersion of catalyst, formation of small particles, induction of defects, and so on. Figure 3-1-1 shows the schematic image of the rotating (planetary) ball-milling apparatus (Fritsch, P7). The milling container is made of Cr steel (UMETOKU Co. Ltd., SKD-11) with the inner volume of about 30 cm³, where a quick connector (Swagelok: SS-QC4-D-2PM) is equipped to the container to exchange the inner atmosphere. In this thesis, the ball-milling condition for synthesis of samples was fixed by following procedure,

1. 300 mg of sample and 20 steel balls (SUI-2) with 7 mm in diameter are introduced into the milling container, and then those are sealed by an O-ring stuck between an inner cover and the upper part of the milling container. In the case of graphite based sample, zirconia (ZrO₂) balls with 8 mm in diameter are used because graphite reacts with Fe which is the main component of steel ball to form a compound of graphite and iron.
2. The ball-milling is performed by repeating a set of 1 h milling and 30 min rest to avoid overheating, where a rotation rate is fixed at 370 rpm.

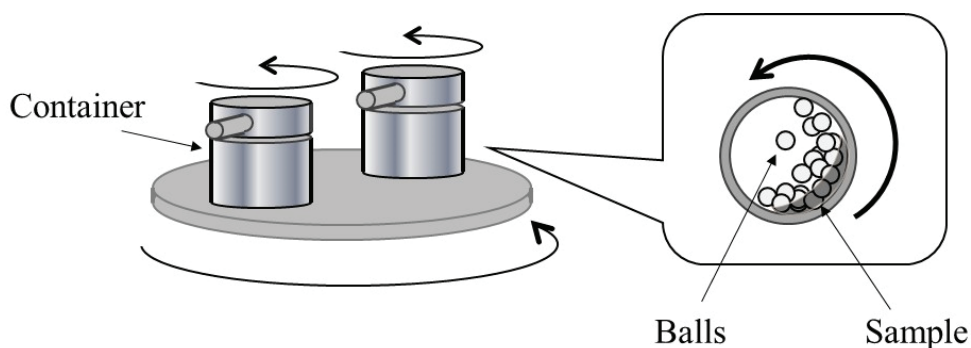


Figure 3-1-1 Schematic image of planetary ball-milling apparatus.

3-1-3 Synthesis of samples

Preparation of Li-M alloys

To synthesize $\text{Li}_{22}\text{Si}_5$, $\text{Li}_{22}\text{Ge}_5$, and $\text{Li}_{22}\text{Sn}_5$, Li metal was mixed with M (Si, Ge, or Sn) with molar ratio of 22 : 5 (4.4 : 1). And then, a mechanical alloying by using a ball-mill apparatus was performed for the mixtures for 2 or 3 h with 370 rpm rotation rate. The total 300 mg amount of mixtures was put into a 30 cm³ of milling vessel with 20 steel balls, and the milling vessel was filled with 0.1 MPa of Ar. After the milling, each sample of the Li-Si and Li-Ge was annealed for 1 h at 500 °C under 0.1 MPa of Ar and dynamic vacuum to induce a crystallization of those samples. Lithium intercalated graphite LiC_{12} was prepared by hand-milling for Li granules and graphite powders with 1:12 molar ratio for 40 min on an agate mortar. After that, the obtained mixture was annealed at 500 °C under 0.1 MPa of Ar. The mixtures of Li_3N and M were prepared to investigate the nitrogen desorption properties. The molar ratio of Li_3N and M was chosen to be 22 : 15 (4.4 : 3) for the Si, Ge, or Sn system, and to be 1 : 18 for the C system. The ball-milling was carried out for 2 h under 0.1 MPa of Ar by 370 rpm of rotation rate. Here, the 20 steel balls were used for the Si, Ge, or Sn system, and 20 zirconia balls were used for the C system.

Preparation of NaNH_2

NaNH_2 was synthesized by a reaction between NaH and liquid NH_3 at room temperature. As a reference to characterize reaction products, Na_2O was synthesized by heat treatment of NaOH and NaH mixture at 300 °C under a dynamic vacuum condition³⁻¹⁾, where the mixture was prepared by ball-milling under 1 MPa of H_2 for 2 h to make close contact between two solid powders.

3-2 Experimental techniques

3-2-1 Powder X-ray diffraction (XRD)

Principle

Powder samples are analyzed by X-ray diffraction (XRD) measurements to know structural properties such as crystal structure, lattice constants, and atomic positions. For the XRD measurements, “Characteristic X-ray” is used. The electron energy in atoms

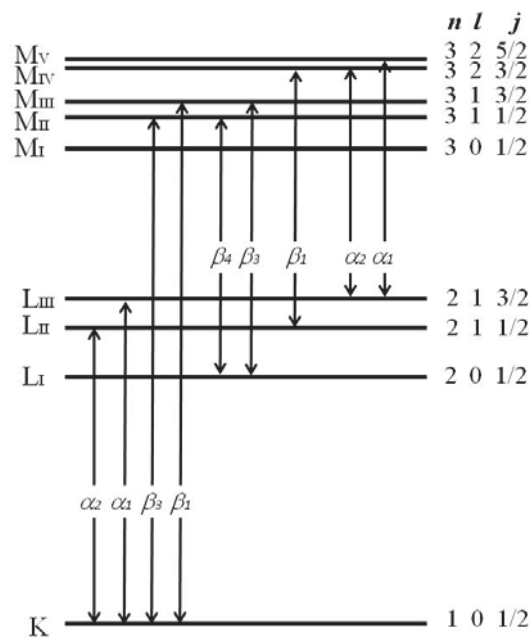


Figure 3-2-1 Relationship diagram between energy levels of electron shells and characteristic X-rays ³⁻²⁾

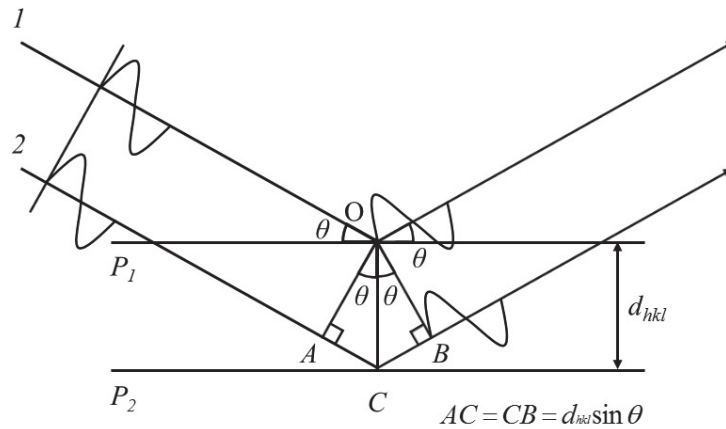


Figure 3-2-2 Inferences of scattered wave from lattice plane ³⁻³⁾

is quantized and generally classified into K, L, and M shells as shown in Figure 3-2-1³⁻
²⁾. When electrically accelerated thermoelectrons are irradiated into target materials to generate the characteristic X-ray, an electron in inner energy level such as the K shell is ejected, where thermoelectrons are electrically accelerated by high voltage between a filament and target materials as cathode. Then, an electron in outer-shells fall into the vacant position to make stable ground state with emitting X-ray. The emitted photon during this process has specific wavelength depending on the energy difference between the inner-shell and outer-shell, where the generated photon is called characteristic X-ray. It is required to choose suitable target materials by considering the sample composition. Typically, characteristic X-ray of K_{α} emitted by Cr, Fe, Co, Cu, and Mo are utilized for X-ray structural analysis.

Assuming that two lattice plane P1 and P2 with the distance of d_{hkl} , in which hkl are miller indexes³⁻³⁾, irradiated monochromatic X-ray of wavelength λ at an incidence angle θ is scattered by electrons in each atom, which are represented as wave1 and wave2 in Figure 3-2-2. When the optical path difference is integral multiple n , the diffracted X-rays are coherent with each other thus undergoes through constructive interference. This phenomena is expressed as following equation,

$$n\lambda = 2d_{hkl} \sin \theta . \quad (3-1)$$

This diffraction condition is well known as Bragg's law. By scanning the intensity of diffracted X-rays with the angle of 2θ between incident X-ray and diffracted one, XRD patterns are obtained.

Procedure

In this work, the XRD measurements were carried out for all of powder and bulk samples to identify the phases by using X-ray diffractometer (RINT 2000, Rigaku). The X-ray source is Cu-K α ($\lambda=1.54 \text{ \AA}$) with the output energy of $\sim 8 \text{ kW}$ (40 kV, 200mA). The sample was spread on a glass plate and adhered by using a grease (Apiezon® Grease, M&I Material Ltd.). And then, the sample was covered with a polyimide sheet (8 μm thickness, Kapton®, Du Pont-Toray Co., Ltd.) and sealed around the sample with the Apiezon grease to avoid oxidation during the measurements. All the processes of the

above sample preparation were performed in the glovebox. The obtained XRD patterns were analyzed by a software PDXL with powder diffraction files (PDF) as the database.

3-2-2 Thermogravimetry – Differential thermal analysis (TG-DTA)

Principle

The weight change during a reaction at elevated temperatures is continuously observed by the thermogravimetry (TG) using an accurate balance. Figure 3-2-3 shows a schematic image of the thermobalance system. An electric current is supplied to a coil to keep equilibrium position of the sample pan when the position detector detects the displacement, which corresponds to the weight change of the sample. And then, the amount of the applied current is recorded as a signal. For the differential thermal analysis (DTA) measurements, a heat flow with an exothermic or endothermic reaction can be observed under programed heating and/or cooling process, besides the phase transitions of the samples such as melting can also be detected. The DTA system is shown in Figure 3-2-4³⁻⁴). Two pans are placed in the furnace, one of which is used as a reference pan while another carries sample. With an increasing temperature, the temperature difference (ΔT) is observed by thermocouple equipped with each holder. For the apparatus used in this work, the gases desorbed from samples are flowed by the carrier gas of Ar. Therefore, the partial pressure of desorbed gases is removed from the reaction fields of the TG-DTA measurement, enabling the reactions to be proceeded in open system without partial pressure of the desorbed gases. Parts of generated gases are flowed to mass spectrometer through the capillary, which is connected with the TG-DTA apparatus.

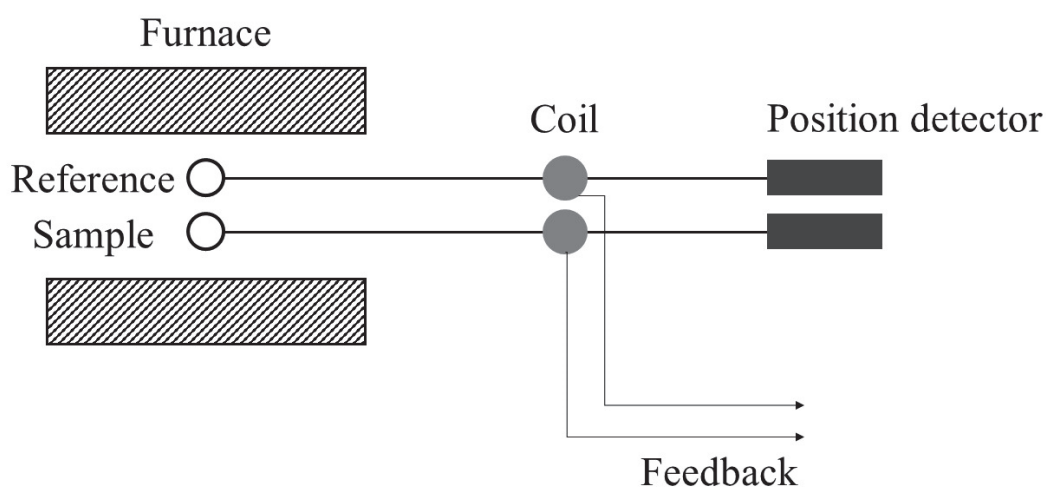


Figure 3-2-3 Schematic images of thermobalance system

Procedure

The thermal properties of the samples were investigated by the TG-DTA apparatus (Rigaku, TG8210), which is set inside the glovebox to prevent an influence of air. The alumina (Al_2O_3) sample pans were used because of its thermal stability up to 900 °C. Here, it is required to be carefully chosen materials of pans to avoid the side reaction (corrosion) between samples and sample pans. The heating rate was fixed to be 5 °C min⁻¹. Less than 10 mg of samples was put into the pan and set to the balance (holders) in the TG-DTA apparatus. The atmosphere for TG measurement is changeable such as an inert gas of Ar and He, and/or air, N₂, O₂, and H₂.

3-2-3 Differential scanning calorimetry (DSC)

Principle

An enthalpy change with exothermic and endothermic reactions such as phase transitions and chemical reactions are measured by the differential scanning calorimetry (DSC) systems, which can evaluate heat flow more accurately than the above DTA measurements. The DTA can observe the temperature difference between the sample and the reference at the programmed temperature as described above. For the DSC measurement, the temperature difference can be observed as the same way as DTA, however the DSC can especially detect the heat quantity of the corresponding reaction more sensitively than the DTA. Furthermore, larger amounts of the sample can be measured compared with the DTA, leading to clear signals. The integrated area of peaks observed in the DSC measurements theoretically corresponds to the reaction heat. There are two types of DSC systems. One is a power-compensation type, and the other is heat-flux type which is used in this study.

The heat transfer due to the thermal reaction of samples, which is called heat flux dq_s/dt , per unit of time is expressed by “Newton’s law of cooling” as following equation,

$$\frac{dq_s}{dt} = \frac{1}{R} (T_f - T_s), \quad (3-2)$$

where T_f is temperature of the furnace and T_s is that of reference. The heat flux is given by the multiplication of the temperature difference $T_f - T_s$ and the inverse of thermal resistance R . The thermal resistance is usually given as an apparatus constant depending on the furnace and cell, which is given by the inverse of heat conduction coefficient. As the same procedure, dq_r/dt for the reference is expressed as follows,

$$\frac{dq_r}{dt} = \frac{1}{R} (T_f - T_r), \quad (3-3)$$

where T_r is the temperature of reference. Here, following equation is given by subtracting eq. (3-2) from eq. (3-3) as follows,

$$\frac{dq_s}{dt} - \frac{dq_r}{dt} = -\frac{1}{R} (T_s - T_r), \quad (3-4)$$

$$\therefore \frac{d\Delta q}{dt} = -\frac{1}{R} \Delta T. \quad (3-5)$$

ΔT as a function of time is measured by a thermocouple as shown in Figure 3-2-4.

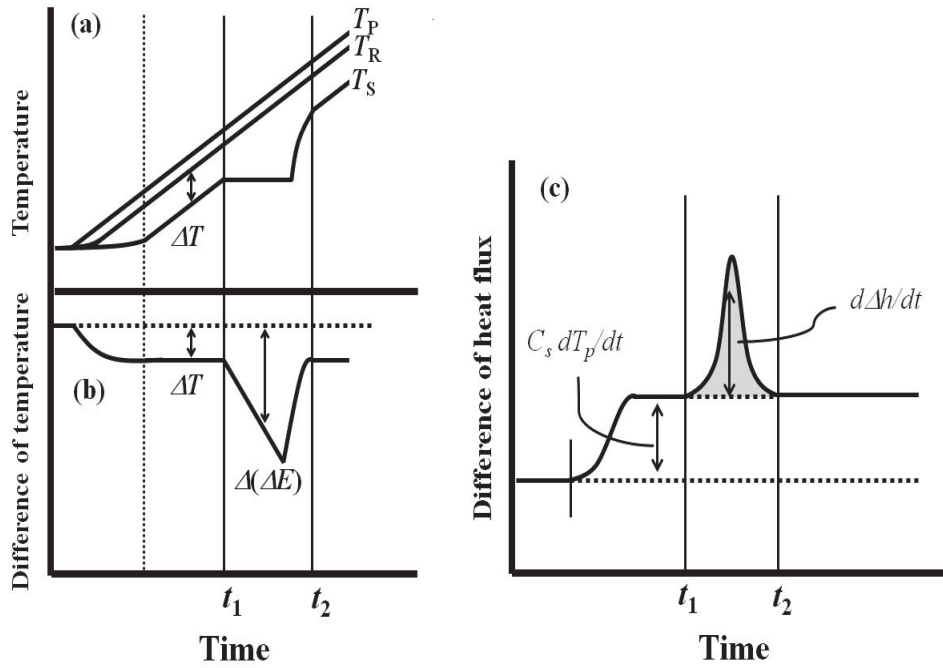


Figure 3-2-4 Time variation of temperature of furnace T_P , reference cell T_R , and sample cell T_S (a), time variation of temperature difference between reference cell and sample cell ΔT (b), and time variation of difference of heat flux between reference cell and sample cell ($d\Delta q/dt$) (c)

Procedure

The differential scanning calorimetry (DSC) (TA Instruments, Q10 PDSC) is placed into the glovebox. The reaction properties of samples were investigated under various kinds of atmosphere such as Ar, H₂, and N₂. To investigate the reaction properties of Li alloys, N₂ and H₂ gases were used for the nitrogenation and ammonia synthesis reaction, respectively. The nitrogenation of the Li alloys were performed in a batch reactor filled with 0.1 and 3 MPa of N₂ up to 500 °C with the heating rate of 5 °C min⁻¹. The ammonia generation experiments were carried out up to 300 °C with the heating rate of

5 °C min⁻¹ under 0.5 MPa of H₂ with flow rate of 50 cm³ min⁻¹. The hydrogenation reaction of “Na₂NH” was measured as well. The reactor was filled with H₂ at the pressure of 0.1 MPa and was heated up to 400 °C with heating rate of 5 °C min⁻¹. The sample pan made from aluminum (Al) is used for all of the DSC measurements.

3-2-4 Thermal desorption mass spectroscopy (TDMS)

Principle

In this work, thermal gas desorption properties are investigated by the thermal desorption mass spectroscopy (TDMS) connected to the TG-DTA and DSC apparatuses. TDMS is consisted of three parts, which are an ionization source, quadruple mass spectrometer, and a detector. In analyses parts, an ultra-high vacuum condition is kept to realize high sensitivity by using a turbomolecular pump (TMP). Firstly, in the ionization part, electrically accelerated thermoelectrons collide with gaseous molecules desorbed from samples to make ionized states. Then, the ionized molecules of the desorbed gases are separated in accordance with a mass-to-charge ratio ($=m/z$), where m is mass and z is charge number of the molecules, in the quadruple mass spectrometer. Here, fragment ions are generated by splitting the ionized molecules in case of having excess internal energy. Ionized molecules are separated depending on these mass deference in the quadruple mass spectrometer by the following way.

A schematic image of quadruple mass spectrometer is shown in Figure 3-2-5³⁻⁵⁾. Couple of twin electrodes are located in a square shape with supplied voltage V_m as expressed following equation,

$$V_m = U + V \cos \omega t . \quad (3-6)$$

U is direct current (D.C.) voltage, V is maximum alternating voltage (A.C.), and ω is equal to $2 \pi \nu$. In the quadrupole area, ionized gaseous molecules are distinguished by varying U and V values with keeping U/V value constant. Then, the ions with the specific value of m/z can pass through the electrodes and reach the detector part, although the other ions with different m/z ratio from the above one collide with electrodes because it is getting high amplitude. This process is expressed as following equation,

$$\frac{m}{z} = \frac{1}{7.22} \frac{V}{r_0^2 \cdot f^2} , \quad (3-7)$$

$$f = \frac{\omega}{2\pi} , \quad (3-8)$$

where r_0 is the incircle radius of quadruple electrodes (Figure 3-2-6) and f is a voltage frequency. The ions which passed through the electrodes are eventually detected by the

detector.

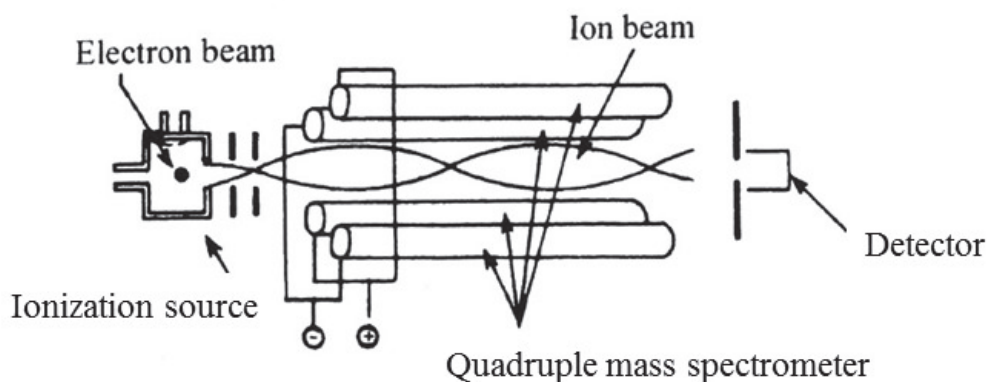


Figure 3-2-5 Schematic image of the TDMS apparatus ³⁻⁵⁾

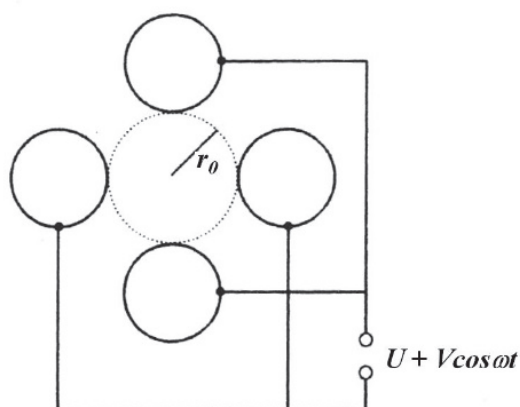


Figure 3-2-6 Schematic image of the quadrupole mass spectrometer ³⁻⁵⁾

Procedure

Thermal gas desorption properties of samples were analyzed by the TDMS apparatus (Anelva, M-QA200TS) connected to the TG-DTA and DSC apparatuses, which are placed in the gloveboxes. For the TG-DTA-MS measurement, desorbed gases were analyzed under Ar gas flow condition. On the other hands, for the DSC measurement, a carrier gas was chosen depend on the reaction condition such as H₂, N₂, and Ar. The heating rate for both measurements were fixed to be 5 °C min⁻¹.

3-2-5 Fourier transform infrared (FT-IR) spectroscopy

Principle

Molecules vibrate consistently with keeping their chemical bonds. When the equivalent energy with the molecular vibration is irradiated to the sample, the molecule absorbs a photon with specific frequencies and the molecule has an excited state. Infrared is often used to characterize the chemical bonding because the energy region of infrared is suitable for molecule vibration. Polyatomic molecules have certain vibration frequencies, and normal vibration modes are determined by $(3N-6)$ for a non-linear molecule and $(3N-5)$ for a linear molecule. For example, H_2O molecule consists of three atoms $N=3$ and has three normal vibration modes as shown Figure 3-2-7 (a) ³⁻⁶. The ν_1 is called OH symmetric stretching vibration, the ν_2 is HOH bending vibration, and the ν_3 is OH asymmetric stretching vibration. A variation of electric dipole moment makes infrared absorption and, in the case of H_2O , stretching and bending vibration modes are

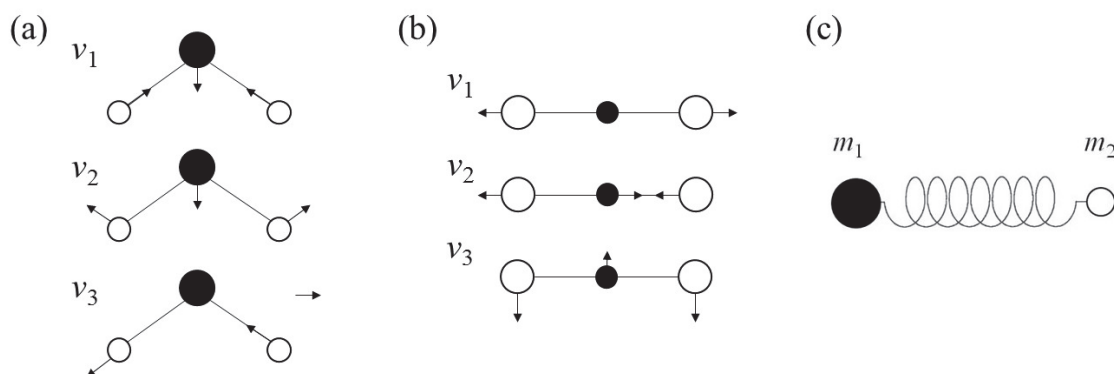


Figure 3-2-7 Vibration modes for (a) H_2O and (b) CO_2 molecule, and (c) Hooke's Law

infrared active. In the case of CO_2 shown in Figure 3-2-7 (b), the electric dipole moment is not changed by the symmetric vibration of ν_1 , resulting in the infrared inactive. However, for the ν_2 and ν_3 , variation of electric dipole moment occurs, suggesting that these are the infrared active ones.

A vibration between two atoms is expressed by Hooke's Law as following equation (Figure 3-2-7 (c)),

$$\nu = \frac{1}{2\pi} \sqrt{\frac{k}{\mu}}, \quad (3-9)$$

where k is spring constant and μ is reduced mass shown as follow,

$$\mu = \frac{m_1 m_2}{m_1 + m_2}, \quad (3-10)$$

where m_1 and m_2 are mass of composed atoms. It is obvious that stretching vibration is depending on close relationship with a mass of bonded atoms. Thus, isotope effect is especially larger for hydrogen (H) including molecules because the mass of deuterium (^2D) is twice as that of the protium (^1H).

Schematic view of FT-IR is shown in Figure 3-2-8. The IR spectra are measured by “Michelson interferometer”. The light with continuous energy in the infrared area is passed through a sample enter the interferometer, and then the intensity of $I(x)$ is detected as a function of optical path difference of x . The positional information is converted into energy information by using “Fourier transform” process, and the infrared absorption spectra as a function of energy are obtained.

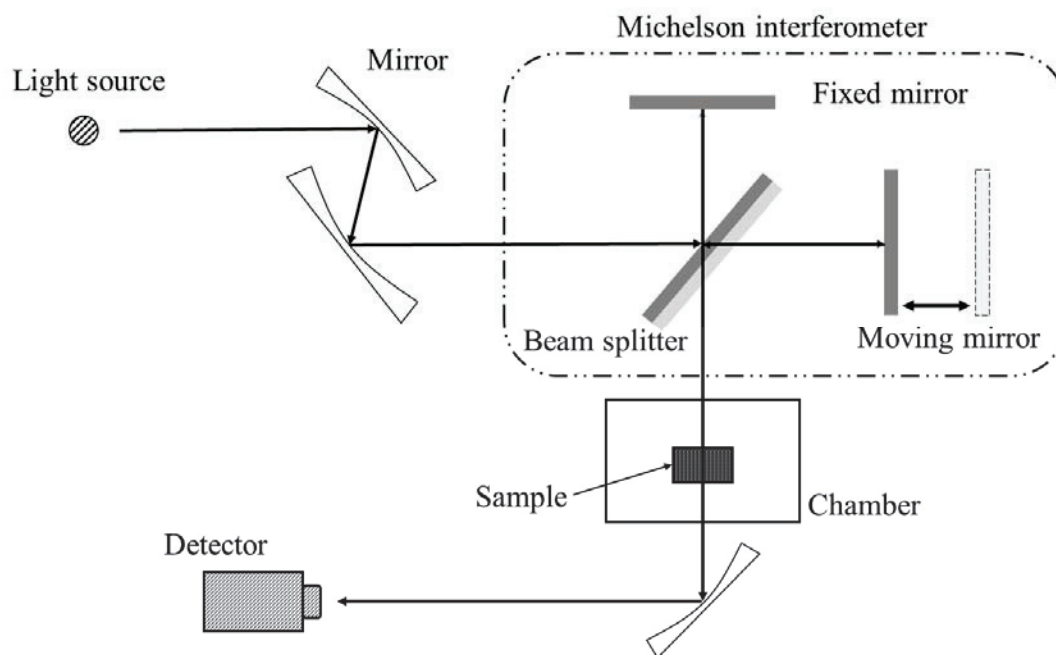


Figure 3-2-8 Schematic view of FT-IR

Procedure

The Fourier transform infrared (FT-IR) measurement (Spectrum One, Perkin-

Elmer) was performed to examine IR active vibration modes of samples. A diffuse reflection cell was employed and all the samples were diluted by potassium bromide KBr at the ratio of the sample to KBr was 5 mass%. The samples for measurements were prepared and sealed in a cell inside the glovebox to avoid oxidation and hydroxylation of samples.

3-2-6 Raman spectroscopy

Principle

By the Raman spectroscopy, chemical structures can be characterized like the IR spectroscopy. When the material is irradiated by the incident beam, scattering beam is generated after the interaction between the material and incident beam. The scattering beam is categorized into elastic scattering (Rayleigh scattering) and inelastic scattering (Raman scattering). Because the intensity of the Raman scattering is about 10^{-6} times weaker than that of Rayleigh scattering, monochromatic laser is generally used as excitation light source. In the Raman scattering, the band with the lower frequency than incident beam is called Stokes scattering ($\nu_0 - \nu$), on the other hand, with the higher frequency is called anti-Stokes scattering ($\nu_0 + \nu$). Typically, Stokes scattering is used to discuss the chemical state of the samples for the Raman spectroscopy. The difference between Raman and Infrared spectroscopy, where both analyses can characterize the molecule structure by detecting the vibration modes of materials, is follows (Figure 3-2-9). For the Raman spectroscopy, shifted Raman scattering is detected according to the change of polarizability. On the other hand, for Infrared spectroscopy, variation of the dipole moment is detected as Infrared absorption spectrum.

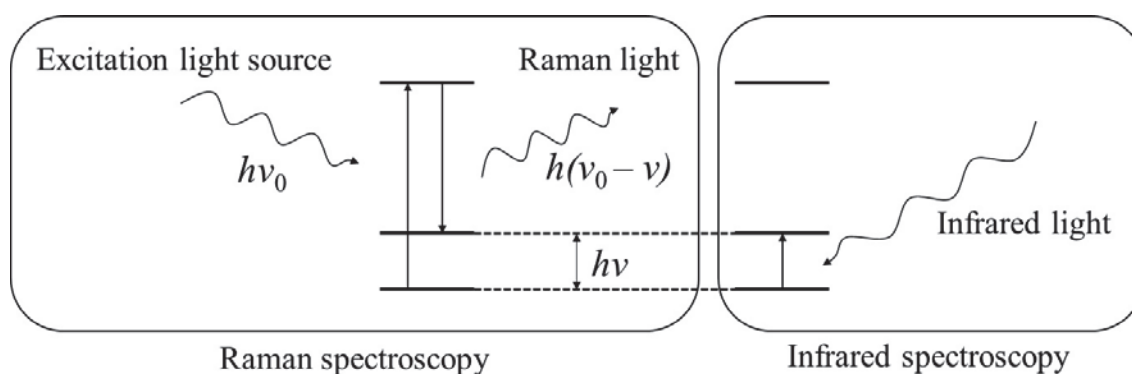


Figure 3-2-9 Vibration energy potential

Procedure

Raman spectra were obtained by using the Raman scattering apparatus (DXR Smart Raman, ThermoFisher SCIENTIFIC). The wave length of 780 nm was used as

laser source. The samples were packed in a vial container (4 ml), which was covered by Teflon tape cap to prevent the reaction with oxide and water vapor, and were prepared in the glovebox filled with high purity Ar.

3-2-7 Transmission Electron Microscope (TEM)

Principle

Transmission electron microscope (TEM) is an important method to characterize materials in micro or nano meter. The detailed information about microstructure, crystal structure, and chemical composition can be obtained. When an accelerated electron is radiated to solid samples, secondary electron and electromagnetic ray are generated according to several internal interactions. An incident electron can penetrate through the sample without any interaction (transmission electron) when the sample is thin or small. Some of electrons are scattered without losing the energy (elastic scattering) and with the partial energy loss (inelastic scattering). Assuming that parallel electron beam enter a single crystal sample or parts, some of electrons penetrate straight through the samples (transmitted wave) and the others are diffracted (diffracted wave) at the angle of $2\theta_B$ (θ_B : Bragg angle). Both the waves are focused at a back focal plane placed back of an objective lens, and then be focused at an imaging plane. Here, an electron diffraction pattern can be obtained when a film is set at the point of back focal plane, and an electron microscopic image, which is enlarged image of sample, is also obtained when a film is set at the point

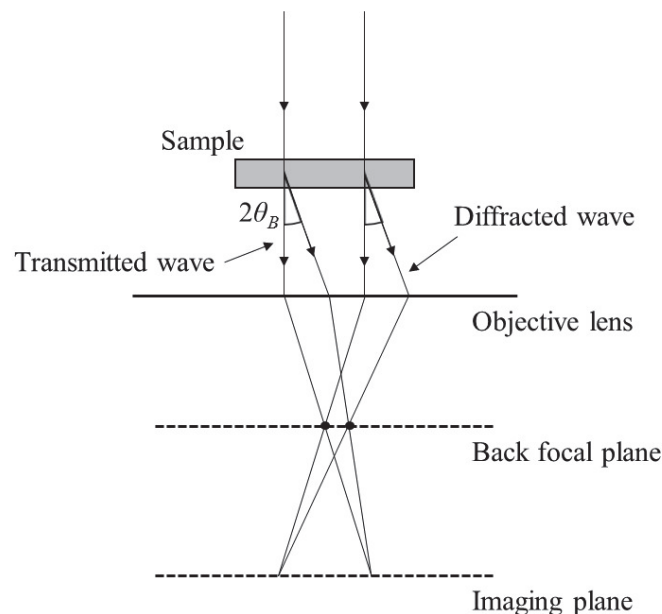


Figure 3-2-10 Interaction between transmitted wave and diffracted wave

of imaging plane (Figure 3-2-10). When the diffracted wave reaches the film without being reflected by lenses, diffraction spots are projected on the film. The distance r_{hkl}

between the diffraction spots caused by transmitted wave is expressed as following equation (Figure 3-2-11 ³⁻⁷⁾),

$$r_{hkl} d_{hkl} = \lambda L, \quad (3-11)$$

where d_{hkl} is lattice spacing of lattice plane hkl , λ is wavelength of electron beam, and L is called camera length, which is the distance from the sample to the film.

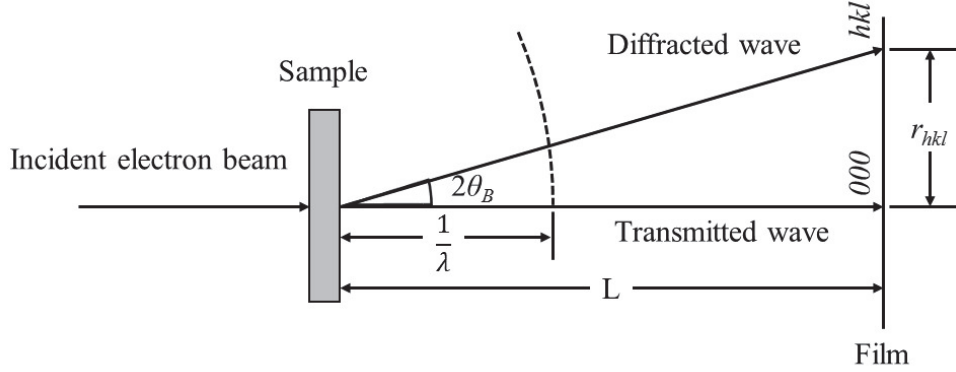


Figure 3-2-11 Relationship of diffraction spot, direct spot, and camera length ³⁻⁷⁾

Procedure

In this study, TEM (JEOL, JEM-2010) was used to investigate the microstructure of samples. Figure 3-2-12 shows the schematic image and picture of a plastic bag method ³⁻⁸⁾. The samples were dispersed on the Mo grid and the grid is loaded into the TEM holder in the glovebox. The TEM holder was sealed into the main body of the plastic bag by using a clip with high purity of Ar gas. Therefore, it is possible to transfer the sample to the TEM apparatus without an oxidation. Then, the joint part of plastic bag was connected with TEM by a binding tape. At the jointed section, the air is replaced with Ar gas by continuous flushing Ar gas for 3-5 min.

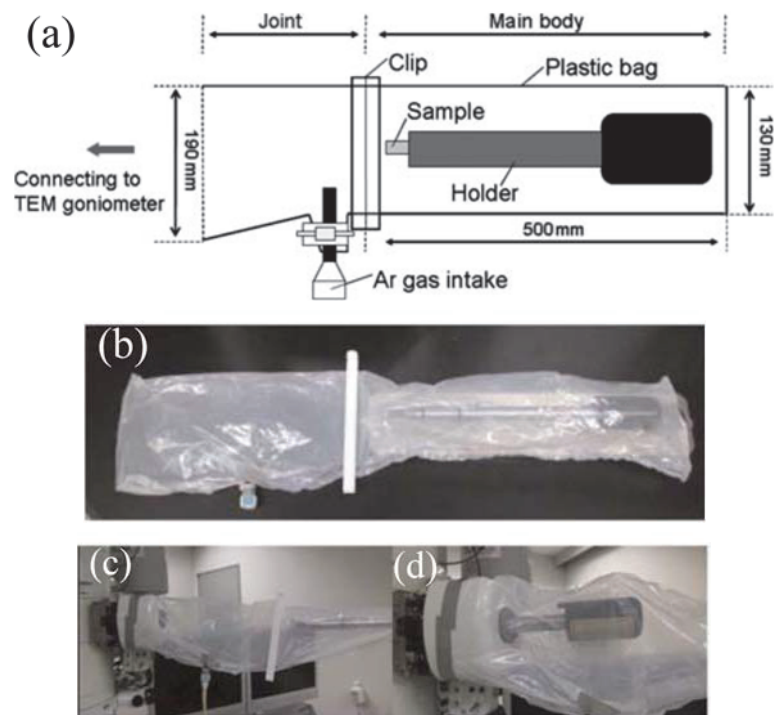


Figure 3-2-12 (a)Schematic image of plastic bag method, (b)TEM holder is covered with plastic bag, (c)Plastic bag is connected to the TEM, (d)TEM holder is inserted

3-2-8 Scanning Electron Microscope (SEM)

Principle

Scanning electron microscope (SEM) is typically employed not only for observing a morphology of the samples but also for quantitative analyses of composition including elements in the samples.

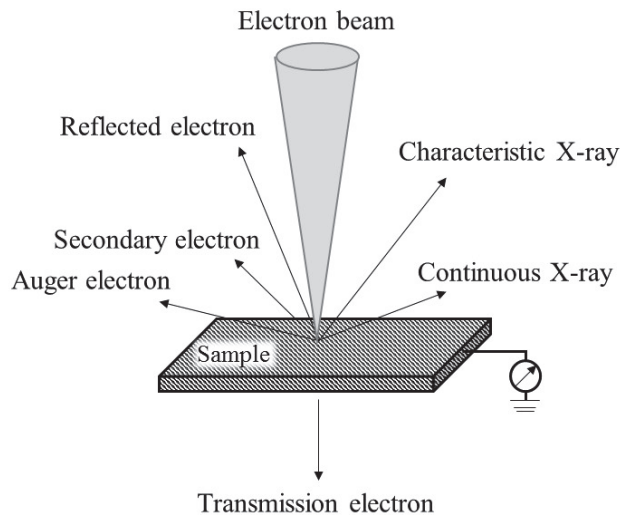


Figure 3-2-13 Available information by interaction between incident beam and material

SEM image is obtained by scanning incident beam toward two dimensions on a sample. The electron beam is generated by choosing an electron gun, where two kinds of electron gun are commonly used at present. One is thermoelectron, which is widely utilized and is featured by its large probe current and good cost performance. The other is Field Emission (FE) type. The High-intensity electron is irradiated from the sharp-edged tip, where the electron is emitted by tunnel effect. The high-resolution observation can be available for the use of FE type than thermoelectron type. When the electron beam is irradiated to the sample, various kinds of interaction occurs as shown in Figure 3-2-13. Especially, the secondary electron and the reflected electron are commonly used in the SEM measurement. In general, a contrast image of secondary electron is affected by the surface composition and gradient of sample particles. The intensity of secondary electron is very low less than ~ 100 eV, resulting surface sensitive due to low detection depth. On the other hand, reflection electron image can be obtained according to backscattered

electron, which direction is against the incident electron. The scattering intensity strongly depends on the electrostatic potential of an atom, in other words, the larger atomic number atoms should show a bright contrast. Furthermore, the energy of reflected beam is proportional to that of incident beam. It is required to be noted that the untypical contrast due to the charge, which is generally called “charge-up”, is observed when it comes to a sample with low conductivity. The common ways to solve this problem, samples of thin film and/or of covered with high conductivity mesh are used. Furthermore, as a technique of measurement, low-vacuum observation (~ 1000 Pa) is utilized although the pressure range for $10^{-3} \sim 10^{-4}$ Pa is applied to typical observation.

Procedure

In this study, SEM (JEOL, JIB-4600F/HKD) was used to observe the morphology and to characterize chemical composition of the samples. In the case of LiM alloys (M=Si, Ge, Sn), bright contrast might be obtained because the atomic number of Li is 7, which is less than Si, Ge, and Sn with the atomic number of 14, 32, and 50, respectively. The sample was spread on the sample holder and then it was enclosed in the transfer vessel to take them to SEM apparatus without exposure of the sample to the air. The acceleration voltage was fixed at 10 kV.

3-2-9 Energy Dispersive X-ray Spectroscopy (EDS)

Principle

Energy dispersive X-ray spectroscopy (EDS) was performed as elemental analysis. When an incident electron beam is irradiated to the samples, several kinds of electron and X-ray can be emitted. When an inner shell electron is ejected by incident electron beam (electron excitation), an outer shell electron goes to the inner shell with emitting characteristic X-ray (electron relaxation) (Figure 3-2-14³⁻⁹⁾). The energy of characteristic X-ray depends on elements, suggesting that the elements in the samples can be qualitatively and quantitatively analyzed by detecting the characteristic X-ray. For the quantitative analysis, the relative atomic ratio of the including elements can be simply estimated from the peak area of each characteristic X-ray.

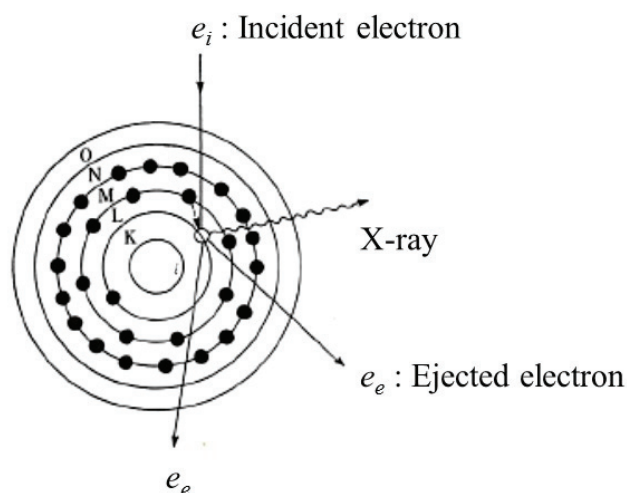


Figure 3-2-14 Principle for X-ray generation³⁻⁹⁾

Procedure

The elemental analysis of the LiM alloys (M=C, Si, Ge, Sn) was performed by EDS (JEOL, JEM-2010), which is combined with TEM, at Hokkaido University. The sample was fixed on the grid made of molybdenum (Mo) and this grid is set on the Copper (Cu) holder in the glovebox. The rod, on which the holder is fixed, is covered by a plastic sheet to transfer it to TEM apparatus without an oxidation of the sample, and then the holder was installed in TEM apparatus.

3-2-10 Gas chromatography (GC)

Principle

Gas chromatography can characterize gaseous products. Some kinds of column can be selected depending on the products, leading to the high sensitivity. Generally, inert gases are used as a carrier gas such as helium (He), nitrogen (N₂), and argon (Ar). The input samples are carried into column part and separated by interacting the filler. Thermal conductivity detector (TCD) is utilized in this experiments. In this detector, sample gases are electrically detected by using the difference of thermal conductivity depended on carrier gases. When the difference of thermal conductivity between a carrier gas and a sample gas is larger, the higher sensitivity can be obtained. Then, the suitable carrier gas should be chosen depending on the sample gas. The thermal conductivity of typical gases are shown in Table 3-2-1.

Table 3-2-1 Thermal conductivity for each gaseous species

Gaseous species	Thermal conductivity (0 °C) mW/m·K
Helium (He)	141.5
Hydrogen (H ₂)	168.4
Nitrogen (N ₂)	24.2
Argon (Ar)	1.5
Oxygen (O ₂)	24.3
Carbon dioxide (CO ₂)	16.6
Methane (CH ₄)	30.1
Ethane (C ₂ H ₆)	18.0
Ammonia (NH ₃)	2.2

Procedure

The reaction products obtained after the thermal decomposition of NaNH₂ were studied by GC (GC-14B, Shimadzu). Ar was used as carrier gas at the pressure of 120 kPa, and the column was set at the temperature of 100 °C. The other parts; injection, TCD detector, and detector (batch), were set at 120 °C. Two types of columns were used. One

is Shincarbon ST, which shows the strong interaction to sample gas, in other words, it can clearly separate H_2 and N_2 . The other is Chromosorb (silica), which shows weak interaction to the sample gas, resulting in the separation of NH_3 and other gases.

Reference

- 3-1. Miyaoka, H., T. Ichikawa, N. Nakamura and Y. Kojima, International Journal of Hydrogen Energy **37**, 17709-17714, (2012)
- 3-2. Waseda, Y. and E. Matsubara, UHIDA ROKAKUHO PUBLISHING CO., LTD., (1998)
- 3-3. Asakura, K., Asakura Publishing Co, Ltd., (2002)
- 3-4. Akaiwa, H., S. Tsude, K. Tsunoda and H. Haraguchi, MARUZEN-YUSHODO Company, Limited, (1991)
- 3-5. Tanaka, S. and Y. Iida, SHOKABO Co., Ltd., (2000)
- 3-6. Hirokawa, T. and T. Tsuda, Asakura Publishing Co, Ltd., (2004)
- 3-7. Saka, H., UHIDA ROKAKUHO PUBLISHING CO., LTD., (1997)
- 3-8. Yao, H., S. Isobe, Y. Wang, N. Hashimoto and S. Ohnuki, Journal of Electron Microscopy **60**, 375-378, (2011)
- 3-9. Japan, T.S.S.S.o., MARUZEN-YUSHODO Company, Limited, (1999)

4 Results and discussions

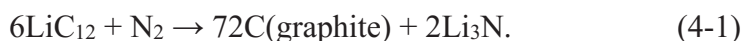
4-1 Nitrogenation of Li-M alloys

In order to investigate the N₂ dissociation and nitrogenation properties of the Li-M alloys, the single phase of the alloys were synthesized by ball-milling. The reactivity of the alloys with N₂ was investigated by heating up to 500 °C under the N₂ pressure.

4-1-1 LiC alloy

Li-C alloy was obtained by mechanical alloying. From the XRD pattern of the as-synthesized Li-C alloy in Figure 4-1-2, the formation of LiC₁₂ is observed. Figure 4-1-1 shows DSC profiles of LiC₁₂ under N₂ pressure of 0.1 and 3 MPa. A broad exothermic peak was observed in the temperature range from 300 to 400 °C at 0.1MPa, indicating that nitrogenation reaction gradually proceeded. A sharp endothermic peak appeared at around 450 °C at 0.1 and 3 MPa. This reaction should be corresponded to a structural phase transition of lithium carbide (Li₂C₂)⁴⁻¹⁾ because exothermic peak was observed as well at the same temperature range in cooling process. It can be suggested that Li₂C₂ phase is partially formed by the reaction of nano or amorphous carbons generated during the mechanical milling process. The diffraction peaks observed in the as-synthesized Li-C alloy was assigned to LiC₁₂ phase. After the reaction with N₂, the diffraction peaks were shifted toward the higher angle and assigned to graphite, where this is typical variation by a decrease in interlayer distance due to the deintercalation of Li from LiC₁₂.

Assuming the complete reaction of LiC₁₂ and N₂ with the formation of graphite and Li₃N, the reaction is expressed as follow,



The reaction yield for the generation of graphite and Li₃N was estimated from weight gain measured after the reaction by the nitrogenation to be 194 %. The reaction yield of excessed 100 % would be caused by the existence of high Li composition phase in the as-synthesized sample. In fact, the weak peak corresponding to LiC₆ is observed around 24 degree in Figure 4-1-2 as a shoulder-like structure with the main peak of LiC₁₂. Although the above results indicate that the Li atoms located in the layers of graphite reacted with

N₂ to form Li₃N and graphite, Li₃N was not observed in the XRD measurements. This results would be considered to following reasons. The amount of Li composed in the LiC₁₂ should be small because of the 1 : 12 composition for Li : C, and the generated Li₃N is expected to be possibly nano or amorphous states. Here, the results obtained by the reaction with 3 MPa of N₂ were similar to that obtained under 0.1 MPa. Namely, the kinetics for the nitrogenation reaction of Li-C alloy is not affected by the nitrogen pressure. To characterize and identify the nano-sized or amorphous products, TEM measurements and EDS analysis were carried out. Here, electron diffraction measurements were also performed, however the useful information to confirm the structure of Li₃N was not obtained. Figure 4-1-3 (a) shows TEM image of Li-C alloy after the nitrogenation. Any clear contrast to distinguish products from the starting material was not found. This results is caused by the low content of Li in LiC₁₂ and small difference in electron numbers of C and N. In other words, it should be difficult to distinguish the products from Li₃N and other products even if the nitrogenation reaction is proceeded. The EDS measurements were carried out at the some points in the particle. However, it was difficult to distinguish the products from alloys because energy of characteristic X-rays from C and N are very close.

4-1-2 Li-Si alloy

From the XRD pattern of the as-synthesized Li-Si alloy in Figure 4-1-5, the formation of Li₂₂Si₅ is observed. Figure 4-1-4 shows DSC profiles of the Li-Si alloy (Li₂₂Si₅) under N₂ pressure of 0.1 and 3 MPa. The clear exothermic peak was observed around 300 °C for the reaction of Li₂₂Si₅ with 0.1 MPa of N₂ as shown in Figure 4-1-4. Furthermore, gradual exothermic reaction proceeded from 450 °C. On the other hand, two clear exothermic peaks were observed from 200 °C under 3 MPa of N₂. The Li-Si alloys with lower Li composition such as Li₁₃Si₄ and Li₇Si₃ were observed after the DSC measurement under 0.1 MPa of N₂, and then small peak corresponding to Li₃N was found. Namely, Li₂₂Si₅ phase is changed to Li₁₃Si₄ and Li₃N is formed at 300 °C, and the generation of Li₇Si₃ starts from 450 °C, suggesting that Li₇Si₃ is final product at 500 °C. Here, the generation of Li₁₃Si₄, above reactions can be proceeded at lower temperatures

below 450 °C under 0.1MPa of N₂ pressure. Only Li₇Si₃ phase was observed in XRD pattern after the reaction at 500 °C under 3 MPa of N₂. This result also indicates that the nitrogenation is accelerated by the N₂ pressure and the Li₇Si₃ phase is the final product in this temperature range.

The weight gain due to the reaction with N₂ was almost consistent with the expected value from the eq. (4-2) and (4-3).

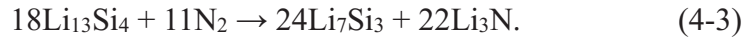


Figure 4-1-3 (b) shows TEM image of selected particle for Li-Si alloy after the nitrogenation. The TEM image shows low contrast parts around the particle, which would be the products with low electron number such as Li₃N. In fact, the EDS results shown in Figure 4-1-3 (e) indicated that Si was absent at the spots with low contrast. On the other hand, even at similar low contrast part, Si was observed, suggesting that determination of the product distribution is difficult for Li-Si case from only contrast of the image.

4-1-3 Li-Ge alloy

Li₂₂Ge₅ single phase was obtained by mechanical alloying and annealing, because the diffraction peaks observed in the XRD pattern shown in Figure 4-1-7 were totally assigned as single phase of Li₂₂Ge₅. DSC profiles of the Li-Ge alloy (Li₂₂Ge₅) under N₂ pressure of 0.1 and 3 MPa were shown in Figure 4-1-6. In the case of Li₂₂Ge₅, the reaction with N₂ under 0.1 MPa started from around 150 °C with a weak exothermic peak as shown in Figure 4-1-6. Other two exothermic peaks were more clearly observed at higher temperature than 350 °C. Under 3 MPa of N₂, clear exothermic peak was observed from 310 °C. After the reaction of Li₂₂Ge₅ with 0.1 MPa of N₂ at 500 °C, the starting phase of Li₂₂Ge₅ remained, and Li₇Ge₂ and unknown phases were generated. Because Li₂₂Ge₅ phase disappears after the reaction at 3 MPa of N₂ condition, the remaining Li₂₂Ge₅ is caused by kinetic reasons. Although the Li composition in the alloy is decreased by the reaction with N₂, Li₃N was not found. It is possible that the nano-sized or amorphous Li₃N and/or ternary nitride phase (Li-Ge-N) are formed. The reaction yield

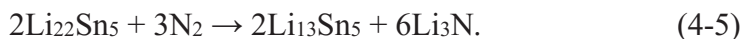
estimated by assumption for generating Li_7Ge_2 and Li_3N as products was higher than 100 %, suggesting that the unexpected reaction possibly proceeds as main reaction,



The TEM image is shown in Figure 4-1-3 (c). Although the Ge is high atomic number compared with those of Li and N, no clear difference in contrast was observed. When the expected nitrogenation reaction proceeds, the products should be generated around the particles because only Li with high mobility is diffused from inside of alloys to surface and form Li_3N . However, considering the ternary nitride formation indicated from the above XRD results, it is expected that N atoms should be diffused into Li-Ge alloy. In this case, the contrast difference in TEM image should not be clearly observed. In fact, the EDS spectra obtained at different spots in the particles were almost same results. The above results indicate that the Li-Ge alloy can dissociate and react with N_2 with different reaction path from the C and Si cases.

4-1-4 Li-Sn alloy

XRD patterns of the as-synthesized Li-Sn alloy corresponded to $\text{Li}_{22}\text{Sn}_5$ phase as shown in Figure 4-1-9. Figure 4-1-8 shows DSC profiles of $\text{Li}_{22}\text{Sn}_5$ under the N_2 pressure of 0.1 and 3 MPa. From the DSC profile obtained under 0.1 MPa of N_2 , multi-exothermic peaks were observed in a wide temperature range from a room temperature to 500 °C. By the reaction with N_2 , $\text{Li}_{22}\text{Sn}_5$ was changed to Li_7Sn_2 and $\text{Li}_{13}\text{Sn}_5$ as shown in the XRD results. It is expected that the nano-sized Li_3N is formed as the reaction product because the any other nitrides and unknown phases are not found. Li_7Sn_2 is an intermediate phase because only this phase was observed at 360 °C, and $\text{Li}_{13}\text{Sn}_5$ with the lower Li composition would be final product at 500 °C. From the above results, it is concluded that the Sn system shows the lowest N_2 -dissociation temperature, which is almost room temperature, among the Li-M alloys. In the case of Li-Sn alloy, no clear difference was found between the experimental results under 0.1 and 3 MPa of N_2 pressures. In other words, reaction is very fast even at low pressure of 0.1 MPa and low composition alloys are easily form,



The clearest contrast and difference between the products and starting alloy were noticed in TEM image and EDS spectra as shown in Figure 4-1-3 (d) and (f), respectively. Here, it is difficult to analyze nitrogen because the level of carbon and oxygen contaminations is higher than that of products at the surface parts. The low contrast parts observed around particle included no Sn component, indicating that these parts were Li_3N as the product of reaction. Figure 4-1-10 shows TEM image of the other particle of Li-Sn alloy after the nitrogenation and the high magnification images of the product parts. Some products formed nano-tube and/or fiber shape.

Li_3N is layered crystal structure, thereby it would form the tubular and fibrous shape like carbon ⁴⁻²⁾. Figure 4-1-11 shows SEM and BE images of the nitrogenated Li-Sn alloy. Although the observed particle showed significant edges in SEM image, some parts become invisible in the case of BE image. This results indicate that the products are located at surface of particle and possesses lower electron number than Li-Sn alloy. The results obtained by both of TEM and SEM are well consistent and indicate the Li_3N formation.

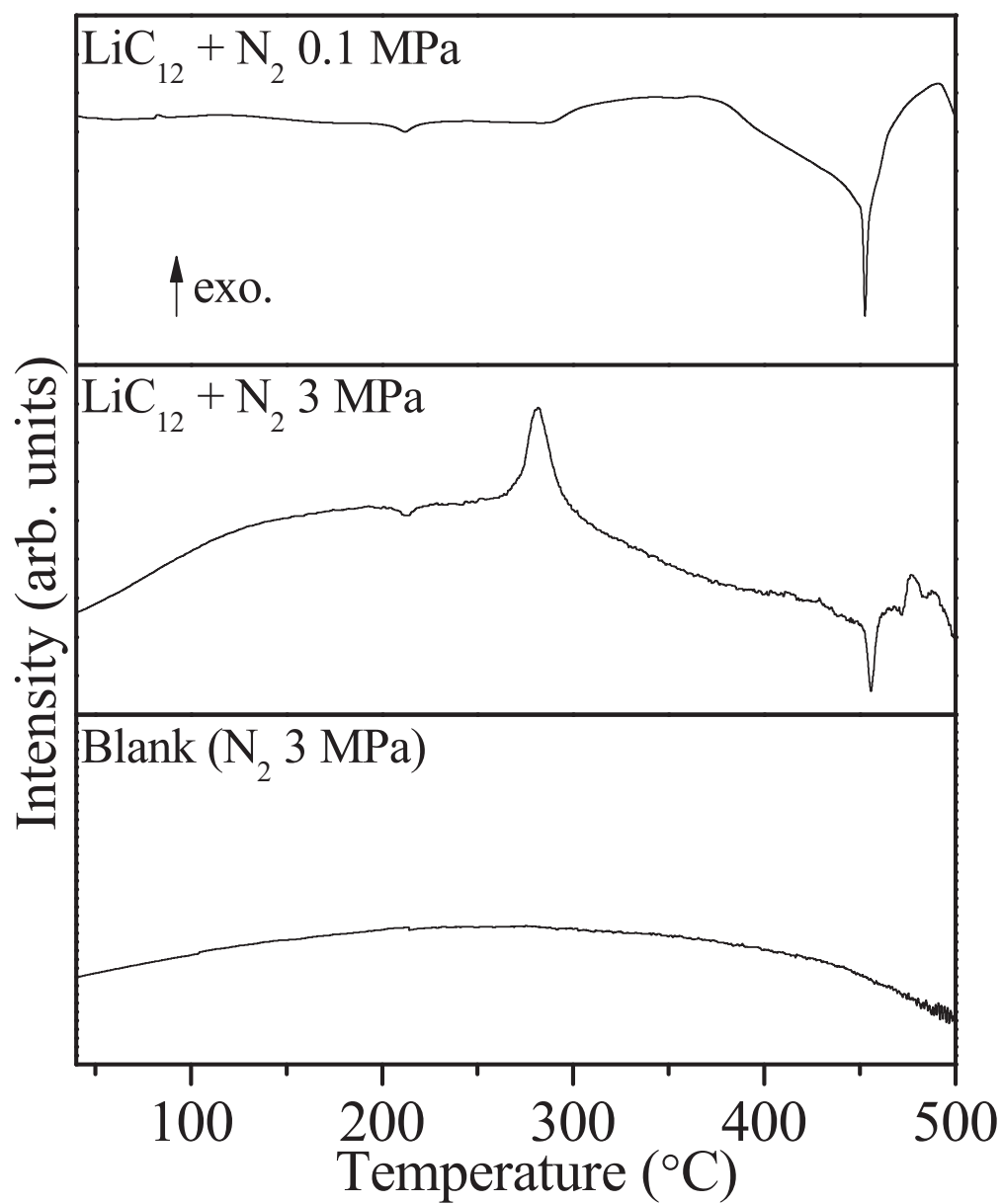


Figure 4-1-1 DSC profiles of the Li-C alloy under 0.1 MPa, 3 MPa of N_2 and blank.

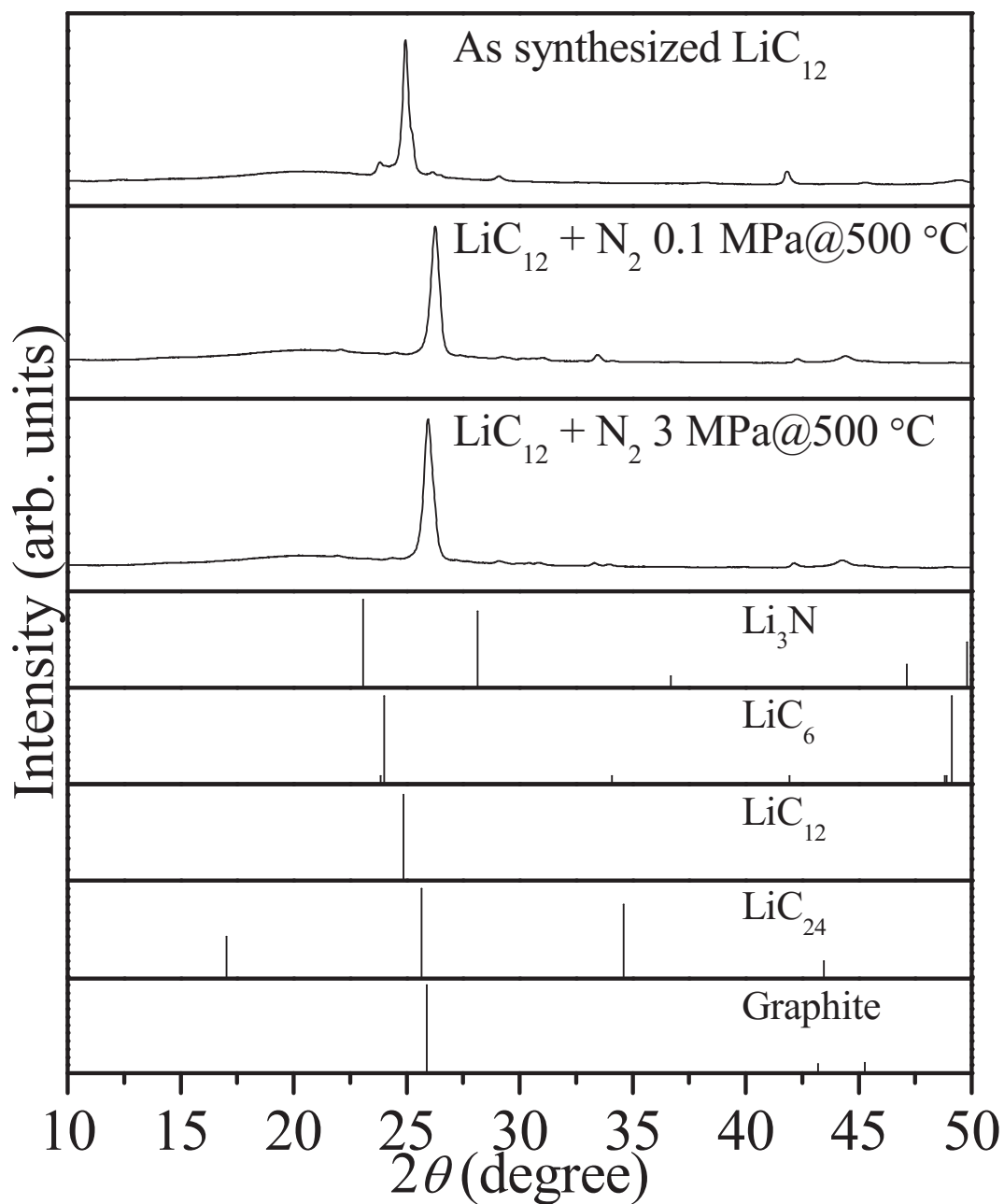


Figure 4-1-2 XRD patterns of as-synthesized LiC_{12} alloy and products after the reaction with N_2 ; XRD pattern of Li_3N (PDF01-075-8957), LiC_6 (PDF00-034-1320), LiC_{12} (PDF00-035-1046), LiC_{24} (PDF00-035-1047), and Graphite (PDF00-012-0212) are referred from databases.

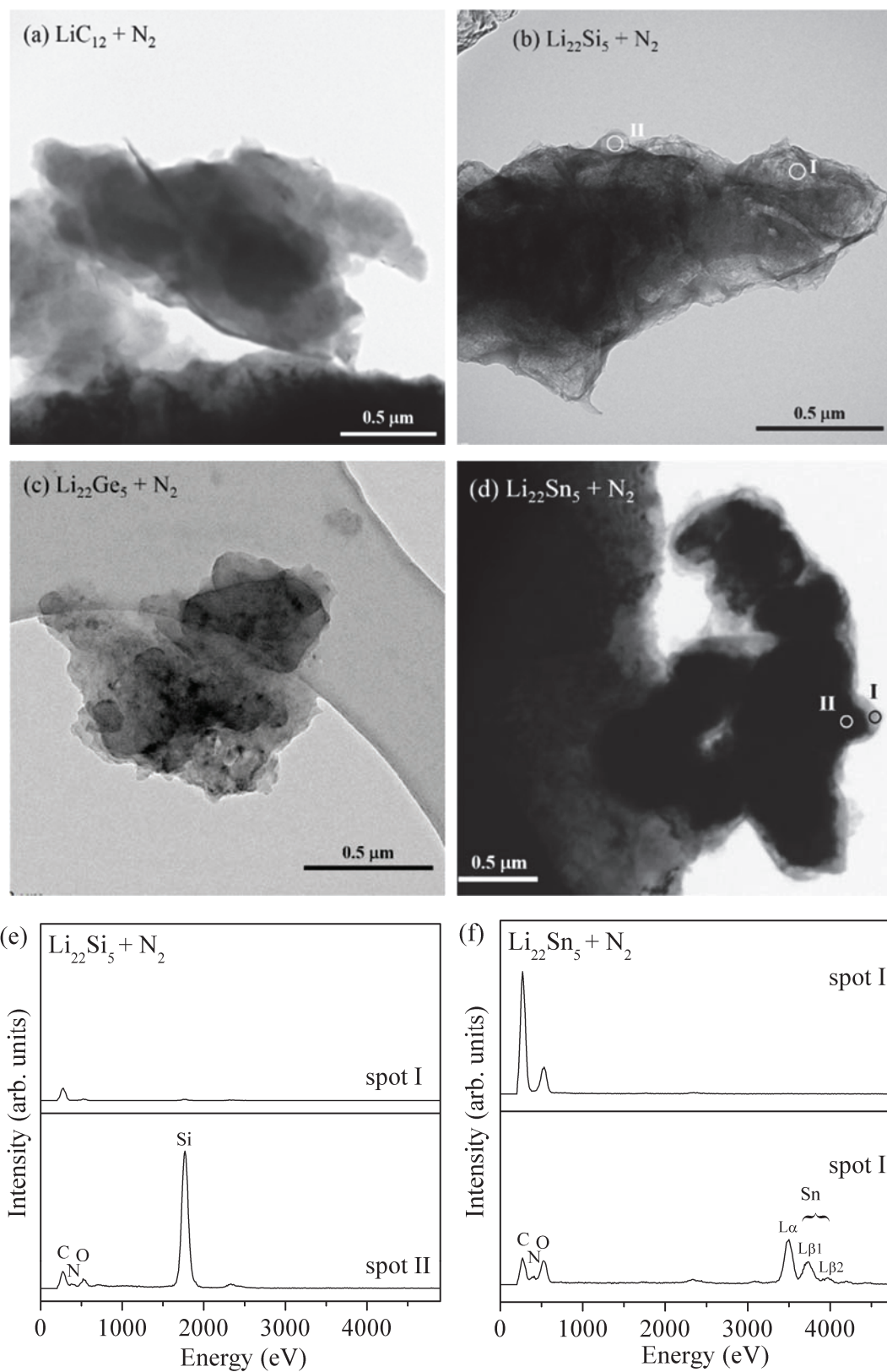


Figure 4-1-3 TEM images of (a) Li-C, (b) Li-Si, (c) Li-Ge, (d) Li-Sn alloys after the reaction with N_2 , and EDS spectra for (e) Li-Si and (f) Li-Sn alloys.

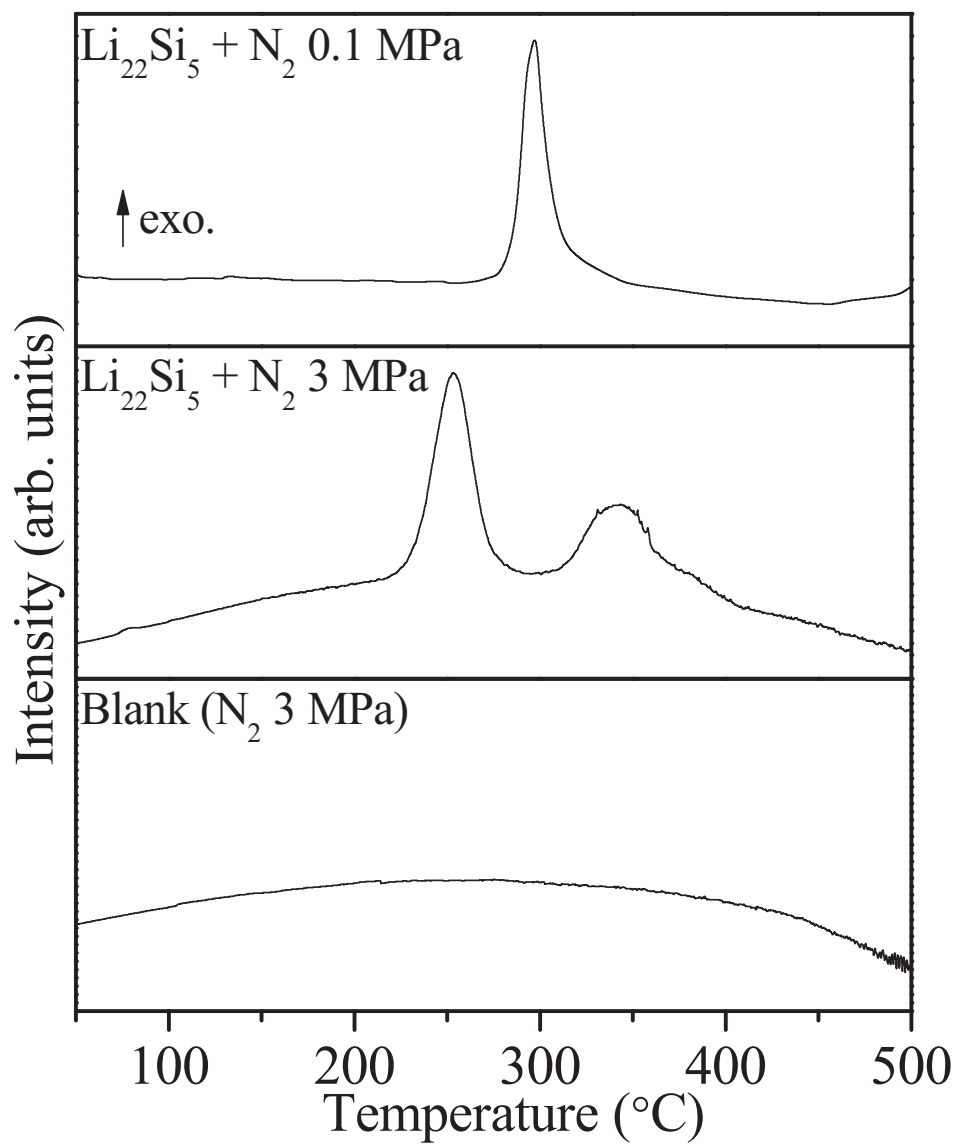


Figure 4-1-4 DSC profiles of the Li-Si alloy under 0.1 MPa, 3 MPa of N₂ and blank.

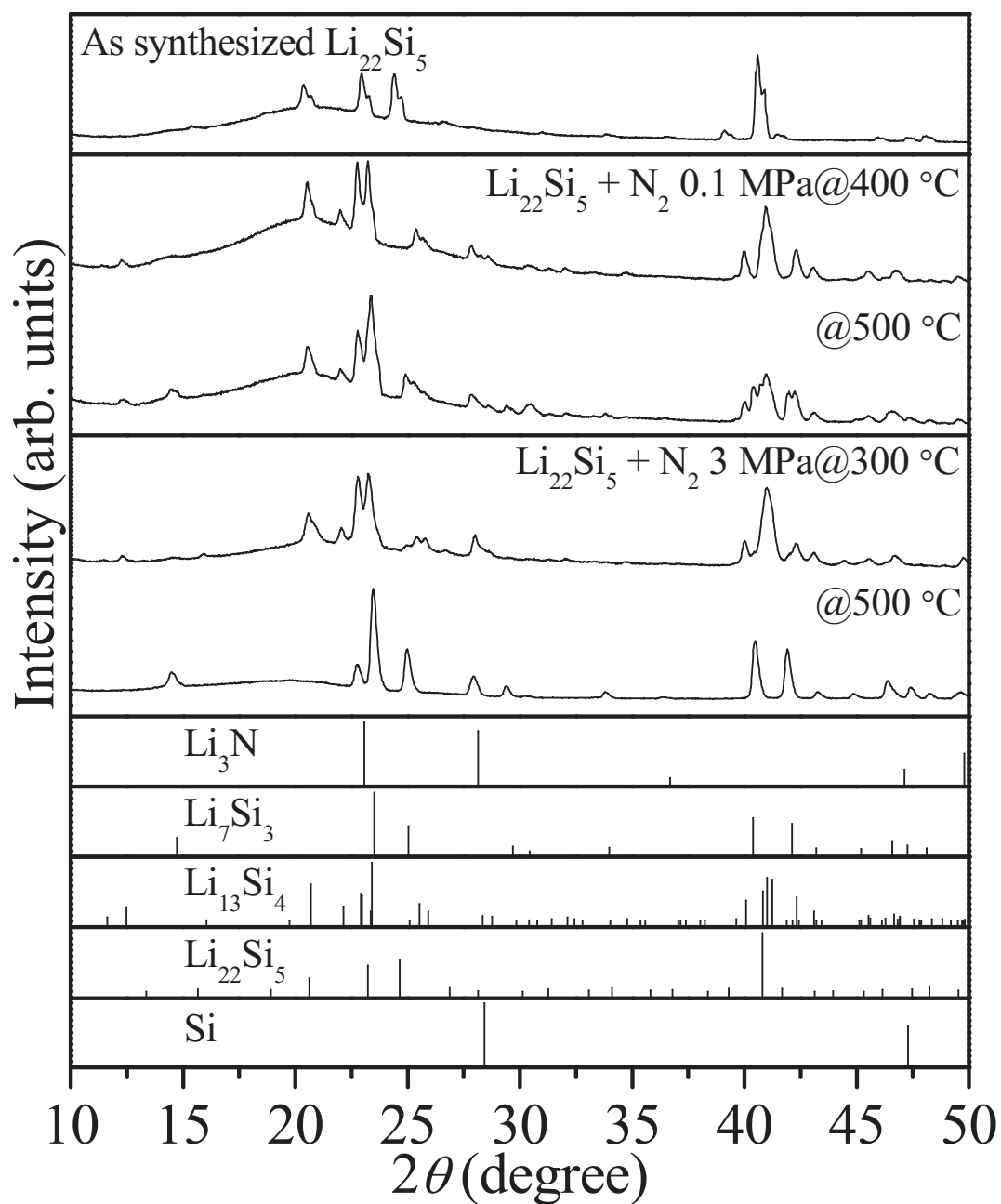


Figure 4-1-5 XRD patterns of as-synthesized $\text{Li}_{22}\text{Si}_5$ alloy and products after the reaction with N_2 ; XRD pattern of Li_3N (PDF01-075-8957), Li_7Si_3 (PDF01-089-0005), $\text{Li}_{13}\text{Si}_4$ (PDF01-089-0009), $\text{Li}_{22}\text{Si}_5$ (PDF01-077-2882), and Si (PDF00-005-0565) are referred from databases.

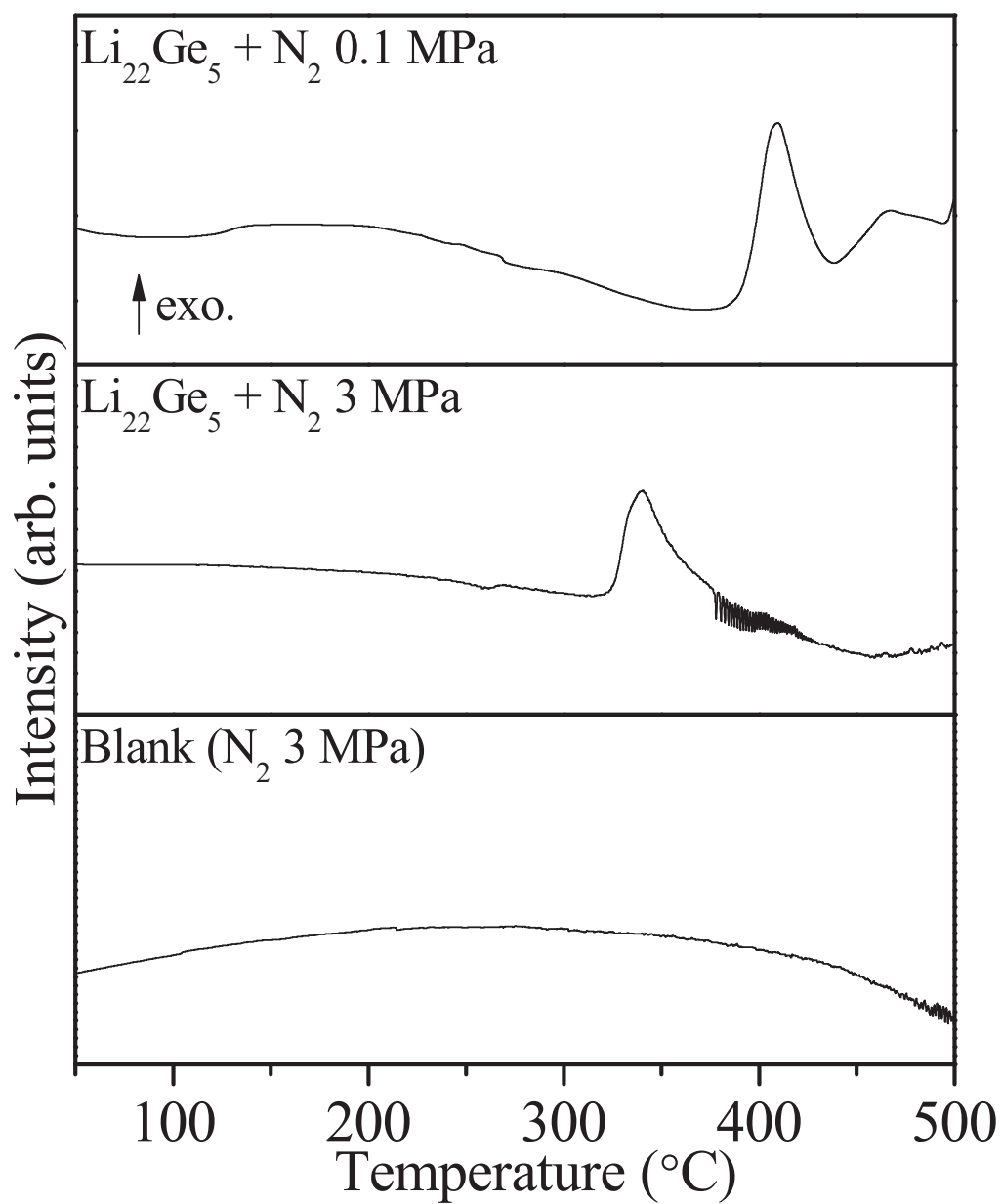


Figure 4-1-6 DSC profiles of the Li-Ge alloy under 0.1 MPa, 3 MPa of N_2 and blank.

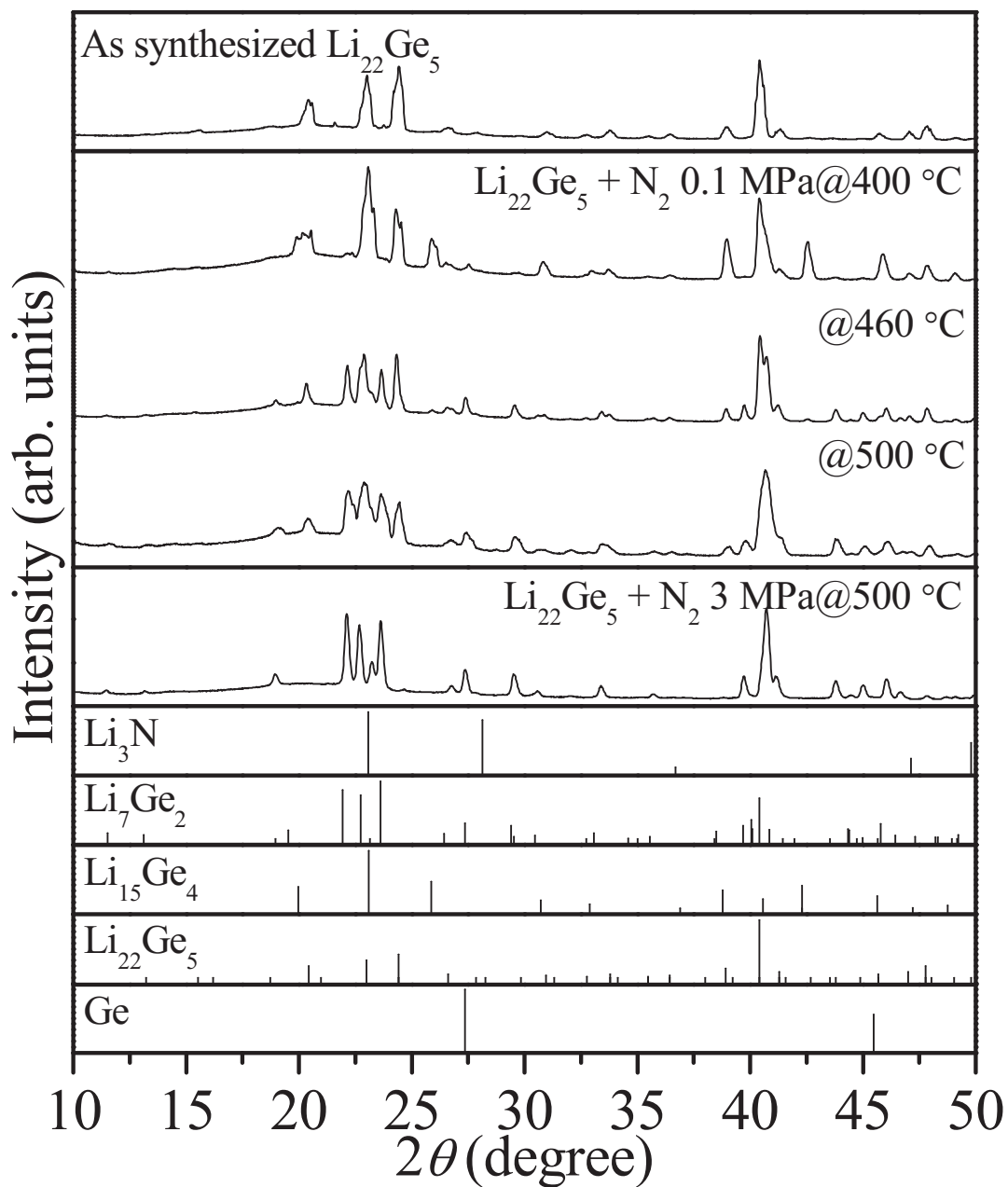


Figure 4-1-7 XRD patterns of as-synthesized $\text{Li}_{22}\text{Ge}_5$ alloy and products after the reaction with N_2 ; XRD pattern of Li_3N (PDF01-075-8957), Li_7Ge_2 (PDF01-080-0531), $\text{Li}_{15}\text{Ge}_4$ (PDF01-089-2584), $\text{Li}_{22}\text{Ge}_5$ (PDF01-017-0402), and Ge (PDF00-004-0545) are referred from databases.

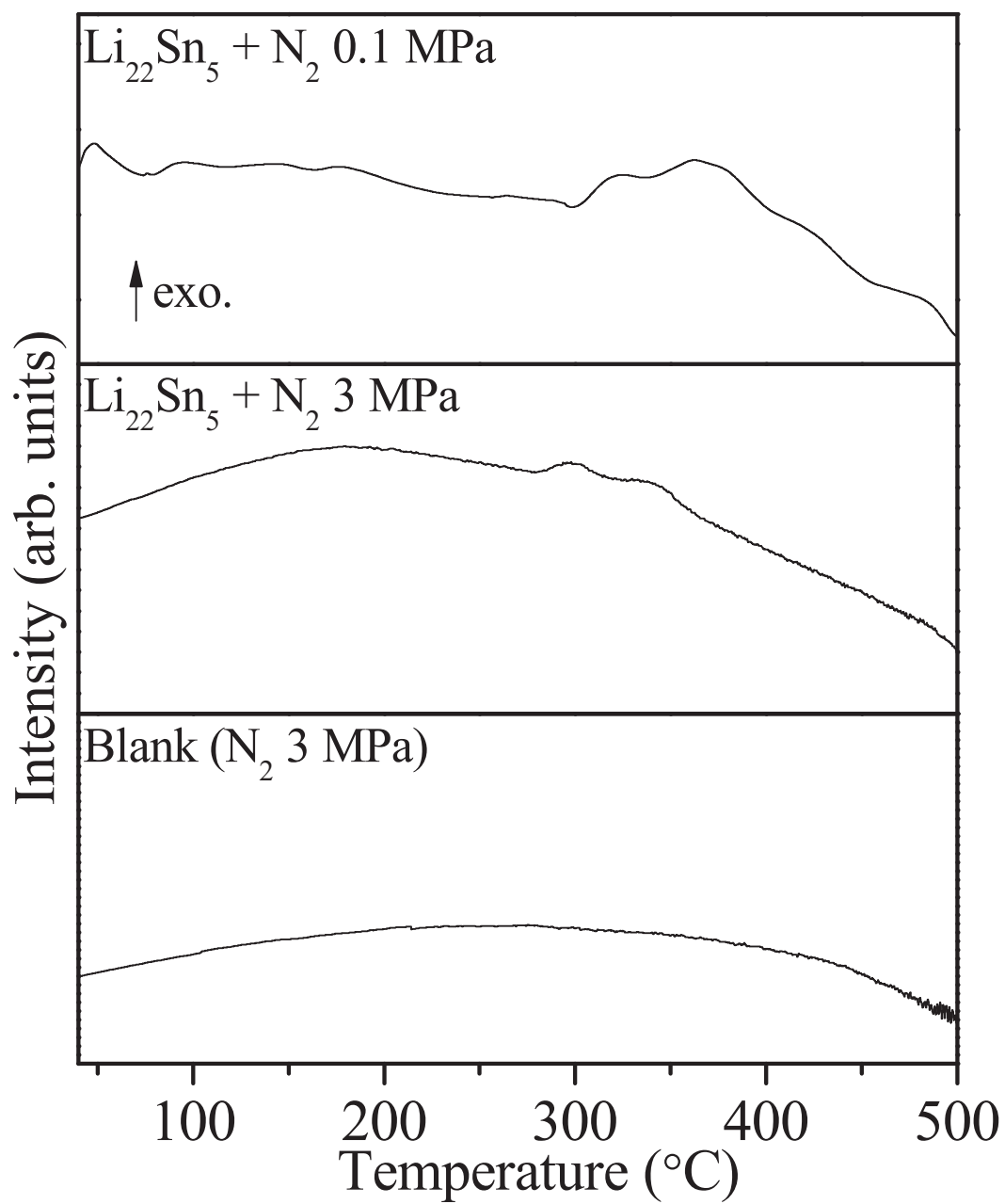


Figure 4-1-8 DSC profiles of the Li-Sn alloy under 0.1 MPa, 3 MPa of N_2 and blank.

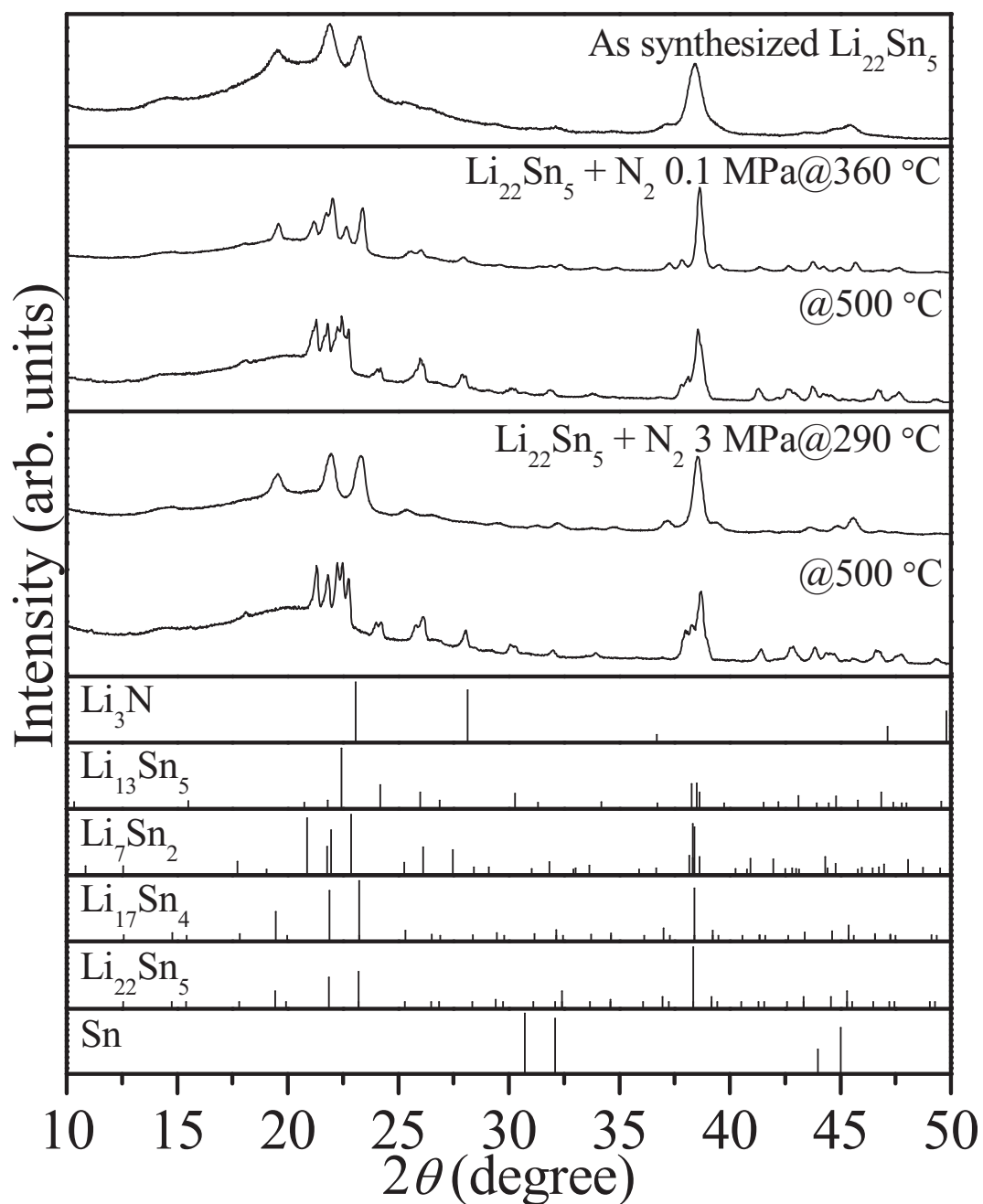


Figure 4-1-9 XRD patterns of as-synthesized $\text{Li}_{22}\text{Sn}_5$ alloy and products after the reaction with N_2 ; XRD pattern of Li_3N (PDF01-075-8957), $\text{Li}_{13}\text{Sn}_5$ (PDF03-065-4493), Li_7Sn_2 (PDF03-065-1419), $\text{Li}_{17}\text{Sn}_4$ (PDF01-070-9404), $\text{Li}_{22}\text{Sn}_5$ (PDF00-018-0753), and Sn (PDF00-004-0673) are referred from databases.

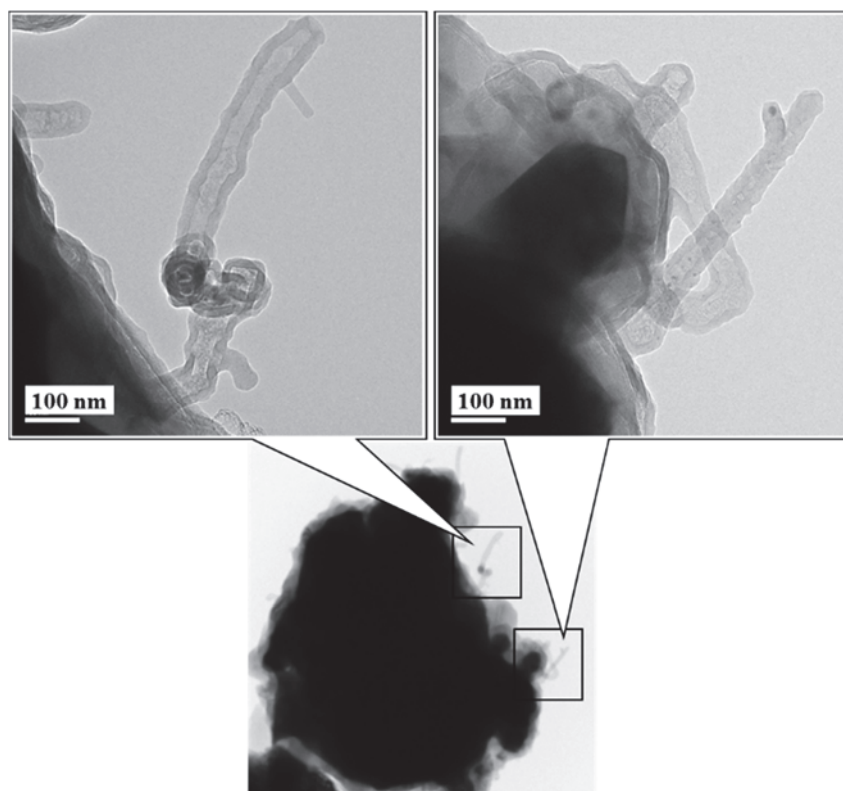


Figure 4-1-10 TEM images of products after the reaction between Li-Sn alloy and N_2 .

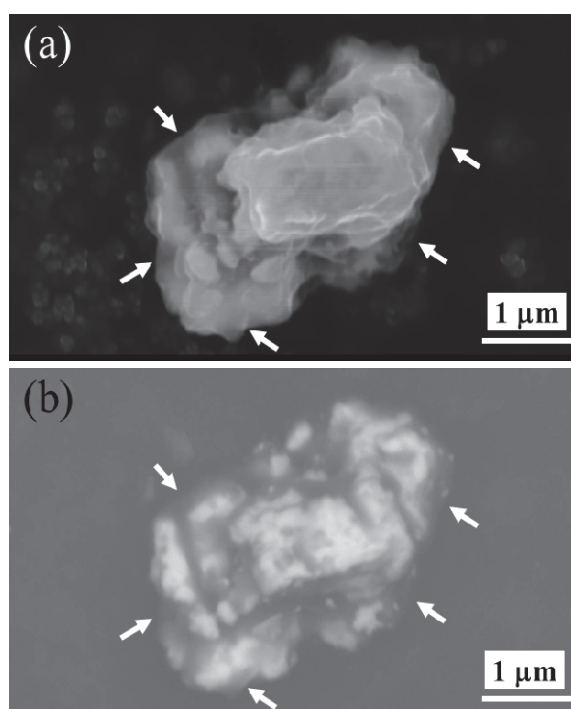


Figure 4-1-11 (a) SEM and (b) BS images of the Li-Sn alloy particle after the reaction with N_2 .

4-2 Denitrogenation

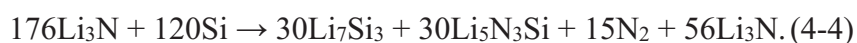
To utilize the dissociated and atomic N in Li₃N, the reverse reaction, which is named as “denitrogenation”, is also important. The reaction properties of Li₃N and M (M=C, Si, Ge, and Sn) mixtures, which is ideal final products, to desorb N₂ with alloy formation were systematically investigated.

4-2-1 Mixture of C and Li₃N

Fig. 4-2-1 shows TG-MS profiles of the Li₃N-M mixtures, and Fig. 4-2-2 shows XRD patterns of as-synthesized mixtures and products. The mass number 28 plotted in the MS profiles corresponds to N₂. Although higher temperature than 1000 °C (the partial pressure of N₂ is assumed to be 0.1 MPa) is thermodynamically necessary to decompose Li₃N itself to Li and N₂, all the mixtures showed N₂ desorption below 600 °C. The Li₃N-C mixtures desorbed N₂ in broad temperature range from 100 to 400 °C with low intensity and only 2.0 wt% of weight loss. The reaction yield is estimated as 38 %, assuming that the LiC₆ is completely generated. The diffraction peak corresponding to graphite was broadened by the mechanical ball-milling and not changed after the N₂ desorption, suggesting that the reaction proceeded with the generation of nano-sized or amorphous Li-C alloys at only small parts. Here, a broad peak in the range from 15 to 35 degree is essential and should be caused by the grease and/or polyimide sheet.

4-2-2 Mixture of Si and Li₃N

In the case of Si system, the N₂ desorption was clearly observed from 350 °C as shown in Figure 4-2-1. Figure 4-2-3 shows the XRD patterns of the mixture of Si and Li₃N, and reaction product after the TG-MS measurements. After the measurement at 600 °C, diffraction peaks corresponding to Si disappeared, and the Li₇Si₃ phase was found as a main product, where ternary nitride (Li₅N₃Si) was possibly formed as by-product. The weight loss due to the reaction yield is estimated to be 93 % assuming that a following reaction proceed,

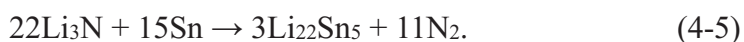


4-2-3 Mixture of Ge and Li₃N

As shown in Figure 4-2-4, no diffraction peaks were observed in the XRD pattern of the as-synthesized Li₃N and Ge mixture, suggesting that both of materials were changed to nano-grains or amorphous phase during the mechanical ball-milling process. The Li₃N-Ge mixture required the higher temperature to release N₂ compared with other mixture. The N₂ desorption was observed from 500 °C and continuously proceeded at more than 600 °C. To complete the N₂ desorption, the mixture was heat-treated at 600 °C for 8 h under a dynamic vacuum condition by using batch cell. The XRD patterns of the product obtained after the TG-MS measurement and the heat treatment at 600 °C are shown in Figure 4-2-4. After just heating up to 600 °C, the observed peaks were not assigned to the any materials in the database. On the other hand, Li₂GeN₂ was formed by the heat treatment for 8 h, suggesting that the unknown phase should be intermediate and precursor of the ternary nitride.

4-2-4 Mixture of Sn and Li₃N

In the case of Li₃N and Sn mixture, nano or amorphous states were formed by the ball-milling as shown in Figure 4-2-5. The N₂ desorption proceeded in the temperature range from 400 to 600 °C with multi steps. Although it was difficult to distinguish each reaction process due to overlapping the N₂ desorption profiles, the composition of Li and Sn were gradually changed with N₂ desorption to form alloys with higher Li composition. At 600 °C, Li₇Sn₂ and Li₂₂Sn₅ were observed as reaction products. The Li₇Sn₂ phase would be main product at this conditions because the 10.2 wt% of weight loss was not corresponding to the formation of Li₂₂Sn₅, which is fully Li composed alloy. Besides, the formation of ternary compounds were not observed in this reaction as by-product. From the MS profiles, it is expected that the reaction was not completed at 600 °C, indicating that the Li₃N and Sn mixture is possibly changed to Li₂₂Sn₅ for longer reaction time or at slightly higher temperature. Therefore, it is recognized that only Li-Sn alloy is a potential material to control the N₂ dissociation and recombination with the largest amount of utilizable Li below 600 °C as a following full-reversible reaction,



Generally, it is expected that the reactions with phase separation such as the Li_3N formation requires high temperature because of the long diffusion distance. However, Li is small element and featured the high mobility known as reactions of lithium ion battery. Therefore, it is speculated that the nitrogenation and denitrogenation reactions of the Li alloys at lower temperature would be realized by the high reactivity with N_2 and mobility of Li.

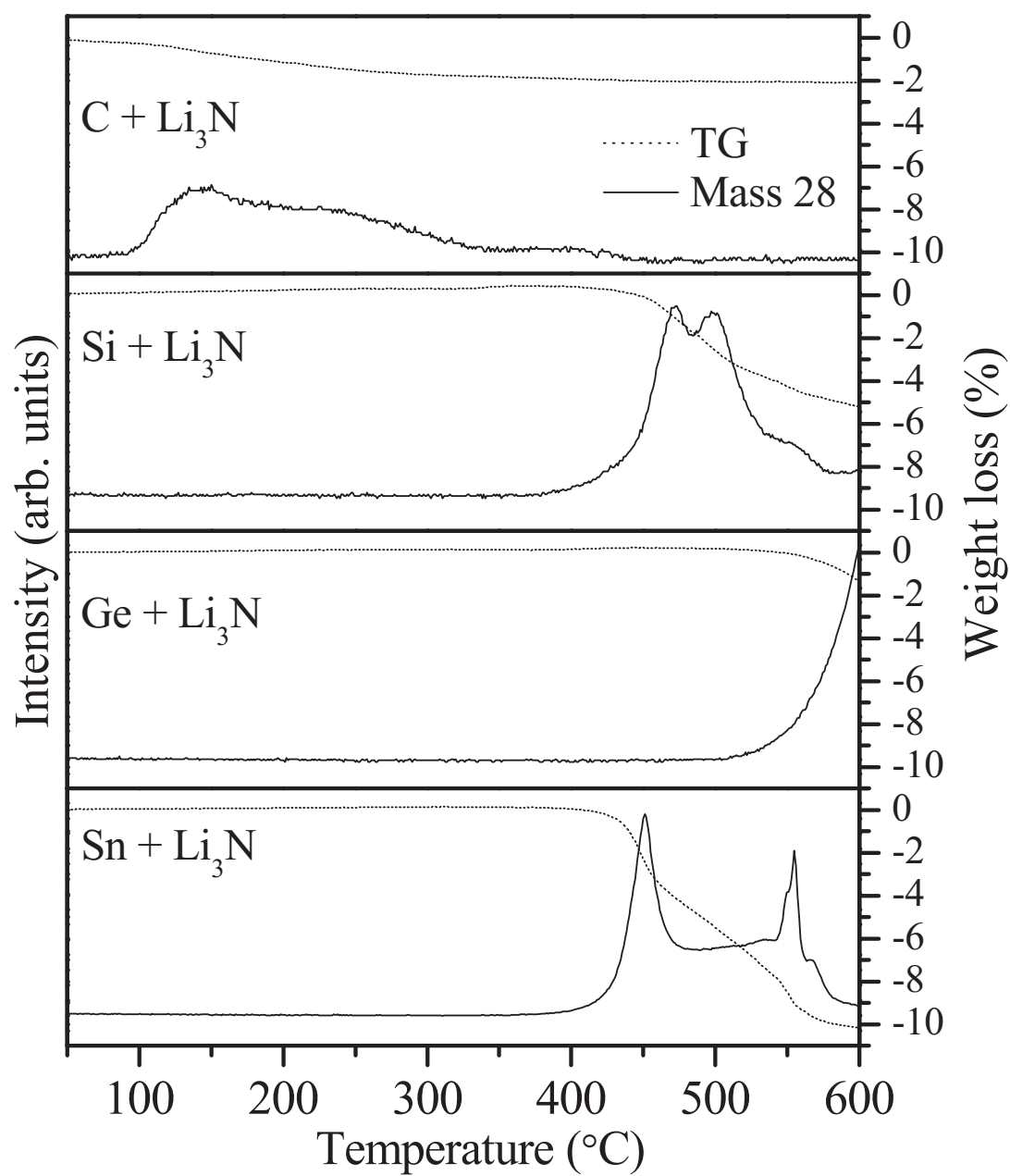


Figure 4-2-1 TG-MS profiles of Li_3N and M mixtures.

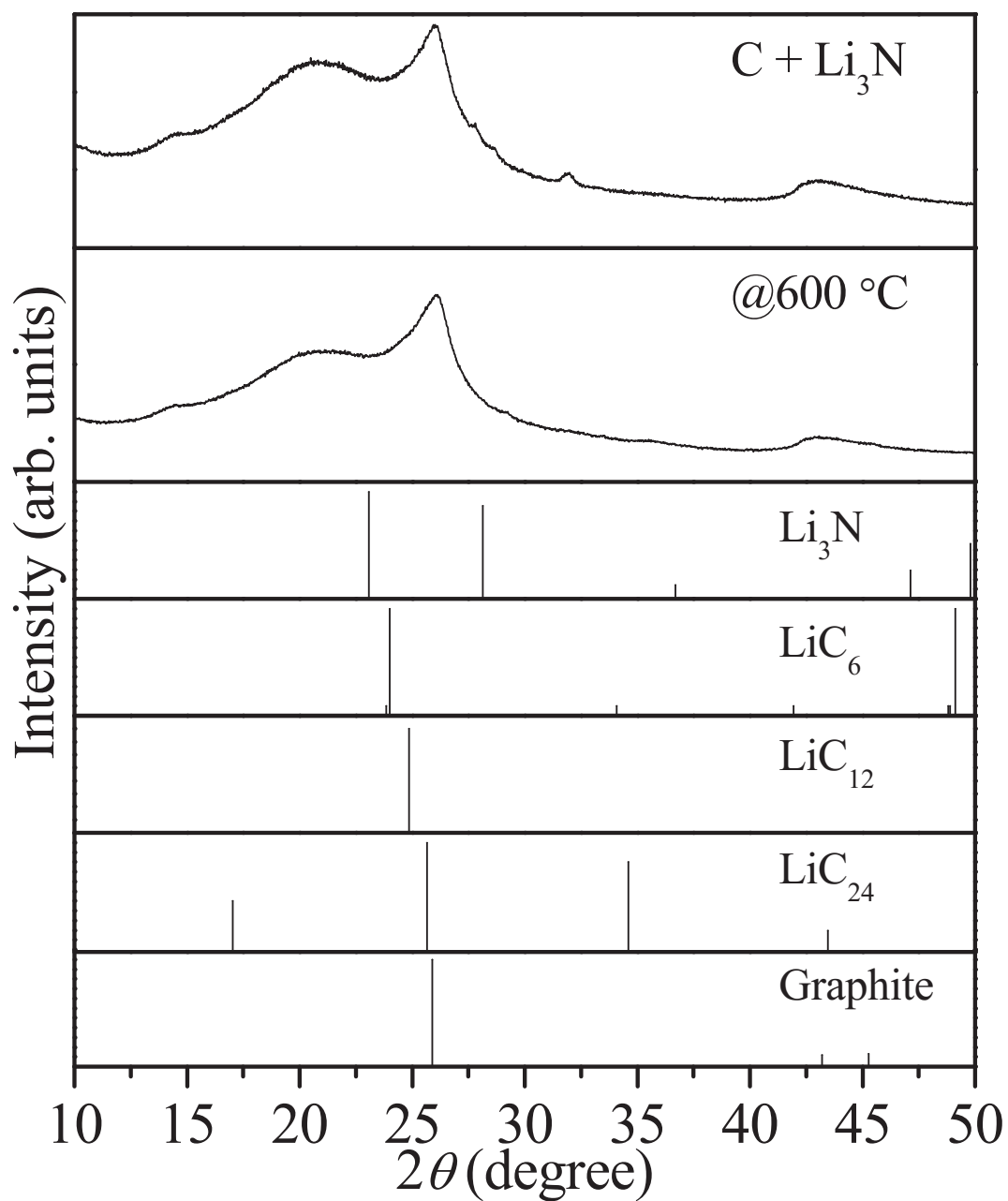


Figure 4-2-2 XRD patterns of as-synthesized C and Li₃N mixture and products after the TG-MS measurement; XRD pattern of Li₃N (PDF01-075-8957), LiC₆ (PDF00-034-1320), LiC₁₂ (PDF00-035-1046), LiC₂₄ (PDF00-035-1047), and Graphite (PDF00-012-0212) are referred from databases.

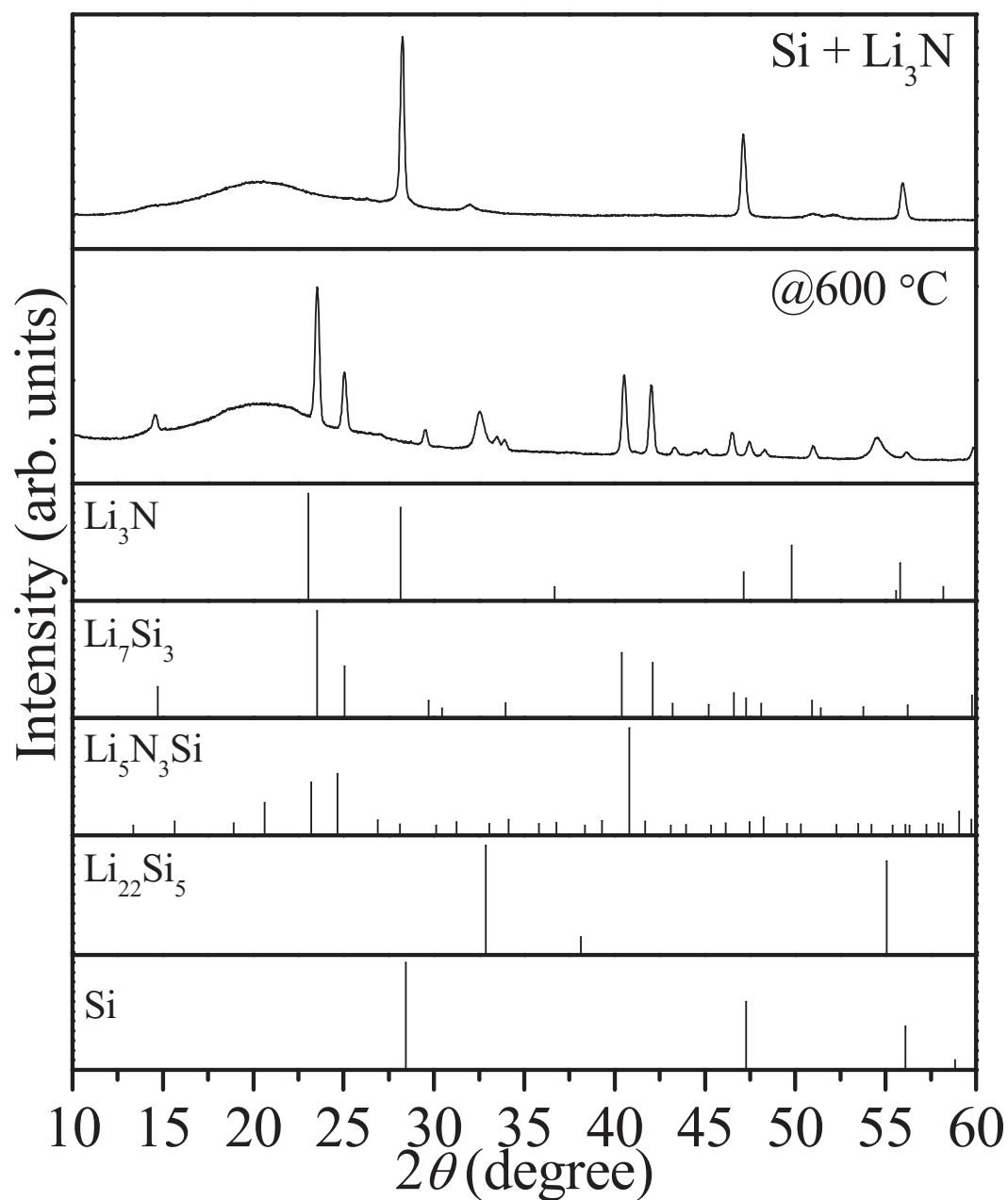


Figure 4-2-3 XRD patterns of as-synthesized Si and Li₃N mixture and products after the TG-MS measurement; XRD pattern of Li₃N (PDF01-075-8957), Li₇Si₃ (PDF01-089-0005), Li₅N₃Si (PDF00-040-1446), Li₂₂Si₅ (PDF01-077-2882), and Si (PDF00-005-0565) are referred from databases.

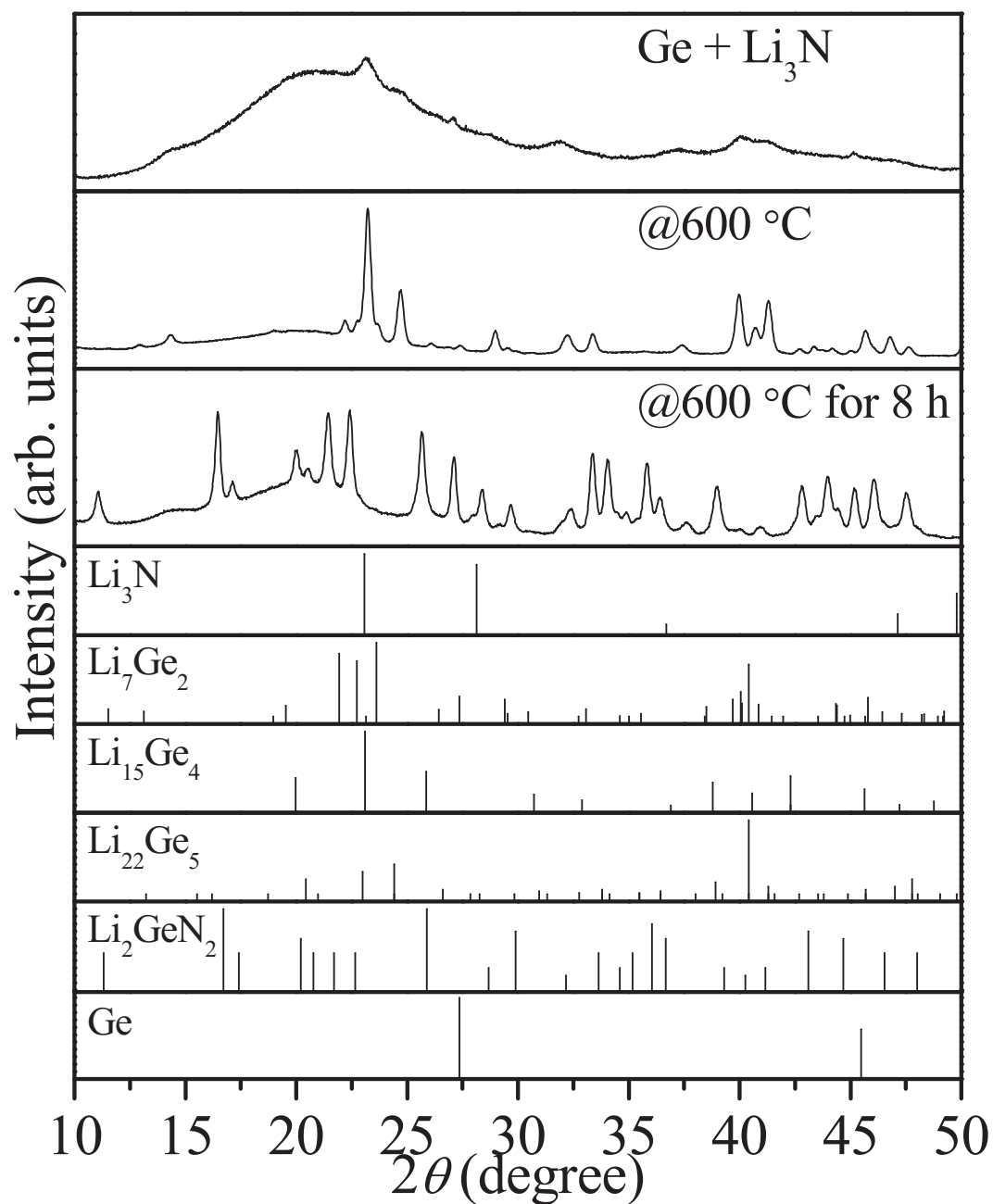


Figure 4-2-4 XRD patterns of as-synthesized Ge and Li₃N mixture and products after the TG-MS measurement; XRD pattern of Li₃N (PDF01-075-8957), Li₇Ge₂ (PDF01-080-0531), Li₁₅Ge₄ (PDF01-089-2584), Li₂₂Ge₅ (PDF01-017-0402), Li₂GeN₂ (PDF00-028-0565), and Ge (PDF00-004-0545) are referred from databases.

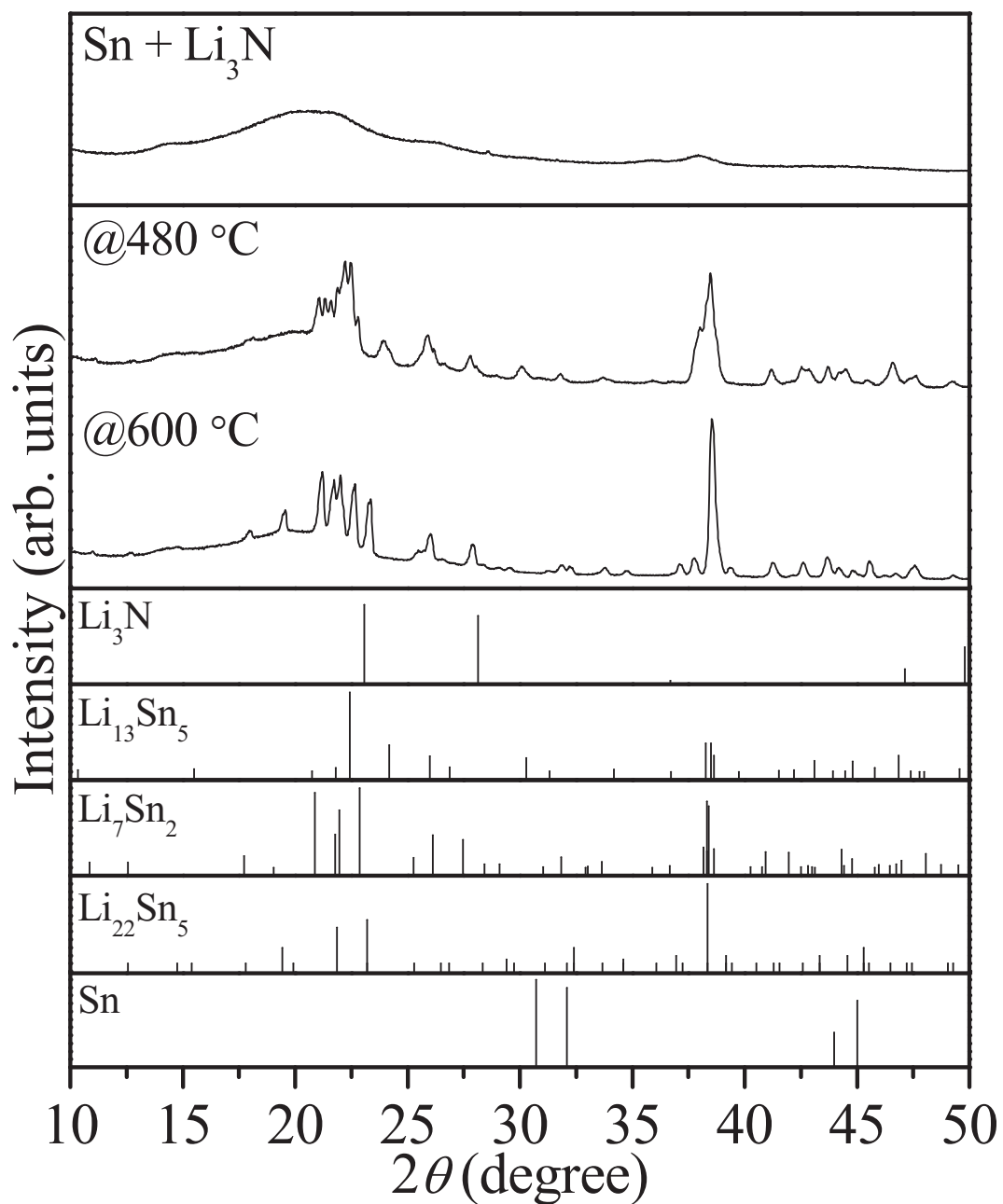


Figure 4-2-5 XRD patterns of as-synthesized Sn and Li₃N mixture and products after the TG-MS measurement; XRD pattern of Li₃N (PDF01-075-8957), Li₁₃Sn₅ (PDF03-065-4493), Li₇Sn₂ (PDF03-065-1419), Li₂₂Sn₅ (PDF00-018-0753), and Sn (PDF00-004-0673) are referred from databases.

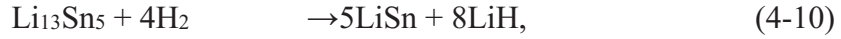
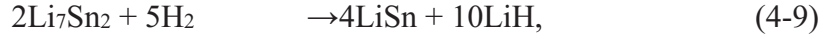
4-3 Ammonia synthesis

Ammonia synthesis properties by using the nitrogenation and denitrogenation reactions of Li-M alloys were investigated. Goshome *et al.* reported that NH₃ can be generated by the reaction between Li₃N and H₂ under flow conditions as following equation ⁴⁻³⁾,



If Li₃N is formed by the reaction of Li-M alloys with N₂, NH₃ should be generated by the above reaction. The DSC-MS measurements of the nitrogenated Li-M alloys were performed under 0.5 MPa of H₂ flow conditions, and the results are shown in Figure 4-3-1. Here, the MS signals are observed at slightly delayed temperature from the DSC signals due to technical reasons of our experimental system. Exothermic reactions were observed from about 150 °C during increasing temperature up to 300 °C for all samples. It is expected that these exothermic peaks are originated in the NH₃ generation from Li₃N and/or hydrogenation of the alloys. The MS signal corresponding to NH₃ (Mass 17) was observed for C, Si, and Sn systems, suggesting that the expected NH₃ synthesis reaction proceeded. On the other hand, the NH₃ generation was not found in the case of Ge system. The NH₃ generation by eq. (4-6) requires Li₃N, however unknown phase is formed as the products after the nitrogenation of Li₂₂Ge₅ alloy. This would be the reason for no NH₃ generation. Figure 4-3-2, 4-3-3, 4-3-4, and 4-3-5 show XRD patterns of the products after the reaction with H₂ and nitrogenated Li-C, Li-Si, Li-Ge, and Li-Sn alloys, respectively. Here, when only Li₃N is converted to NH₃ and LiH by the reaction with H₂ according to eq. (4-6), the alloy phases should not be changed and remain even after the process of above reaction. The main diffraction peak observed for the C system was the same position after the reaction, and a shoulder appeared at higher angle, suggesting that the small amount of Li is removed from the graphite layers. In the cases of Si and Ge systems, the intensity of diffraction peaks assigned to Li₇Si₃ and Li₇Ge₂, which are the alloy phases with lower Li composition, was increased compared with the XRD patterns of the products after the nitrogenation shown in Figure 4-3-3 and 4-3-4. The Sn system revealed clear difference before and after the reaction with H₂, and then Li₇Sn₂ and Li₁₃Sn₅ generated by the nitrogenation was totally changed to LiSn. These results indicated that

the following hydrogenation of the Li-M alloys proceeded to form LiH in addition to the reaction of NH₃ generation by eq. (4-6),



where it would be difficult to observe diffraction peaks corresponding to LiH because of the low electron number. From the above results, it was clarified that NH₃ can be synthesized from the nitrogenated Li-C, Li-Si, and Li-Sn alloys, indicating that Li₃N should be formed as products for these alloys. The results obtained by the NH₃ synthesis are quite consistent with the nitrogenation properties of the Li-M alloys.

The final products after the NH₃ synthesis can be recycled back to Li-M alloy with releasing H₂ below 500 °C⁴⁻⁴⁾. Thus, the N₂ dissociation and recombination reactions of Li-M alloys can be utilized as the pseudo-catalyst for the NH₃ synthesis. The reaction mechanism for the dissociation of nitrogen triple bonds are totally different compared to employing the typical catalyst⁴⁻⁵⁻⁸⁾. The conditions required for the NH₃ synthesis by using the reactions of Li alloys are less than 500 °C and 0.5 MPa, which is milder than those of conventional Haber-Bosch process operated at 400-600 °C under 20-35 MPa. Even though 1 MPa of pressure is necessary when the active Ru catalyst is used, NH₃ can be obtained at lower temperature without rare metal catalysts in the case of the proposed synthesis process. Consequently, the pseudo-catalytic process using the Li alloys are expected as a potential technique as small-scale and distributed-type NH₃ synthesis technique although the Haber-Bosch process is well established for mass production. As discussed above, Li₃N generated from the alloys by the reaction with N₂ in nano-size, indicating that the nano-Li₃N has high reactivity for other reaction. Furthermore, it is possible that the nano-size and reactivity of Li₃N is preserved during the utilization cycles because Li is returned into atomic states to form alloy phases, suggesting that the reactions using Li-M alloys are expected as a “self-activation” process. The feasibility of the Li-M alloys as pseudo-catalyst for synthesis of various nitrides and their cycle properties should be investigated in further detail as future works.

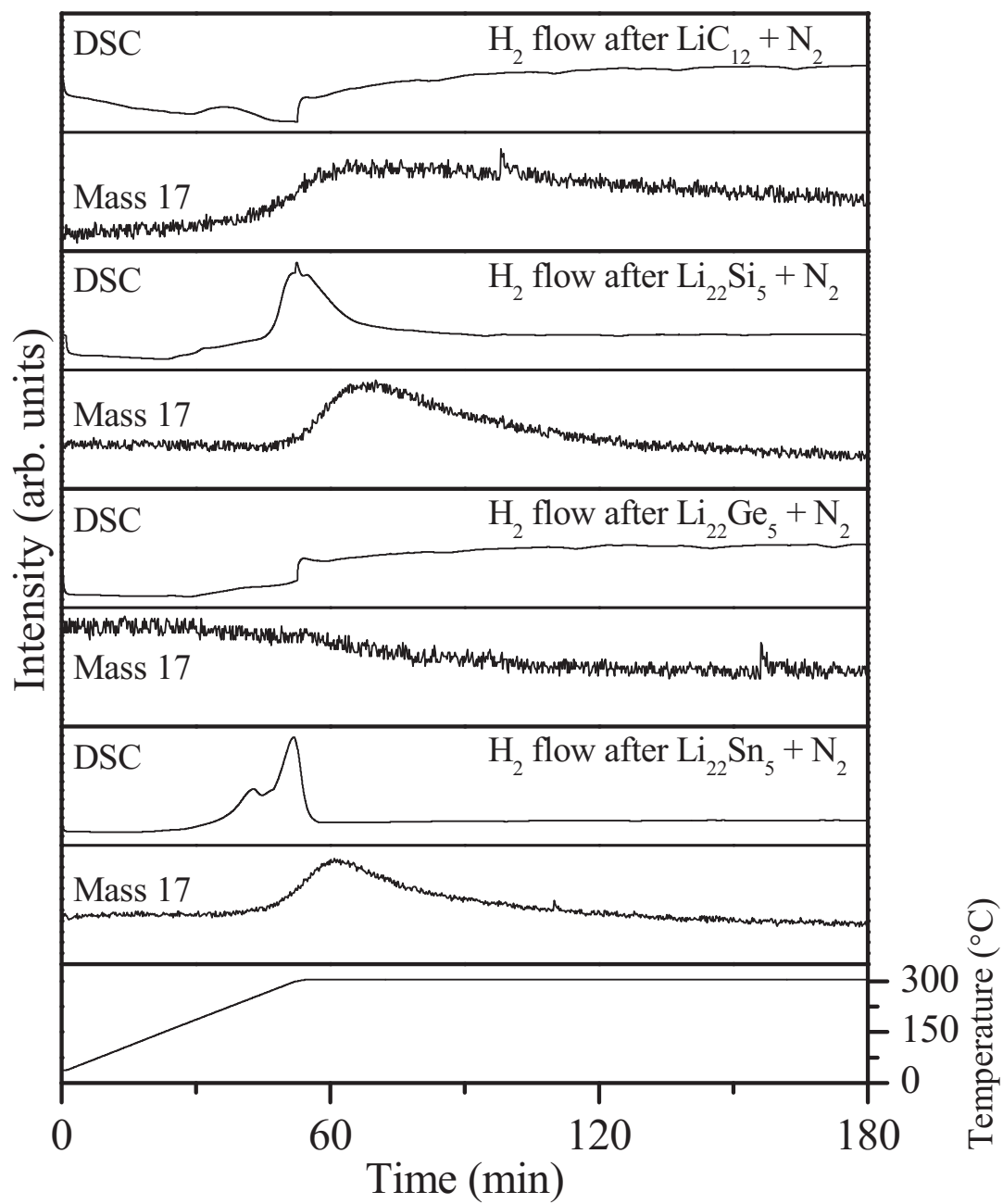


Figure 4-3-1 DSC-MS profiles of the nitrogenated Li-M alloys under N_2 flow condition.

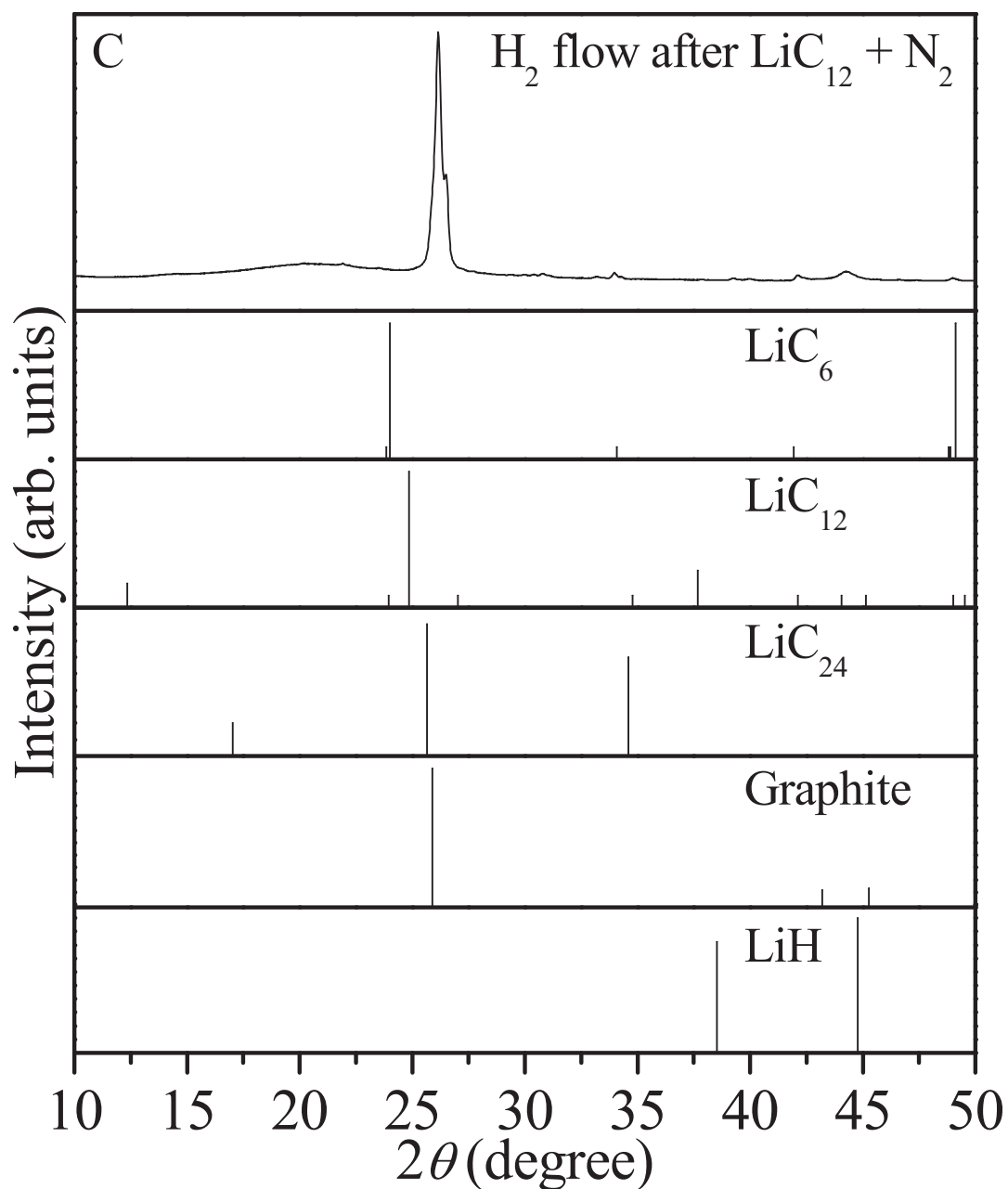


Figure 4-3-2 XRD patterns of nitrogenated Li-C alloy under N_2 condition after the DSC-MS measurement; XRD pattern of LiC_6 (PDF00-034-1320), LiC_{12} (PDF00-035-1046), LiC_{24} (PDF00-035-1047), LiH (PDF#78-0842), and Graphite (PDF00-012-0212) are referred from databases.

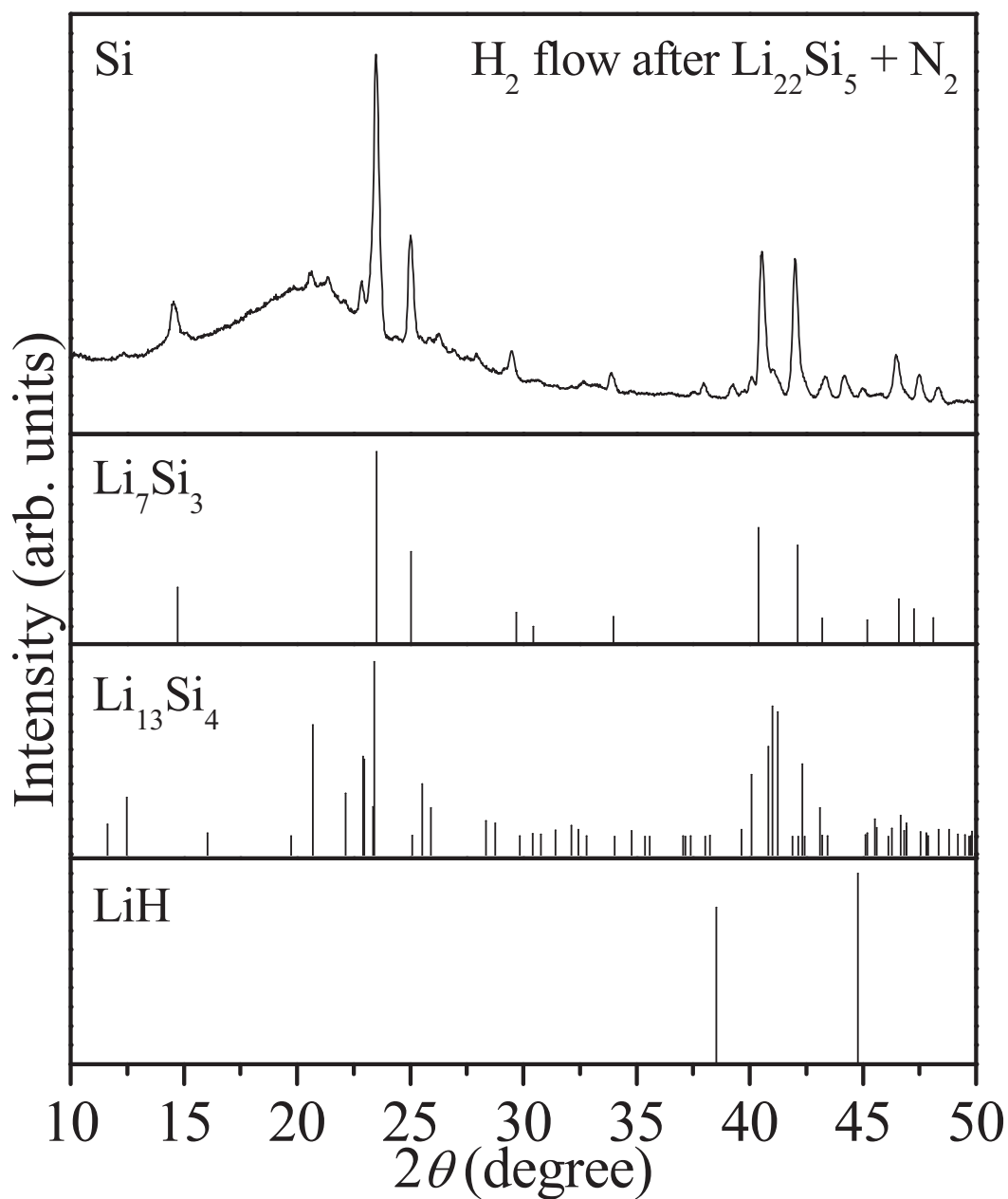


Figure 4-3-3 XRD patterns of nitrogenated Li-Si alloy under N_2 condition after the DSC-MS measurement; XRD pattern of Li_7Si_3 (PDF01-089-0005), $Li_{13}Si_4$ (PDF01-089-0009), and LiH (PDF#78-0842) are referred from databases.

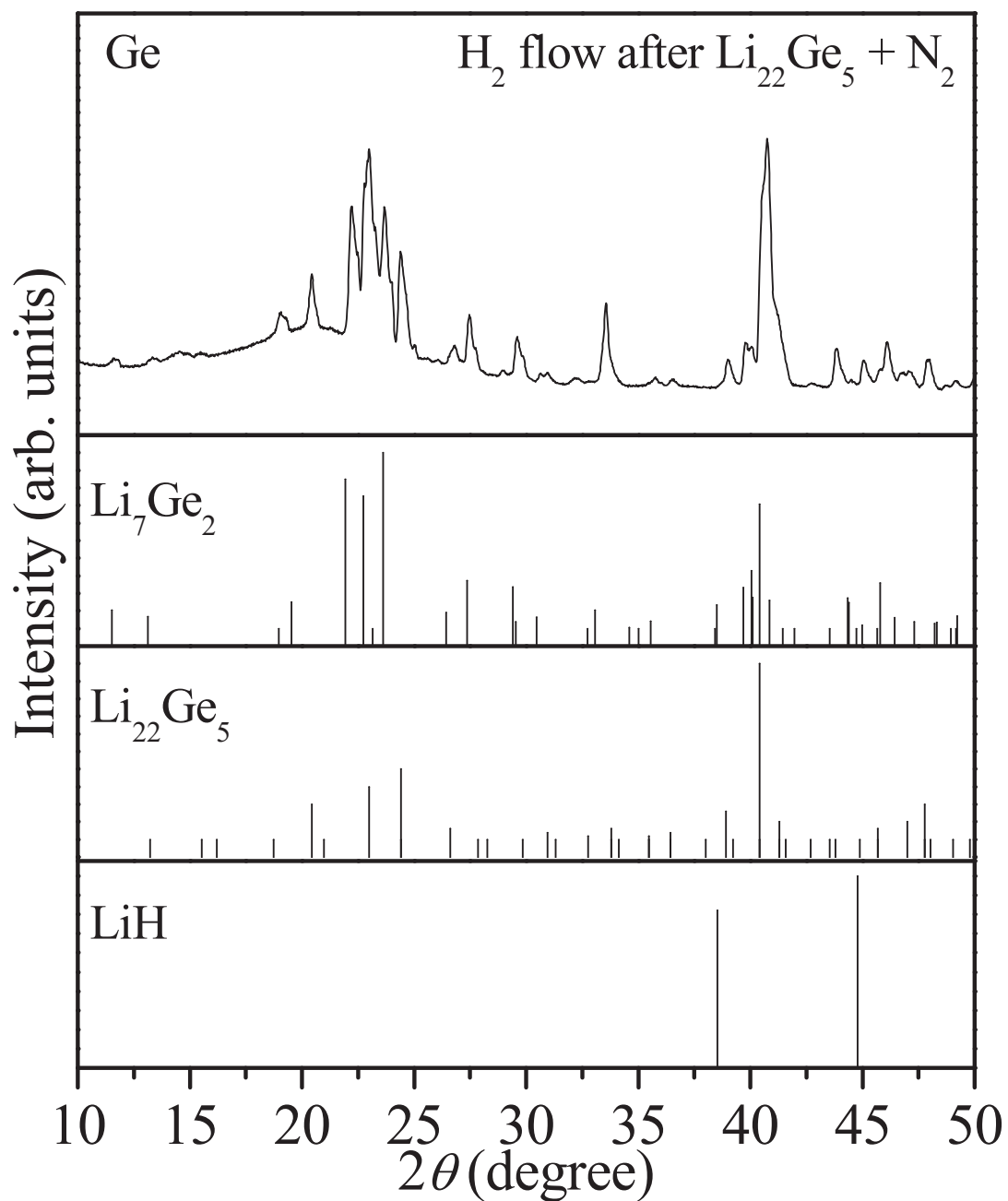


Figure 4-3-4 XRD patterns of nitrogenated Li-Ge alloy under N_2 condition after the DSC-MS measurement; XRD pattern of Li_7Ge_2 (PDF01-080-0531), $\text{Li}_{22}\text{Ge}_5$ (PDF01-017-0402), and LiH (PDF#78-0842) are referred from databases.

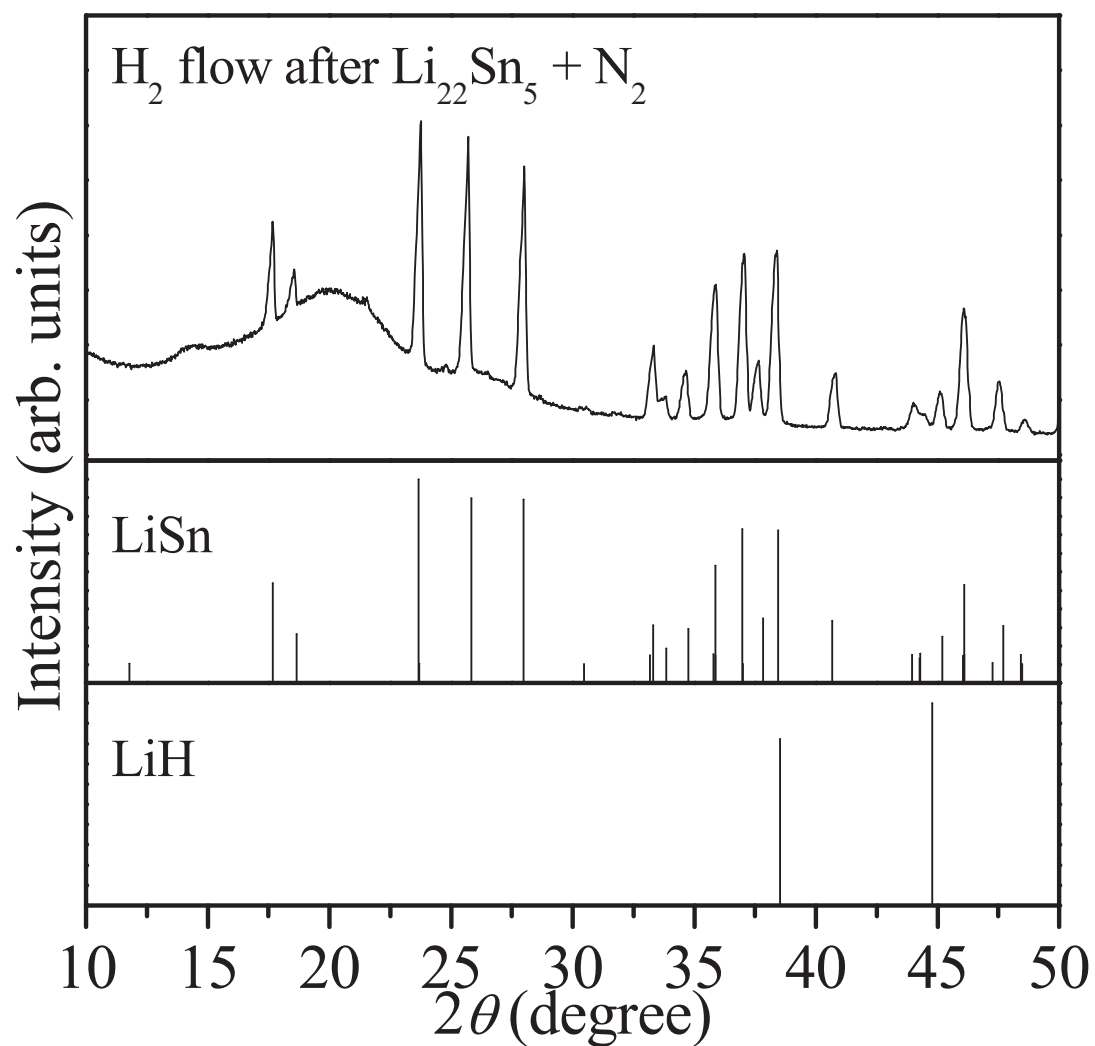


Figure 4-3-5 XRD patterns of nitrogenated Li-Sn alloy under N_2 condition after the DSC-MS measurement; XRD pattern of LiSn (PDF03-065-1261) and LiH (PDF#78-0842) are referred from databases.

4-4 Thermal decomposition of NaNH_2

To develop NaNH_2 as a functional material for practical use, the fundamental decomposition properties have to be understood. The decomposition properties of NaNH_2 were investigated in further detail by thermal and structural analyses.

Reaction system

Two types of reaction systems have been designed and assembled to investigate the decomposition process of NaNH_2 as shown Figure 4-4-1 at higher temperature than 300 °C. The reactor is composed of an inner sample-tube and an outer case. The inner tube is made from nickel based alloys to suppress the corrosion by Na-compounds, and the outer case is made from stainless steel. Sodium (Na), which is one of the expected reaction product, may be generated as the vapor phase at the given temperature because of its low melting point 98 °C. These reactors were equipped with the water cooling part to condense the Na vapor by solidification. In the reactor shown in Figure 4-4-1 (a), the reaction proceed under the non-equilibrium state due to evacuating the generated gaseous phase by a dynamic vacuum condition, suggesting that the decomposition is thermodynamically accelerated. In other words, the thermal decomposition of NaNH_2 proceeds without the effect of partial pressure of generated gases. This condition is called “vacuum condition”. The other reactor shown in Figure 4-4-1 (b) was designed to trap and analyze NH_3 , which was also one of the expected gaseous products. This condition is called “gas-trap condition”. In this system, the generated NH_3 was trapped as solid phase at a cooling part using liquid nitrogen, suggesting that the partial pressure of NH_3 would not affect the decomposition of NaNH_2 . Other expected gaseous products such as H_2 and N_2 remains in the reactor with some partial pressure. The heat treatments of NaNH_2 were carried out at 400 °C for 24 h in the above experimental system.

Figure 4-4-2 shows the results of thermogravimetry-differential thermal analysis-thermal desorption mass spectroscopy (TG-DTA-MS) below 230 °C which is slightly higher than the melting temperature of NaNH_2 . From the results obtained by this experiments, a small exothermic peak and two endothermic peaks were observed in the

DTA profiles with the detectable mass number of 28, which would be originated in N_2 , in this temperature range. The total weight loss due to N_2 desorption was less than 0.5 mass% below the temperature of 230 °C. This weight loss was quite small considered by N_2 desorption due to thermal decomposition of a bulk $NaNH_2$. Furthermore, if it is assumed that the origin of N_2 was bulk $NaNH_2$, H_2 desorption should be observed at the same time to balance. Any phase change was not found in the X-ray diffraction (XRD) measurements of the products after TG-DTA-MS as shown in Figure 4-4-3. Here, the low peak intensity is because of a small sample amount which is technical reason of our experiment. While the detailed decomposition process of $NaNH_2$ below 230 °C is not clarified yet, the origin of three peaks and mass signal could be explained as follows. The first exothermic reaction at 120 °C could be caused by crystallization such as refinement of disorder state in the synthesized $NaNH_2$ because any other exothermic reactions with N_2 desorption were not found in previous reports and speculated. In other words, the synthesize process could affect the chemical properties of $NaNH_2$. After that, two endothermic peaks around 150 °C and 200 °C were originated in phase transition because it was clarified that these peaks were reversible reactions by the differential scanning calorimetry (DSC) in our previous work, where the phase transition at 210 °C is melting of $NaNH_2$ ⁴⁻⁹). Generally, the phase transition should not be related to the gas desorption and it could be applied to the case of $NaNH_2$. However, David *et al.* also reported the similar N_2 desorption from $NaNH_2$ ⁴⁻¹⁰). Since $NaNH_2$ is an ionic chemical and not porous materials, the adsorbed state of N_2 should be unstable. Typically, adsorbed gas should be desorbed below 100 °C. The higher desorption temperature more than 100 °C indicates that chemically stable N atoms are desorbed even though the changes in composition and crystal structure is not found after N_2 desorption. As a similar phenomenon, Züttel *et al.* reported that small amount of H_2 was released with structural phase transition in the case of lithium borohydride ($LiBH_4$) ⁴⁻¹¹). Thus, the quite small amount of N_2 is possibly originated in above transition processes in the case of $NaNH_2$, in other words, unstable N atoms might exist at disorder sites in $NaNH_2$ and be desorbed as N_2 due to the phase transitions. As discussed above, the results obtained by TG-DTA-MS is not essential and not related to decomposition process because the amount of desorbed N_2 is very small

and crystal structure of NaNH_2 is clearly kept at the operation temperature range.

Figure 4-4-3 and Figure 4-4-4 show the XRD patterns of the reaction products obtained under vacuum condition and the gas-trap condition, respectively. Here, obtained XRD profiles were assigned by using database, which is shown in same figure below the XRD profile. For the vacuum condition, the diffraction peaks corresponding to the cooling part was totally assigned to Na metal, indicating that NaNH_2 was thermally reduced to metal phase at 400 °C. The weak peak intensity is caused by small sample amount. On the other hand, any peaks of NaNH_2 was not observed at XRD pattern corresponding to heating part and the observed peaks are not assigned to any Na-including materials in the PDXL database. For the gas-trap condition, the diffraction pattern of the product found at cooling part corresponds to NaNH_2 which is differently from the results vacuum condition. In this condition, it was thought that NaNH_2 was melted at heating part without decomposition and then some parts were evaporated and condensed at cooling part. At the heating part, unreacted NaNH_2 remained, and NaH was observed as the product from XRD profile, indicating that the reaction was slow and its process was different from that under the vacuum condition. A reason of the NaH formation will be discussed in the further details at later part.

After the reaction of gas-trap condition, gas-trap part was removed from liquid N_2 and kept it for several hours to obtain gaseous phase. The gaseous products were analyzed by gas chromatography (GC) using two kinds of column, which are Shincarbon and Chromosorb (Figure 4-4-5). As shown in the results by using the Shincarbon column, two peaks were observed at different detection time and these peaks were assigned to H_2 and N_2 . In addition, the generation of NH_3 was observed from the results of Chromosorb. It is noted that another peak can be assigned to the mixture of H_2 and N_2 . These results suggested that NH_3 is essentially generated during the decomposition process of NaNH_2 .

Above results suggest that partial pressure is important for decomposition process of NaNH_2 . Therefore, thermal treatments were performed under H_2 , N_2 , and NH_3 with the pressure of 1.0, 1.0, and 0.5 MPa, respectively. The XRD pattern obtained after the reaction were shown in Figure 4-4-6. Under the H_2 pressure, NaH was observed as product with remains of NaNH_2 , which is starting material. On the other hand, any

reaction products were not formed without NaNH_2 in the case of N_2 and NH_3 atmosphere. These results indicate that only partial pressure of H_2 affects the decomposition process and decomposition reaction should be suppressed if N_2 and NH_3 exist at the reaction field.

To characterize the unknown phase found at heating part under the vacuum condition, infrared (IR) spectroscopic measurement was performed. Figure 4-4-7 shows the IR spectra of the reaction products for both the experimental conditions together with spectrum of the as-synthesized NaNH_2 . The absorption peaks observed at 3210 and 3260 cm^{-1} were characteristic stretching modes of $-\text{NH}_2$ group ⁴⁻¹²⁾. For the product obtained by the gas-tarp condition, the observed peaks were totally same as those of NaNH_2 . On the other hand, for the products obtained by the vacuum condition, the characteristic stretching modes of $-\text{NH}_2$ were disappeared and new broad absorption peak appeared in the range of 3150-3210 cm^{-1} . The variation of this variation from NaNH_2 to unknown phase is similar to that from LiNH_2 to Li_2NH ⁴⁻¹³⁾, suggesting that a compound with $-\text{NH}$ group like imide (hereafter “ Na_2NH ”) was possibly generated.

Here, some diffraction peaks corresponding to the unknown phase were close to those of Na_2O . As a one possibility of the explanation for this result, NaNH_2 was possibly oxidized by mingled from leakage of the reactor though no leakage was checked at pre-experiment. If the considerable amount of O_2 exists in the reactor, Na_2O should be observed at cooling part as well because Na metal show high reactivity with O_2 . Raman spectroscopy was performed to distinguish the reaction products from Na_2O . Raman spectrum of the reaction products with spectra of NaNH_2 and Na_2O as reference were shown in Figure 4-4-8. The observed peaks originated in the phonon of solid materials were totally different between the products and reference of Na_2O . Considering the results of XRD and FT-IR, it is expected that the reaction product has similar cubic structure to that of Na_2O and has $-\text{NH}$ group as well. Here, if the $-\text{NH}$ group ($(\text{NH})_2^-$) is substituted for the O_2^- in Na_2O , it is possible that both the materials show similar crystal structure because signal from H atom cannot be detectable in XRD measurements. To determine this crystal structure corresponding to the new phase in further details, it should be required to be performed neutron diffraction measurement for deuterated sample.

From the results obtained by this experiments, the decomposition process would

be discussed follows. Under the vacuum condition at 400 °C, in which no partial pressure of any gases exist in the reaction field, the formation of “Na₂NH” was indicated. On the other hand, the Na generation is clearly found, suggesting that the imide-like phase is metastable state and decompose to Na gradually at the reaction conditions. If Na is generated preliminarily to the imide formation, it is expected that Na and/or NaH, which is possibly formed by the reaction of Na with the generated H₂, should be found at the cooling part in the case of gas-trap condition. Thus, “Na₂NH” is generated prior to Na because no Na generation is found in the gas-trap condition. As shown in Figure 4-4-4, NaH was formed at the heating part in the gas-trap condition. With respect to the NaH generation, two routes are though, and these would be hydrogenation of Na or the intermediate “Na₂NH”. Under the gas-trap condition, generated NH₃ and N₂ gas was solidified by liquid N₂ resulting in existence of partial pressure of H₂. The hydrogenation of Na metal generated by the decomposition of “Na₂NH” would proceed easily at the bottom of reactor. Here, it was reported that Li₂NH is hydrogenated to form amide and hydride phases by exothermic reactions as following equation (4-11) ⁴⁻¹⁴,



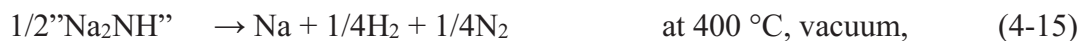
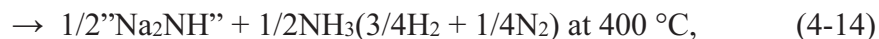
At 400 °C, NH₃ thermodynamically decomposed to H₂ and N₂, where the decomposition ratio is about 90 % under equilibrium condition with initial pressure 0.1 MPa. Assuming that the generated “Na₂NH” behaves like Li₂NH under a H₂ existent condition, NaH should be generated by the reaction of “Na₂NH” and H₂,



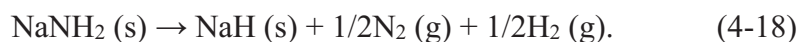
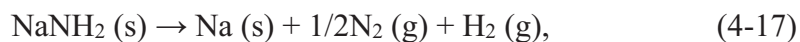
To understand the above hydrogenation process, the reaction between “Na₂NH” and H₂ was carried out by the DSC measurement (Figure 4-4-9). As a result, it was clarified that NaH was formed by the exothermic reaction, However, NaNH₂ was not found and other unknown phase was observed as the product (Figure 4-4-10). With respect to the “Na₂NH” and its hydrogenation, the structural identification is necessary to know the reaction details. Even though either of the above reactions proceeds, NaH is formed as the product at 400 °C under the H₂ partial pressure.

The decomposition process of NaNH₂ are described from the experimental results obtained in this work as follows, assuming that the intermediate phase is composed

of Na, N, H with 2:1:1 ratio based on “Na₂NH” defined,



NaNH₂ shows several phase transitions with small amount of N₂ emission below 230 °C as expressed by eq. (4-13), which are revealed by the TG-DTA-MS and XRD measurements. At 400 °C, it was indicated from the results of IR and Raman spectroscopy that the unreported phase with –NH group was generated as the metastable intermediate product, which is denoted as “Na₂NH”. And then, NH₃, H₂ and N₂ are observed as gaseous products by the GC measurements, where it is thermodynamically possible that H₂ and N₂ are generated by the partial decomposition of NH₃ at 400 °C. After that, the intermediate “Na₂NH” continuously decomposes to Na, H₂ and N₂ under the vacuum condition (eq. (4-15)). When the H₂ partial pressure exists under the closed gas-trap condition, “Na₂NH” is decomposed into NaH and the above gaseous products as shown in eq. (4-16). Previously, the following reactions were proposed as possible thermal decomposition processes ^{4-15, 16)},



It is reported that NaH is formed under H₂ atmosphere. Considering the products in eq. (4-14), the products obtained by the eq. (4-15) and (4-16) are consist with those of eq. (4-17) and (4-18), respectively.

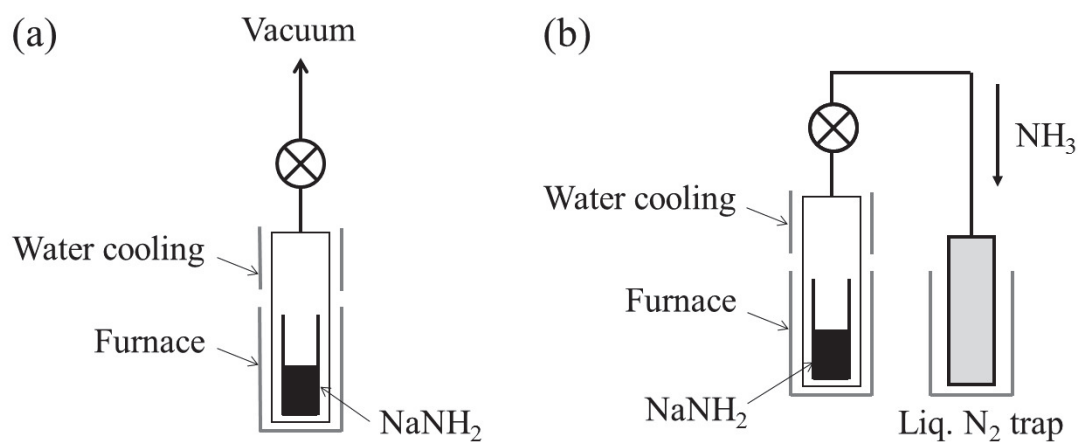


Figure 4-4-1 Schematic image of reaction systems for NaNH_2 decomposition (a) under vacuum condition and (b) under gas-trap condition.

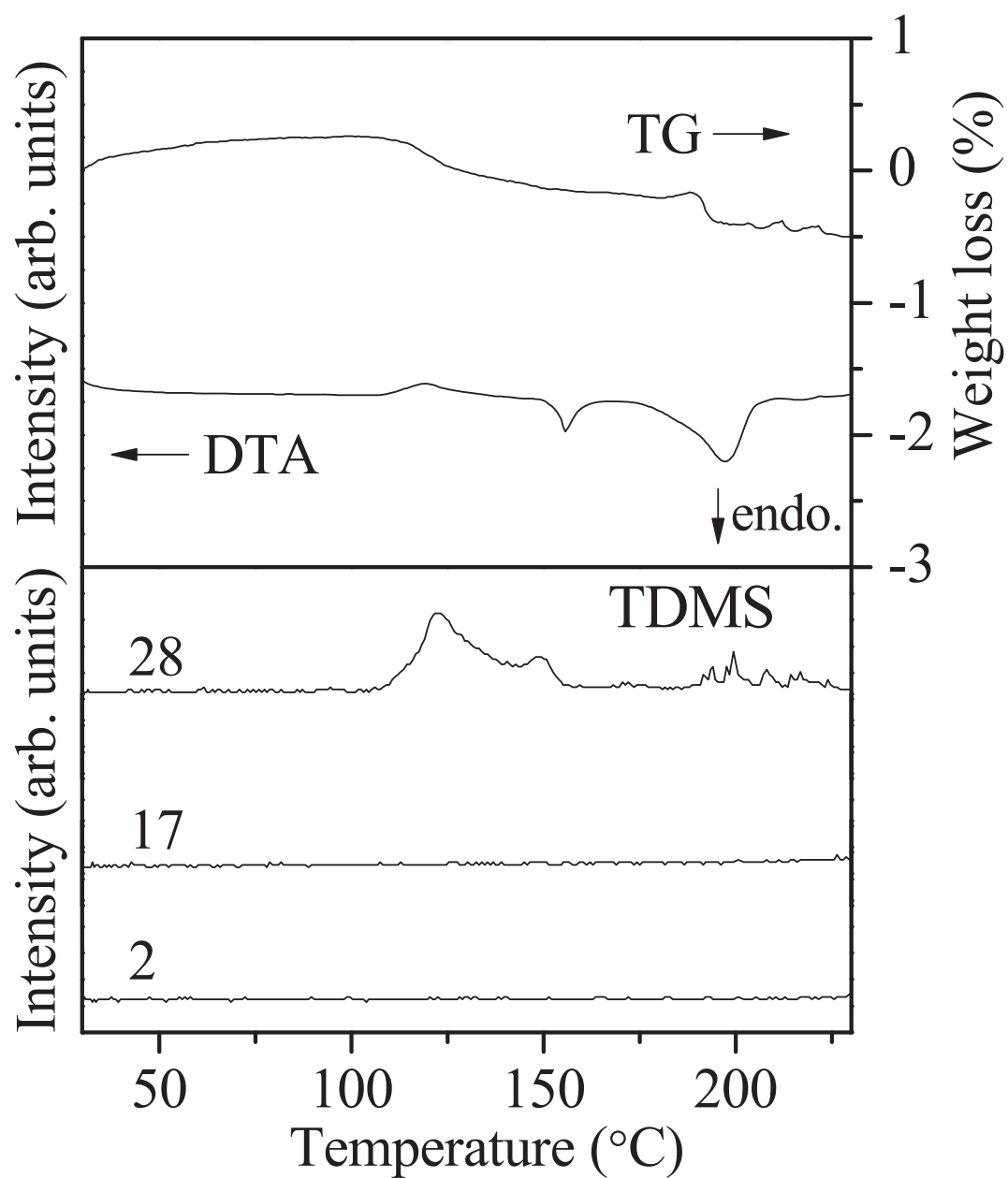


Figure 4-4-2 TG, DTA, and MS profiles of NaNH_2 , in which mass number 2, 17, and 28 correspond to H_2 , NH_3 , and N_2 , respectively.

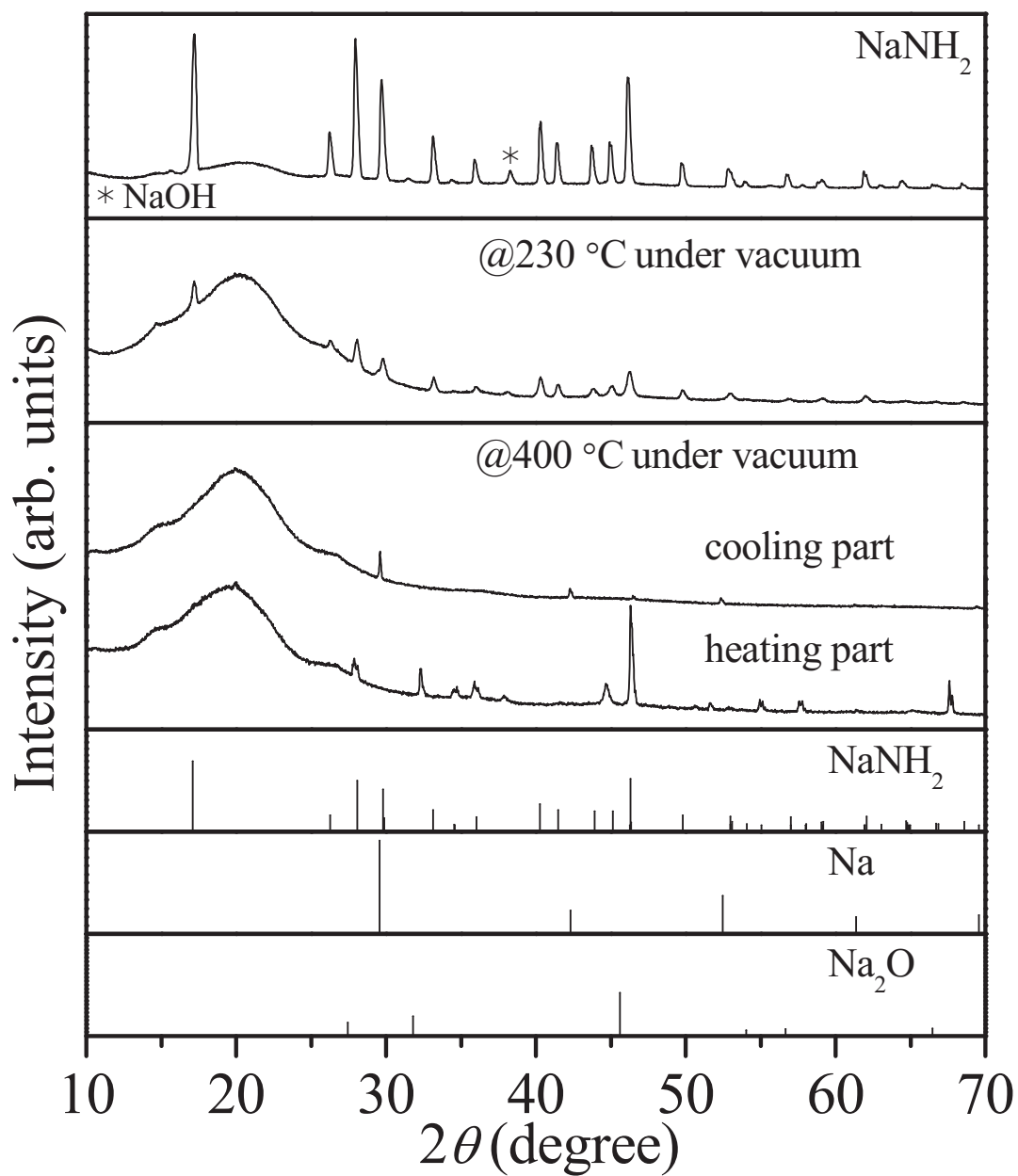


Figure 4-4-3 XRD patterns of as-synthesized NaNH₂, the products obtained by heating up to 230 and 400 °C under vacuum condition; XRD pattern of NaNH₂ (PDF00-000-0762), Na (PDF03-065-6995), and Na₂O (PDF01-077-2148) are referred from databases.

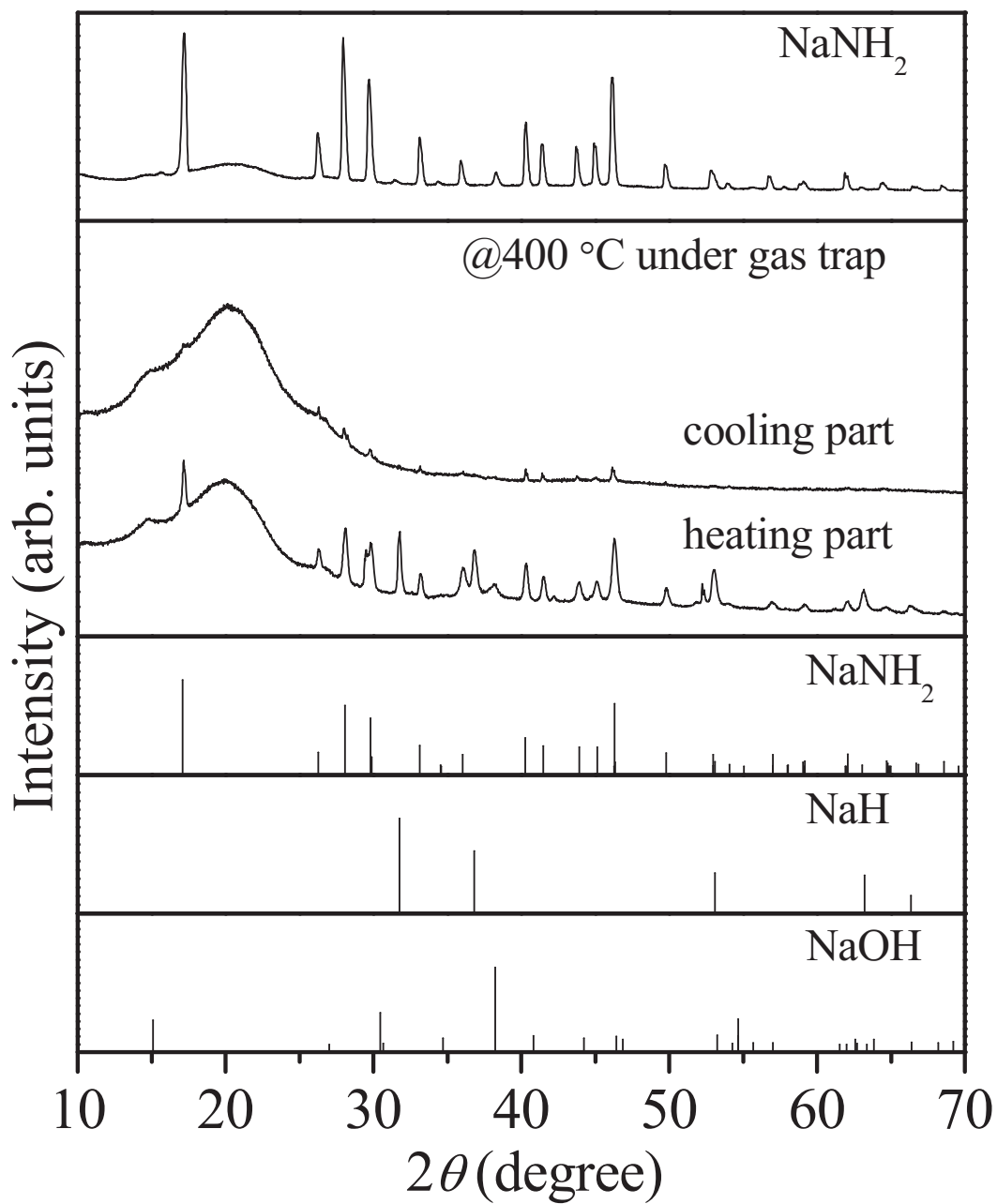


Figure 4-4-4 XRD patterns of as-synthesized NaNH₂ and the products obtained by heating up to 400 °C under gas-trap condition; XRD pattern of NaNH₂ (PDF00-000-0762), NaH (PDF00-000-1288), and NaOH (PDF01-078-0188) are referred from databases.

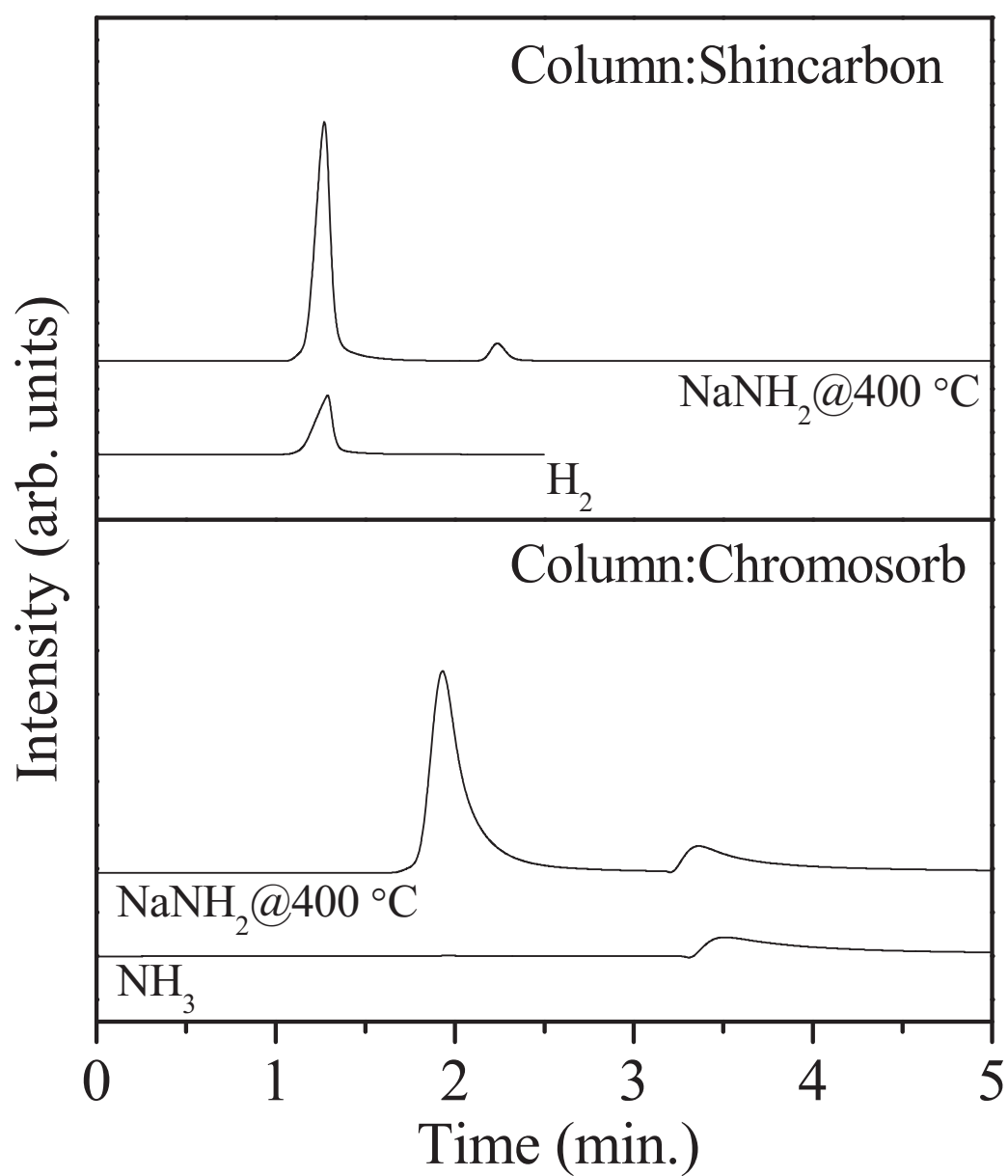


Figure 4-4-5 GC profiles using Shincarbon and Chromosorb columns of the gaseous products obtained by heating NaNH₂ at 400 °C. H₂ and NH₃ appended as reference.

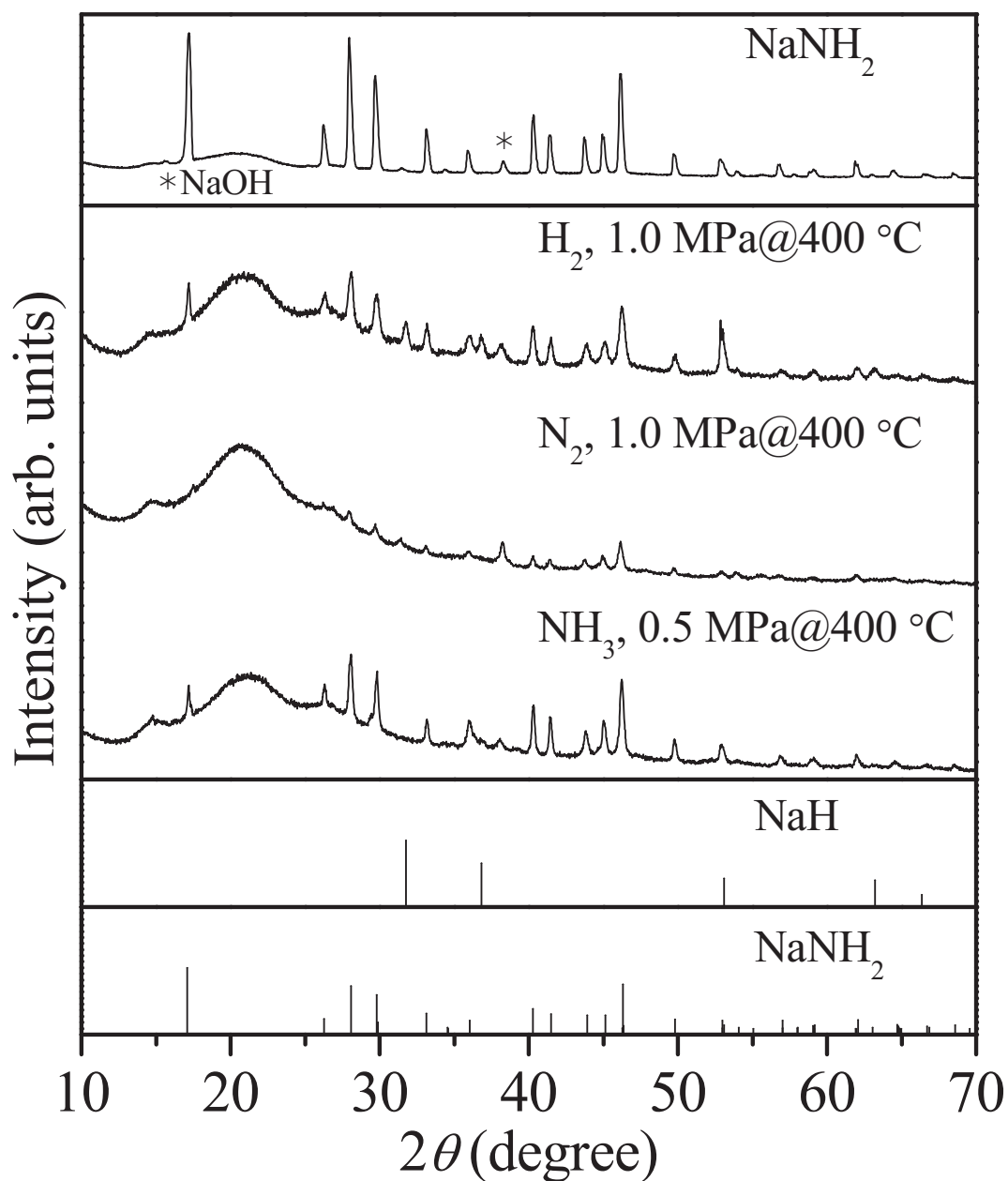


Figure 4-4-6 XRD patterns of as-synthesized NaNH₂ and products obtained by heating up to 400 °C under partial pressures of H₂, N₂, and NH₃ with the references; XRD pattern of NaH (PDF00-000-1288) and NaNH₂ (PDF00-000-0762) are referred from databases.

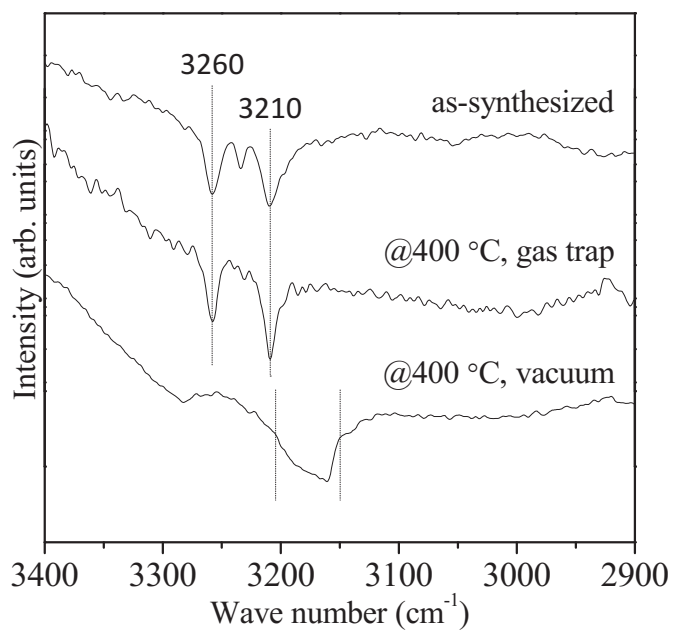


Figure 4-4-7 IR spectra of the as-synthesized NaNH_2 , the reaction products after heating at 400 °C under the gas-trap, and the vacuum condition.

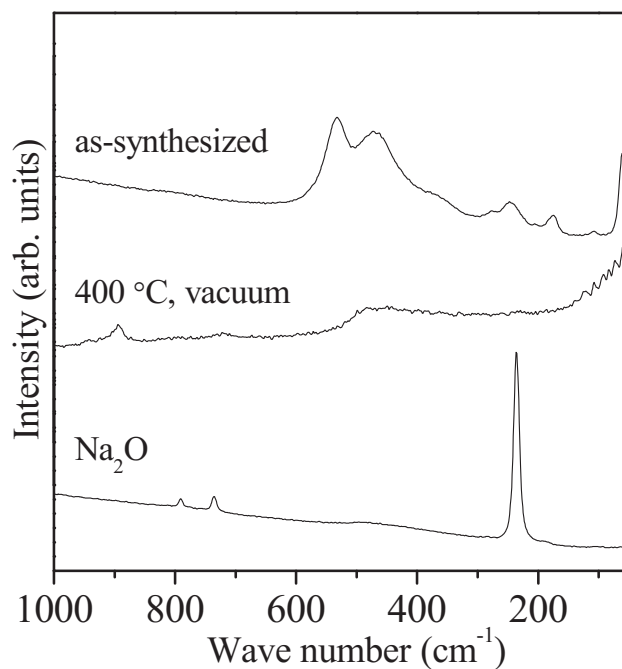


Figure 4-4-8 Raman spectra of the as-synthesized NaNH_2 , the reaction product after heating at 400 °C under the vacuum condition, and Na_2O as reference.

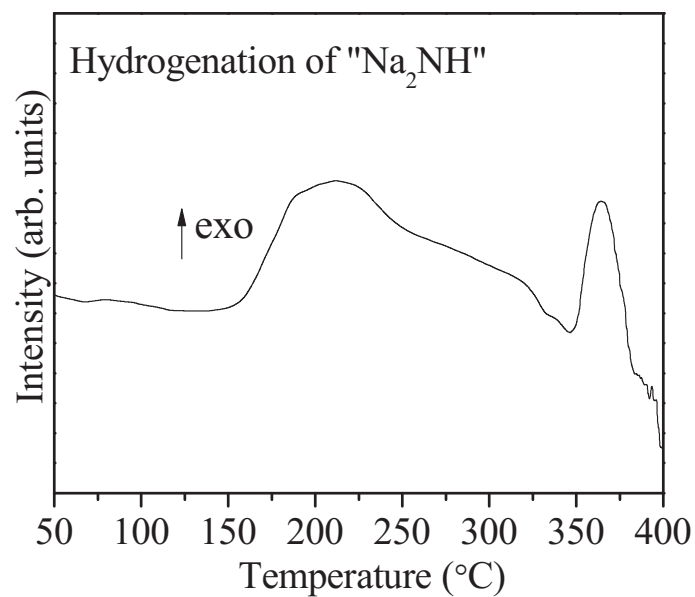


Figure 4-4-9 DSC profile obtained by the reaction between “Na₂NH” and H₂.

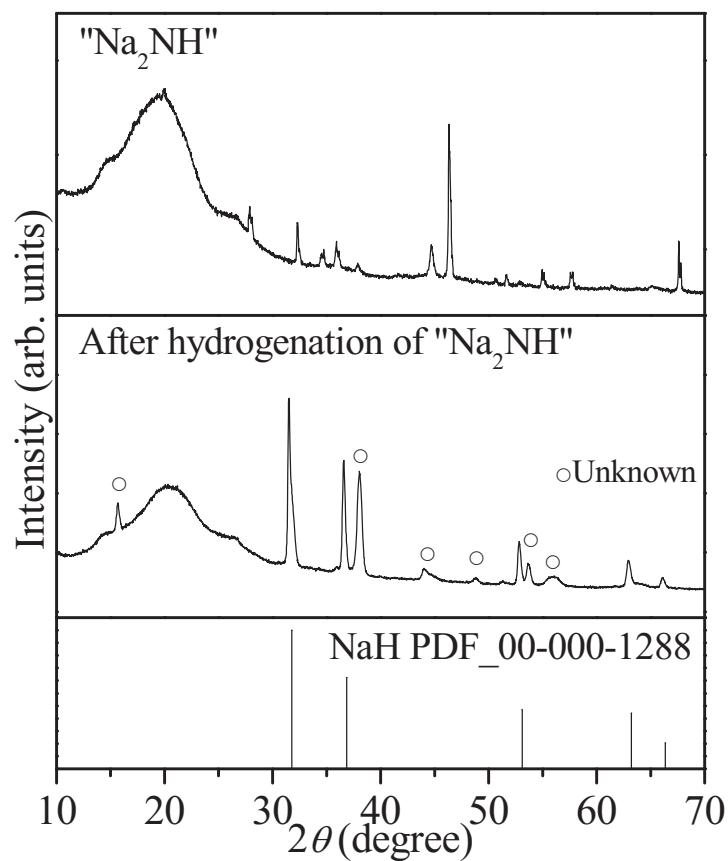


Figure 4-4-10 XRD patterns of the product obtained after the decomposition under the vacuum condition and after the hydrogenation of “Na₂NH” with the reference of NaH (PDF00-000-1288)

References

- 4-1. Miyaoka, H., W. Ishida, T. Ichikawa and Y. Kojima, *Journal of Alloys and Compounds* **509**, 719-723, (2011)
- 4-2. Gregory, D.H., *Journal of Materials Chemistry* **18**, 2321-2330, (2008)
- 4-3. Goshome, K., H. Miyaoka, H. Yamamoto, T. Ichikawa, T. Ichikawa and Y. Kojima, *MATERIALS TRANSACTIONS* **56**, (2015)
- 4-4. Jain, A., H. Miyaoka and T. Ichikawa, *Destabilization of lithium hydride by the substitution of group 14 elements: A review*, in *International Journal of Hydrogen Energy*. 2016. p. 5969-5978.
- 4-5. Aika, K.-i. and A. Ozaki, *Journal of Catalysis* **14**, 311-321, (1969)
- 4-6. Aika, K.-I. and A. Ozaki, *Journal of Catalysis* **19**, 350-352, (1970)
- 4-7. Aika, K.-i., H. Hori and A. Ozaki, *Journal of Catalysis* **27**, 424-431, (1972)
- 4-8. Jacobsen, C.J.H., S. Dahl, B.S. Clausen, S. Bahn, A. Logadottir and J.K. Nørskov, *Journal of the American Chemical Society* **123**, 8404-8405, (2001)
- 4-9. Yamamoto, H., H. Miyaoka, S. Hino, H. Nakanishi, T. Ichikawa and Y. Kojima, *International Journal of Hydrogen Energy* **34**, 9760-9764, (2009)
- 4-10. David, W.I.F., J.W. Makepeace, S.K. Callear, H.M.A. Hunter, J.D. Taylor, T.J. Wood and M.O. Jones, *Journal of the American Chemical Society* **136**, (2014)
- 4-11. Züttel, A., P. Wenger, S. Rentsch, P. Sudan, P. Mauron and C. Emmenegger, *Journal of Power Sources* **118**, 1-7, (2003)
- 4-12. Zhang, Y. and Q. Tian, *International Journal of Hydrogen Energy* **36**, 9733-9742, (2011)
- 4-13. Kojima, Y. and Y. Kawai, *Journal of Alloys and Compounds* **395**, 236-239, (2005)
- 4-14. Chen, P., Z. Xiong, J. Luo, J. Lin and K.L. Tan, *Nature* **420**, 302-304, (2002)
- 4-15. Titherley, A.W., *Journal of the American Chemical Society* **65**, 504-522, (1894)
- 4-16. Juza, R., *Angewandte Chemie int ed* **3**, 471-481, (1964)

5 Conclusion

In this thesis, the research on nitrogen related materials, which is especially nitride synthesis and utilization technique, is summarized. The reaction for nitrogen dissociation and nitride synthesis were systematically investigated by using lithium alloys composed of Li and 14 group elements, which are C, Si, Ge, and Sn. Furthermore, the decomposition properties of nitrogen composed material (NaNH_2) were investigated in details. It was revealed that nitrogen dissociation and reformation are manageable at some feasible reaction conditions although it is expected to be difficult because of its strong bonds. The obtained results are summarized as follows.

The nitrogenation properties were investigated by the DSC measurements under N_2 gas. All the alloys dissociate nitrogen triple bond of N_2 to form atomic states as nitrides below 500 °C. For the Li-C, Si, and Sn alloys, nano-sized Li_3N was formed as a product while ternary nitride was generated in the case of Li-Ge alloy. It is interesting that the generated Li_3N is partially nano-tube or fiber structure. The denitrogenation reactions by Li_3N and M mixtures were examined by the thermal analyses with heating up to 600 °C under Ar flow conditions, and the N_2 desorption was confirmed for all the systems. For the Ge alloy, the ternary nitride formation as unexpected reactions was observed in both of the reactions. It is indicated that the Li-C and Li-Si alloys show partially reversible reactions with N_2 . Among the series of Li-M alloys, the Li-Sn alloy is only a potential material to control the dissociation and recombination of N_2 below 500 °C by a reversible reaction with the largest amount of utilizable Li. From the above results, it is concluded that the nitrogenation and denitrogenation reactions of the Li alloys at a lower temperature would be realized by the high reactivity with N_2 and mobility of Li. Furthermore, the feasibility of the Li alloys as the pseudo-catalytic process for NH_3 synthesis was experimentally demonstrated. As a result, NH_3 can be synthesized below 500 °C under less than 0.5 MPa of pressure. Considering the reaction mechanism, it is expected that the pseudo-catalysts using Li alloys are developed as a “self-activation” process.

The decomposition process of NaNH_2 under the different reaction conditions were investigated. Although NaNH_2 was not decomposed below 230 °C, several phase transitions such as structural change and melting with small amounts of the N_2 desorption, which are originated in possibly crystallization at 120 °C, in phase transition at 150 °C, and in melting at 210 °C, were revealed. NaNH_2 decomposed to Na metal at 400 °C via the unreported intermediate phase with gases generation of H_2 , N_2 , and NH_3 . It was proposed by the characterization using XRD, FT-IR, and Raman spectroscopies that the unknown phase could be “ Na_2NH ”, which would have similar cubic crystal structure to Na_2O . In our future work, the synthesis conditions of “ Na_2NH ” single phase should be obtained, and then the crystal structure of “ Na_2NH ” would be determined by neutron diffraction for the deuterated sample. The decomposition processes of NaNH_2 were clearly affected by the partial pressure of gaseous products. Especially, it was indicated that “ Na_2NH ” is changed to NaH as the final product under the presence of H_2 partial pressure.

公表論文

(1) Thermal Decomposition of Sodium Amide

Shotaro Yamaguchi, Hiroki Miyaoka, Takayuki Ichikawa, and Yoshitsugu Kojima

International Journal of Hydrogen Energy, **42**, 5213-5219, (2017)

参考論文

- (1) Thermochemical Water-Splitting Reaction by Alkali Metal-Cobalt Oxide
Shotaro Yamaguchi, Naoya Nakamura, Hikaru Yamamoto, Hitoshi Inokawa,
Takayuki Ichikawa, Yoshitsugu Kojima, and Hiroki Miyaoka
Journal of the Japan Institute of Energy, **92**, 909-912, (2013)
- (2) Anode Properties of Al₂O₃-added MgH₂ for All-Solid-State Lithium-Ion Battery
Suguru Ikeda, Takayuki Ichikawa, Kiyotaka Goshome, Shotaro Yamaguchi,
Hiroki Miyaoka, and Yoshitsugu Kojima
Journal of Solid State Electrochemistry, **19**, 3639-3644, (2015).
- (3) Catalysis of Lithium Chloride and Alkali Metal Borohydrides on Hydrogen
Generation of Ammonia and Lithium Hydride System
Hiroki Miyaoka, Keita Nakajima, Shotaro Yamaguchi, Taihei Aoki, Hikaru
Yamamoto, Takahiro Okuda, Kiyotaka Goshome, Takayuki Ichikawa, and
Yoshitsugu Kojima
Journal of Physical Chemistry C, **119**, 19922-19927, (2015)
- (4) Catalytic Modification in Dehydrogenation Properties of KSiH₃
Ankur Jain, Takayuki Ichikawa, Shotaro Yamaguchi, Hiroki Miyaoka, and
Yoshitsugu Kojima
Physical Chemistry Chemical Physics, **16**, 26163-26167, (2014)
- (5) Effects of Metal Oxide Additives on Anode Properties of Magnesium Hydride for
All-Solid-State Lithium Ion Batteries
Suguru Ikeda, Takayuki Ichikawa, Shotaro Yamaguchi, Hiroki Miyaoka, and
Yoshitsugu Kojima
Journal of the Japan Institute of Energy, **93**, 926-930, (2014)